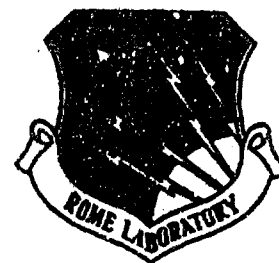


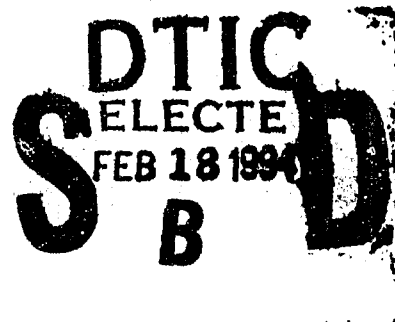
AD-A275 763
Rome Laboratory
1980

AD-A275 763



RL/ERCT AUTOMATED SWEEP-ANGLE BISTATIC MEASUREMENT SYSTEM

Doc Cl. Cote



APPROVED FOR PUBLIC RELEASE; DISTRIBUTION UNLIMITED.

BEST AVAILABLE COPY

12/96

94-05340



DTIC QUALITY INSPECTED 2

Rome Laboratory
Air Force Materiel Command
Griffiss Air Force Base, New York

94 2 17 062

This report has been reviewed by the Rome Laboratory Public Affairs Office (PA) and is releasable to the National Technical Information Service (NTIS). At NTIS it will be releasable to the general public, including foreign nations.

RL-TR-93-52 has been reviewed and is approved for publication.

APPROVED:

Robert V. McGahan

ROBERT V. McGAHAN, Chief
Applied Electromagnetics Division
Electromagnetics & Reliability Directorate

FOR THE COMMANDER:

John K. Schindler

JOHN K. SCHINDLER
Director of Electromagnetics & Reliability
Electromagnetics & Reliability Directorate

If your address has changed or if you wish to be removed from the Rome Laboratory mailing list, or if the addressee is no longer employed by your organization, please notify RL(ERCT) Hanscom AFB MA 01731-5000. This will assist us in maintaining a current mailing list.

Do not return copies of this report unless contractual obligations or notices on a specific document require that it be returned.

REPORT DOCUMENTATION PAGE			Form Approved OMB No. 0704-0188	
Public reporting burden for this collection of information is estimated to average 1 hour per response, including the time for reviewing instructions, searching existing data sources, gathering and maintaining the data needed, and completing and reviewing the collection of information. Send comments regarding this burden estimate or any other aspect of this collection of information, including suggestions for reducing this burden, to Washington Headquarters Services, Directorate for Information Operations and Reports, 1215 Jefferson Davis Highway, Suite 1204, Arlington, VA 22202-4302, and to the Office of Management and Budget, Paperwork Reduction Project (0704-0188), Washington, DC 20503.				
1. AGENCY USE ONLY (Leave blank)		2. REPORT DATE April 1993		3. REPORT TYPE AND DATES COVERED In-House October 1985 - June 1989
4. TITLE AND SUBTITLE RL/ERCT Automated Swept-Angle Bistatic Measurement System			5. FUNDING NUMBERS PE - 62702F PR - 4600 TA - 15 WU - 06	
6. AUTHOR(S) Marc G. Cote				
7. PERFORMING ORGANIZATION NAME(S) AND ADDRESS(ES) Rome Laboratory/ERCT 31 Grenier Street Hanscom AFB MA 01731-3010			8. PERFORMING ORGANIZATION REPORT NUMBER RL-TR-93-52	
9. SPONSORING/MONITORING AGENCY NAME(S) AND ADDRESS(ES)			10. SPONSORING/MONITORING AGENCY REPORT NUMBER	
11. SUPPLEMENTARY NOTES				
12a. DISTRIBUTION/AVAILABILITY STATEMENT Approved for public release, distribution unlimited.			12b. DISTRIBUTION CODE	
13. ABSTRACT (Maximum 200 words) A bistatic scattering measurement system well suited to support basic research in target scattering is described. The system can measure bistatic scattering from near backscatter through forward scatter. At X-band frequency, scattering levels of -50 dBsm in the backscattering region and -18 dBsm at forward scatter can be measured to an accuracy of +/-1 dB. This fully automated indoor system fixes the target and direction of illumination and sweeps the receive antenna to collect data as a direct function of bistatic angle. A broadband, coherent, continuous wave radar is used to obtain both amplitude and phase of the component of the total field aligned with the receive antenna polarization. Target scattered fields are derived from the phasor subtraction of target and background measurement runs. We consider the system design, calibration procedure, and measurement accuracy. Example measurements on metal cubes and spheres are presented to demonstrate the system performance.				
14. SUBJECT TERMS Swept-angle bistatic scattering Radar-cross-section measurements			15. NUMBER OF PAGES 102	
			16. PRICE CODE	
17. SECURITY CLASSIFICATION OF REPORT Unclassified	18. SECURITY CLASSIFICATION OF THIS PAGE Unclassified	19. SECURITY CLASSIFICATION OF ABSTRACT Unclassified	20. LIMITATION OF ABSTRACT SAR	

Contents

1	INTRODUCTION	1
2	SYSTEM OVERVIEW AND THEORY	3
3	OPERATING PROCEDURES	5
4	CALIBRATING THE MEASUREMENTS	11
5	EXAMPLE MEASUREMENTS	17
6	SUMMARY AND CONCLUSIONS	27
	REFERENCES	31
	APPENDIX A: DATA STRUCTURE	33
	APPENDIX B: RL/ERCT SYSTEM	47
	APPENDIX C: BACKGROUND LEVELS AT 10 GHz	55
	APPENDIX D: DERIVATION OF THE MINIMUM RCS MEASUR- ABLE	91

Accession For	
NTIS GRA&I	<input checked="" type="checkbox"/>
DTIC TAB	<input type="checkbox"/>
Unannounced	<input type="checkbox"/>
Justification	
By _____	
Distribution/	
Availability Codes	
Dist	Avail and/or Special
A-1	

Figures

1	Photograph of the Anechoic Chamber part of the Swept-Angle Bistatic Measurement System	1
2	ASBSMS System Component Layout and Measurement Geometry	3
3	ASBSMS Diagram Summarizing the Measurement Procedure	7
4	Measurement Geometry Shown in Plan View and Target Orientation Geometry Shown in the Three Views - Plan, Side, and End	8
5	Polystyrene Foam Target Support Pedestal and Target Orientation Apparatus	9
6	Target Alignment Geometry	9
7	Scattering from a Perfectly Conducting Sphere, $ka = 18$	12
8	Typical Point Calibration Phasors Computed from Unshifted Measurements (No Offset), and Computed from Measurements Shifted 0.8° Relative to the Exact Solution	14
9	Phase of the Point Calibration Phasor and Best Fit Curve	15
10	Measurement Geometry with Calibration Sphere Displaced	16
11	Amplitude and Phase of the Background Field Collected Prior to the Calibration Sphere Measurement	18
12	Measured Total Field of the Calibration Sphere ($ka = 18$)	19
13	Amplitude and Phase of the Background Field Measured After the Calibration Sphere	20
14	Amplitude and Phase of the Typical Measured Total Field	21
15	Amplitude and Phase of the Typical Measured Background Field	22
16	Background Perturbation Phasor Obtained by Computing the Ratio of Figures 11 and 13	24
17	Measured Scattered Field of an Aluminum Sphere ($ka = 18$)	25
18	Measured Scattered Field of an Aluminum Cube ($s = 0.75\lambda$)	26
19	Calibrated Measured Scattering Cross Section of an Aluminum Cube ($s = 0.75\lambda$) with Error Bars, Compared to a Dual-Surface Magnetic-Field Integral Equation (DSMFIE) Solution	28
A.1	Data Base File Structure on the ASBSMS System Disc	35
A.2	Data Base Index-File Structure on the ASBSMS System Disc	38
A.3	Example System Disc Index-File (<i>SASX.PRG</i>)	40
A.4	Example System Disc Data Base File (<i>SASX.DAT</i>)	41
A.5	VAX-Based Data File Structure Required by the RCS Data Processor (RCS-DPP) which Runs the RL/ERCT VAX 11750	43
A.6	Example of a VAX-Based Total-Field Data File (File Name <i>SASX040393.RAWD</i>) Showing Total-Field Measurement Data for an E-plane Cut of a Square Plate at 10 GHz	44
A.7	Example of a VAX-Based Background-Field Data File (File Name <i>SASX040395.RAWD</i>) Showing E-plane Background-Field Measurement Data at 10 GHz	45

A.8	Example of a VAX-Based Scattered-Field Data File (File Name <i>SASX040393.SUBT</i>) Showing Scattered-Field Measurement Data for an E-plane Cut of a 5λ Square Plate at 10 GHz	46
B.1	Anechoic Chamber Subsystem with Cartesian Coordinate System Superimposed	48
B.2	Maximum Target Dimension for Accurate Scattering Measurements	48
B.3	Receive Subsystem Schematic	49
B.4	Measured Linearity of SA-1785 Receiver with SA 14-5 Mixers at 10 GHz . .	50
B.5	Transmit Subsystem Schematic	51
B.6	Schematic Diagram of the ASBSMS Positioning Subsystem	51
B.7	System Controller Subsystem Schematic	52
C.1	Calibrated H-plane Background Measurement Collected on the First Day of the Experiment	56
C.2	Calibrated H-plane Background Measurement Collected on the Second Day of the Experiment	57
C.3	Calibrated H-plane Background Measurement Collected on the Third Day of the Experiment	58
C.4	Calibrated E-plane Background Measurement Collected on the First Day of the Experiment	60
C.5	Calibrated E-plane Background Measurement Collected on the Third Day of the Experiment	61
C.6	Calibrated E-plane Background Measurement Collected on the Fifth Day of the Experiment	62
C.7	Average Calibrated H-plane Background Measurements	63
C.8	Average Calibrated E-plane Background Measurements	64
C.9	Calibrated H-plane Residual Background Computed for Two Background Measurements Separated in Time by Approximately 1 Hour	65
C.10	Calibrated H-plane Residual Background Computed for Two Background Measurements Separated in Time by Approximately 1 day and 2 Hours . . .	65
C.11	Calibrated E-plane Residual Background Computed for Two Background Measurements Separated in Time by Approximately 1 Hour	66
C.12	Calibrated E-plane Residual Background Computed for Two Background Measurements Separated in Time by About 2 Hours	66
C.13	Average Calibrated H-plane Residual Backgrounds	67
C.14	Average Calibrated E-plane Residual Backgrounds	68
C.15	Perturbation Phasor Computed from Two H-plane Background Measurements Separated in Time by Approximately 1 Hour	69
C.16	Perturbation Phasor Computed from Two H-plane Background Measurements Separated in Time by About 2 Hours	70
C.17	Perturbation Phasor Computed from Two H-plane Background Measurements Separated in Time by About 19 Hours	71
C.18	Perturbation Phasor Computed from Two H-plane Background Measurements Separated in Time by About 20 Hours	72

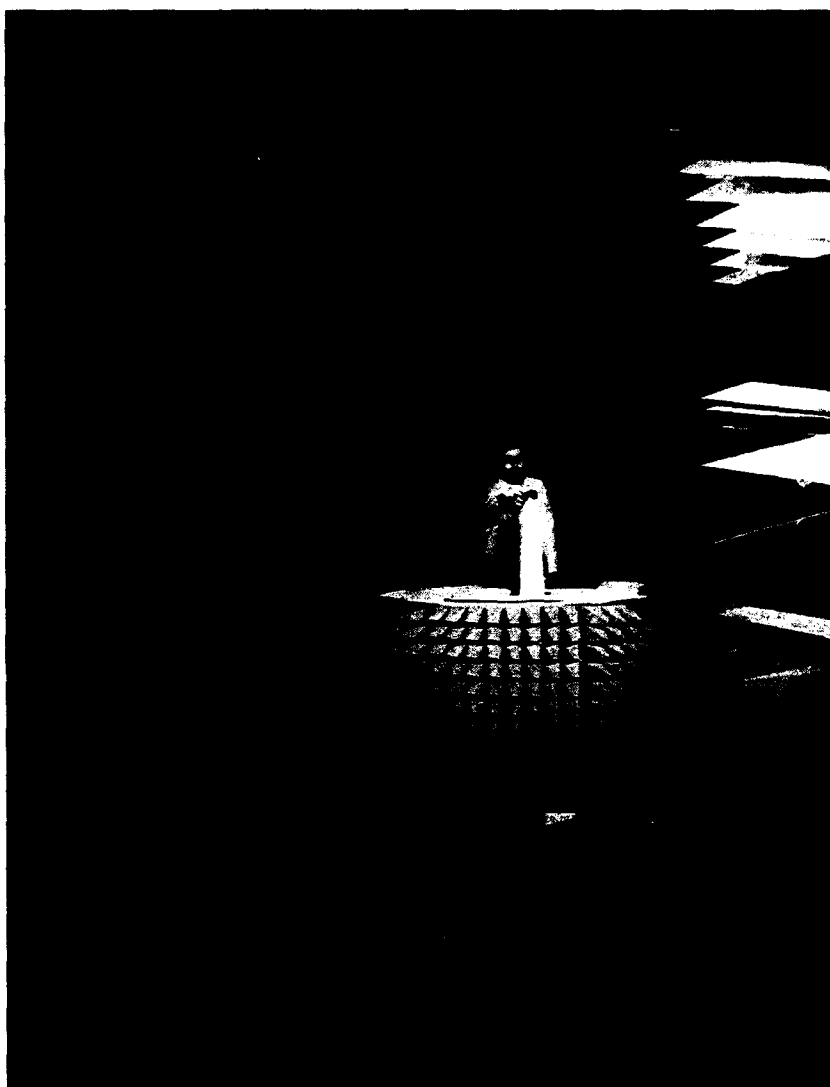
C.19 Perturbation Phasor Computed from Two H-plane Background Measurements Separated in Time by About 44 Hours	73
C.20 Perturbation Phasor Computed from Two H-plane Background Measurements Separated in Time by About 45 Hours	74
C.21 Perturbation Phasor Computed from Two H-plane Background Measurements Separated in Time by About 46 Hours	75
C.22 Perturbation Phasor Computed from Two H-plane Background Measurements Separated in Time by About 46.5 Hours	76
C.23 Perturbation Phasor Computed from Two H-plane Background Measurements Separated in Time by About 47.4 Hours	77
C.24 Perturbation Phasor Computed from Two H-plane Background Measurements Separated in Time by About 48.3 Hours	78
C.25 Perturbation Phasor Computed from Two E-plane Background Measurements Separated in Time by Approximately 1 Hour	79
C.26 Perturbation Phasor Computed from Two E-plane Background Measurements Separated in Time by About 2 Hours	80
C.27 Perturbation Phasor Computed from Two E-plane Background Measurements Separated in Time by About 3 Hours	81
C.28 Perturbation Phasor Computed from Two E-plane Background Measurements Separated in Time by About 24 Hours	82
C.29 Perturbation Phasor Computed from Two E-plane Background Measurements Separated in Time by About 25 Hours	83
C.30 Perturbation Phasor Computed from Two E-plane Background Measurements Separated in Time by About 26 Hours	84
C.31 Perturbation Phasor Computed from Two E-plane Background Measurements Separated in Time by About 27 Hours	85
C.32 Perturbation Phasor Computed from Two E-plane Background Measurements Separated in Time by About 98 Hours	86
C.33 Perturbation Phasor Computed from Two E-plane Background Measurements Separated in Time by About 99 Hours	87
C.34 Perturbation Phasor Computed from Two E-plane Background Measurements Separated in Time by About 100 Hours	88
C.35 Perturbation Phasor Computed from Two E-plane Background Measurements Separated in Time by About 117 Hours	89

Tables

A.1 Description of Mnemonics Used to Encode the Measurement and Receiver Parameters	36
A.2 System Disc Plotting Code Used by the ASBSMS when Plotting Data at the Measurement Site	37
A.3 Description of Mnemonics Used in Figure 6 to Describe the Measurement Parameters	42

Preface

I am grateful to Richard Wing for collecting the many millions of bytes of data necessary to write this report, only a small fraction of which are presented within. My thanks go out to Keith Trott, Robert McGahan, and Arthur Yaghjian for the helpful editorial comments regarding the manuscript and to John Quinn for his help with data processing and software writing. Finally, I am indebted to Jo-Ann Ducharme for typing the manuscript, a task that involved decoding my cryptic revisions more times than I care to count.



A view from the theodolite port showing Mr. Richard Wing installing a conisphere on the polystyrene foam target support column. The photograph was taken by Mr. Lee M. Stevens of Phillips Laboratory (PL/TSV).

1 INTRODUCTION

This report describes the bistatic scattering measurement system used by the Rome Laboratory Electromagnetics and Reliability Directorate (RL/ER) to conduct research in electromagnetic scattering. A manual version of this system was conceived and designed by Robert McGahan in 1984. The manual system was built and tested [1] [2] [3] with the help of Mr. David Gaunt. The basic system (see Figure 1) has changed little from the original design and has evolved into an essential part of the ERCT in-house research program. The system is named the Automated Swept-Angle Bistatic Scattering Measurement System (ASBSMS) because it fixes the target and direction of illumination and sweeps the receiving probe to collect data as a direct function of bistatic angle. The system uses a broad band, coherent, continuous wave radar that operates in the S, C, and X frequency bands (2-12.4 GHz). The

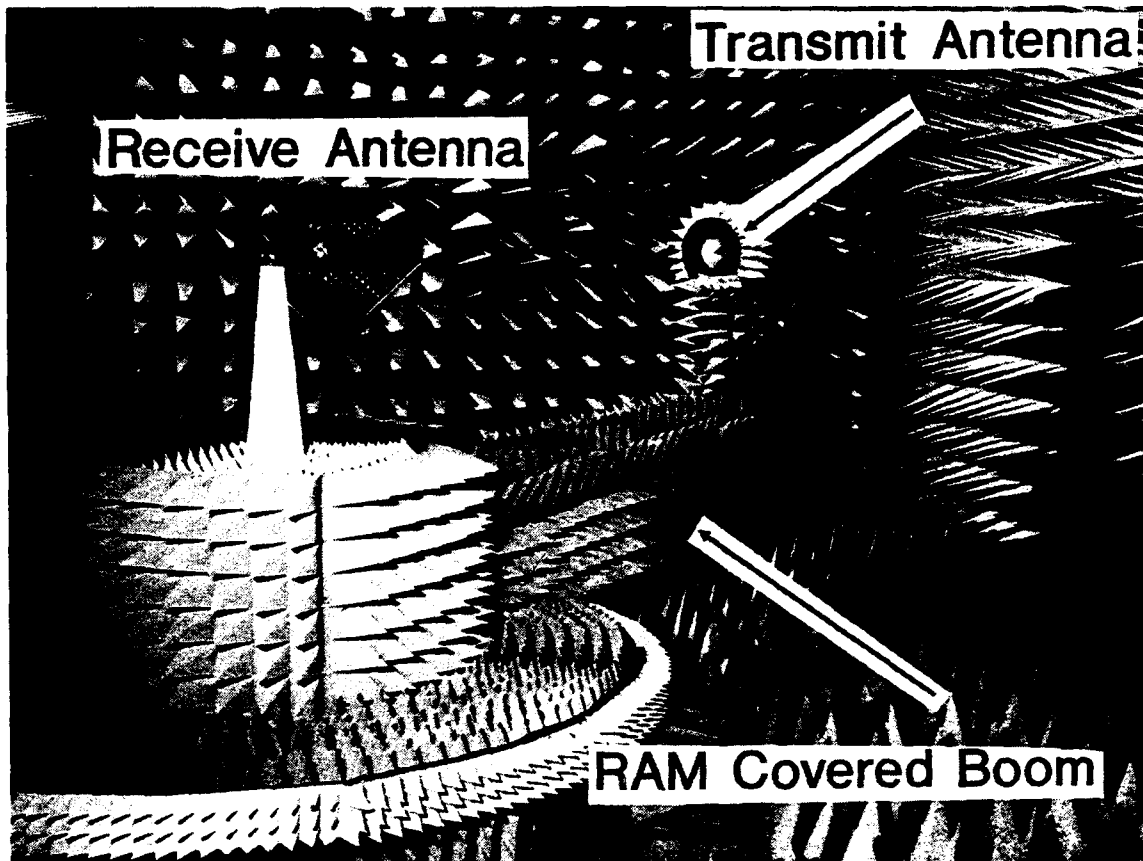


Figure 1: Photograph of the Anechoic Chamber part of the Swept-Angle Bistatic Measurement System

Received for publication 26 April 1993

ASBSMS has two distinct advantages over conventional fixed-angle bistatic measurement systems. First, it is better suited for verifying theoretical scattering models because it measures what is usually computed from the theory. Conventional measurements, in contrast, gather data as a function of illumination direction (aspect) reproducing a single point of the typical scattering model output. Second, the ASBSMS can be calibrated at small bistatic angles where typical calibration target (usually metal spheres) scattering is well behaved. This calibration remains valid for all bistatic angles. In contrast, the fixed angle bistatic systems are difficult to calibrate at large bistatic angles because calibration spheres tend to have scattering patterns with rapid spatial variations in the forward scattering region. At high bistatic angles the system calibration depends strongly on the accuracy of the position information.

This report tells what the ASBSMS is, the theoretical basis it is founded on, how it operates, and how the data are calibrated. It begins with a system overview giving a general description of the system hardware. Then the theory is developed and the assumptions of the measurement technique discussed. Section 3 presents the operating procedures, discussing in detail the three major tasks of aligning targets, collecting data, and assessing system performance. Section 4 details the calibration procedure and includes example data for illustrative purposes. Finally, the measurement procedure is applied to obtain the E-plane scattering pattern of an aluminum cube 3 wavelengths on a side. This section includes a description of how error bars are computed for the measured scattering patterns. Three Appendices are included that give specific details of the system and system performance. Appendix A gives the structure of the raw data stored on the system hard disc, and the structure of the processed data that we give to customers. Appendix B gives a detailed description of the ASBSMS subsystems and lists the specific hardware along with its specifications. Appendix C presents data demonstrating the background level and stability at 10 GHz.

In preparing this report I have come across several articles that shed light on errors in scattering measurements [12] [13] [14] [15] [16], and discussed various aspects of bistatic scattering measurements [16] [17] [18] [19] [20] [21] [23]. These references are mentioned as a courtesy to the reader.

This report describes the automated system as it existed in early 1989. In 1989 several changes were made to improve measurement accuracy and utility. A description of the updated system is given in Reference [22]. The three most important changes are;

1. The wooden boom was replaced by a lighter, more rigid, and smaller profile aluminum box beam.
2. A second, smaller azimuth positioner was added to allow fixed angle bistatic measurements.
3. The locations of the receive and transmit antennas were interchanged and the receive signal was mixed down to IF frequency at the antenna. This reduced phase error and enhanced signal to clutter ratios significantly.

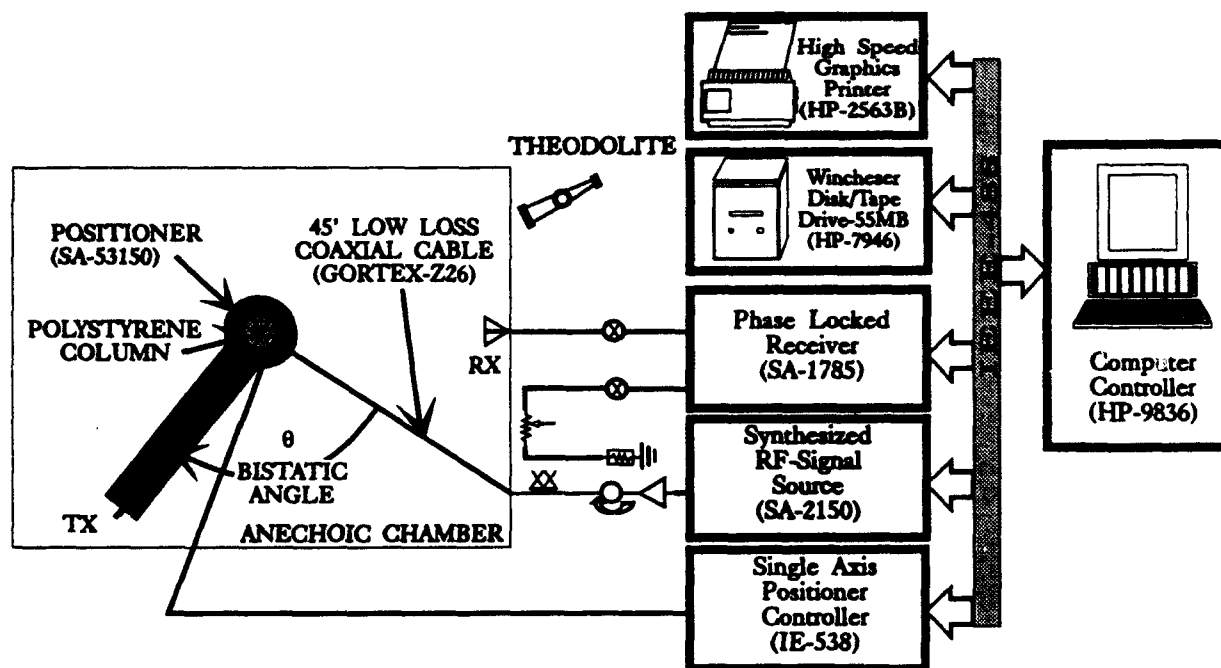


Figure 2: ASBSMS System Component Layout and Measurement Geometry

2 SYSTEM OVERVIEW AND THEORY

The ASBSMS consists of six major subsystems: anechoic chamber, receiver, transmitter, positioner, target aligner, and system controller. The system components are organized as illustrated in Figure 2. The target is supported by a conical polystyrene column glued to a trussed wooden boom directly over the center of rotation of the azimuth positioner. At the far end of the boom the transmit antenna is attached so that the boresight axis is parallel to the chamber floor and passes just above the polystyrene column. The receive antenna is mounted on a metal plate that is attached to the chamber wall. The boresight axis of the receive antenna is parallel to the floor and intersects the transmit antenna boresight axis just above the target support column. Target and antenna alignment is achieved by use of a surveyor's theodolite.

Electromagnetic energy is coupled to the transmit antenna by means of a phase-stable low-loss coaxial (GORTEx-Z26) cable. The cable runs in a trough along the chamber floor below the absorber, passes up through a hole at the center of rotation of the azimuth positioner, thence inside the boom and up behind the antenna support, where it attaches to the transmit antenna. A service loop is provided in the cable before it passes up through the azimuth positioner to avoid phase variations caused by cable twist. Monitoring the shorted cable with a network analyzer while cycling the boom through 180° showed a two-way phase change of less than 1° at 10 GHz.

An isolator and a directional coupler lie between the source and the low-loss cable. The isolator prevents the signal reflected by the antenna from coupling into the reference path.

The directional coupler provides a stable reference signal to the receiver. The reference path variable attenuator is used to control the reference signal amplitude. This control prevents over driving the receiver and allows for maximum receiver accuracy. Depending on the power requirements, an RF amplifier can also be inserted in the circuit. The receive antenna (usually a horn or center-fed dish) couples the co-polarized component of the total field present in the chamber into the receive branch of the system. The received signal is routed through an isolator before entering the signal channel of the receiver to minimize errors due to antenna mismatch. The receiver and the azimuth positioner are controlled by a microcomputer.

Typically, data are collected automatically by positioning the boom to zero bistatic angle (see Figure 2), commanding the azimuth positioner (target and transmit antenna assembly) to rotate continuously at a constant angular velocity, and triggering the receiver to take a field sample at regular angular intervals. Both amplitude and phase are recorded.

Continuously moving the target-transmit antenna boom assembly and measuring "on the fly" instead of moving and stopping before each field sample is done because automated control of the boom acceleration is not precise enough to ensure the necessary position repeatability from measurement to measurement.

The collected data are proportional to the total electric field aligned with the polarization of the receive antenna. This field, E_t , is made up of four or two components, depending on whether or not a target is present. If a target is present, then E_t is the phasor sum of the direct coupling from the transmit antenna (E_d), the field scattered by the chamber (E_a), the field scattered by the target (E_s), and a multipath field (E_m). The multipath field arises from scattered energy that illuminates the target and perturbs the currents set up by the direct energy. If no target is present the target scattered field term is zero. Equation (1) describes the total field when the target is present, and Eq. (2) describes the total field in the empty chamber.

$$E'_t(\theta) = E_d(\theta) + E'_a(\theta) + E'_m(\theta) + E'_s(\theta) \quad (1)$$

$$E_t(\theta) = E_d(\theta) + E_a(\theta) \quad (2)$$

The prime indicates the presence of the target and θ is the bistatic angle. The multipath field, E'_m , and the chamber scattered field, E'_a , depend on the target.

In theory, the chamber scattered fields, $E'_a(\theta)$ and $E_a(\theta)$, differ because the target blocks a portion of the incident field. This blockage changes the illumination of the chamber environment directly behind the target. The severity of change depends strongly on the reflection properties of the shadowed chamber environment, the target size, the distance from transmit antenna to shadowed chamber environment to receive antenna, and whether the shadowed region scatters co-polarized energy in the direction of the receive antenna. In a swept-bistatic angle system, this unavoidable change in the chamber scattered field is negligible for sectors away from backscatter because the shadowed portion of the absorber-lined chamber does not radiate strongly into the receive antenna. In the

backscattering sector, the chamber field change can be made negligible for most targets by adding a thicker layer of pyramidal absorber to the directly illuminated portion of the chamber wall. The multipath field, $E'_m(\theta)$ becomes appreciable if the target introduces a

significant source of reradiation directed toward a chamber object with high backscattering cross section (for example the positioner) or vice versa. The size of the multipath field depends strongly on the illuminated (or shadowed) chamber environment, target scattering characteristics, the distance from the transmit antenna to chamber environment to receive antenna, and whether the illuminated region scatters co-polarized energy in the direction of the receive antenna. For the typical target this contribution to the multipath field can be kept small by mounting the target several wavelengths (about 5 to 10) above the positioner, and placing a flat disk of tuned absorber between the polystyrene foam column and the positioner. Since there is no way to decouple E_a and E_d with our CW system, we combine them and name the result the background total field, $E_b(\theta)$. With these considerations we can rewrite the expression for the total field as follows:

$$E_t(\theta) = E'_b(\theta) + E'_m(\theta) + E'_s(\theta) \quad (3)$$

$$E_t(\theta) = E_b(\theta) \quad (4)$$

The measured scattered field of the target is obtained by subtracting Eqs. (3) and (4), which results in,

$$E_s^M(\theta) = E'_s(\theta) + E'_b(\theta) - E_b(\theta) + E'_m(\theta) \quad (5)$$

We can see from Eq. (5) that the measured scattered field, $E_s^M(\theta)$, differs from the true scattered field, $E'_s(\theta)$, by the multipath field, $E'_m(\theta)$ and the residual¹ background field, $E_b^A(\theta) = E'_b(\theta) - E_b(\theta)$. If $E'_m(\theta)$ and $E_b^A(\theta)$ can be kept small then the measured scattered field will be a very good estimate of the true target scattered field. In theory this background subtraction technique is valid for situations where the background is not changed significantly by the introduction of the target.

3 OPERATING PROCEDURES

The measurement objective is to collect reliable total and background fields to be processed off-line on a mainframe computer. The background fields must be representative of the background component of the associated total field. This requires that the background remain stable for the time it takes to collect each measurement set. An unstable background leads to large errors in the measured scattered field [5]. A reliable measurement involves the three distinct operations, aligning the target, collecting data, and assessing system performance. These operations are employed as described in the flow diagram of Figure 3. First, measure the background field. Second, place the calibration target onto the polystyrene target support column inside the chamber without disrupting the absorber or other chamber objects, especially those immediately surrounding the target support column. Third, collect the calibration target total field. Fourth, carefully remove the calibration target. Fifth, again measure the background field. Sixth, using the background fields collected in steps one and four, perform a data quality check (described below). Seventh, place the target of int

¹See Appendix C for measured estimates of the residual background level at 10 GHz.

inside the chamber and align it. Eighth, collect the target total field. Ninth, carefully remove the target from the chamber. Tenth, measure the target background field. Repeat steps seven, eight, nine, and ten, for different targets or target orientations, as prescribed by the particular measured program. Before ending the measurement session repeat steps one through six. If the data quality check is negative repeat the entire measurement session.

The target alignment operation requires adjusting three angles: pitch (η), azimuth (α), and roll (ρ). The pitch and roll axes are fixed to the target and the azimuth axis is coincident with the vertical axis (y-axis) passing through the center of rotation of the measurement system positioner. Figure 4 defines these angles with three views: plan, side, and end. The method used to obtain the proper orientation depends on the target geometry. The tools available to obtain alignment are the theodolite and various gauges. Alignment is a two person job, requiring one person to sight the target through the theodolite telescope and the other person to make adjustments at the target location. One technique to provide all three degrees of target alignment is to glue the target to a polystyrene sphere (Figure 5). A shallow cylindrical hole in the target support column, of radius slightly less than the radius of the polystyrene sphere, accepts the sphere and allows unlimited (360°) aspect variation and limited pitch and roll variations. The proper aspect angle, α , is obtained by rotating the boom assembly to α° off the transmit antenna theodolite boresight. Once there, a second person sights through the theodolite along a convenient target edge and instructs the first person to adjust the target position until proper alignment is achieved. This technique is illustrated in Figure 6. Pitch and roll alignment are achieved by holding up against a convenient target edge, a gauge with edges or scribed lines that make the desired angle. A second person sights through the theodolite, giving instructions to the first person to move the target and gauge until proper alignment is obtained. This alignment procedure requires that the center of the target move for pitch and roll variations. The target scattered field phase data must be corrected for the error incurred by the moving target center to maintain phase consistency from measurement to measurement. We reference all phase measurements to the origin of the measurement system (a point that does not vary with bistatic angle). The correction required to make a rolled or pitched target scattered field phase consistent with that of a 0° -roll, 0° -pitch target orientation is given in Eq. (6).

$$\phi_s^{M_o}(\theta) = \phi_s^M(\theta) - a \sin(\gamma) g_\gamma(\theta), \quad (6)$$

where a is the radius of the polystyrene sphere to which the target is attached, $\phi_s^M(\theta)$ is the measured phase for the pitched or rolled target, $\phi_s^{M_o}(\theta)$ is the corrected phase referenced to the system origin, and

$$g_\gamma(\theta) = \begin{cases} \cos \theta & \gamma = \eta, \rho = 0 \quad (\text{pitch variations}) \\ \sin \theta & \gamma = \rho, \eta = 0 \quad (\text{roll variations}) \end{cases} \quad (7)$$

Equation (6) is valid only for cases where we vary pitch while holding $\rho = 0^\circ$, or we vary roll while holding $\eta = 0^\circ$.

The data are collected by first insuring that the chamber contains a properly aligned target (or is empty for background measurements) and the chamber door is closed. Next the

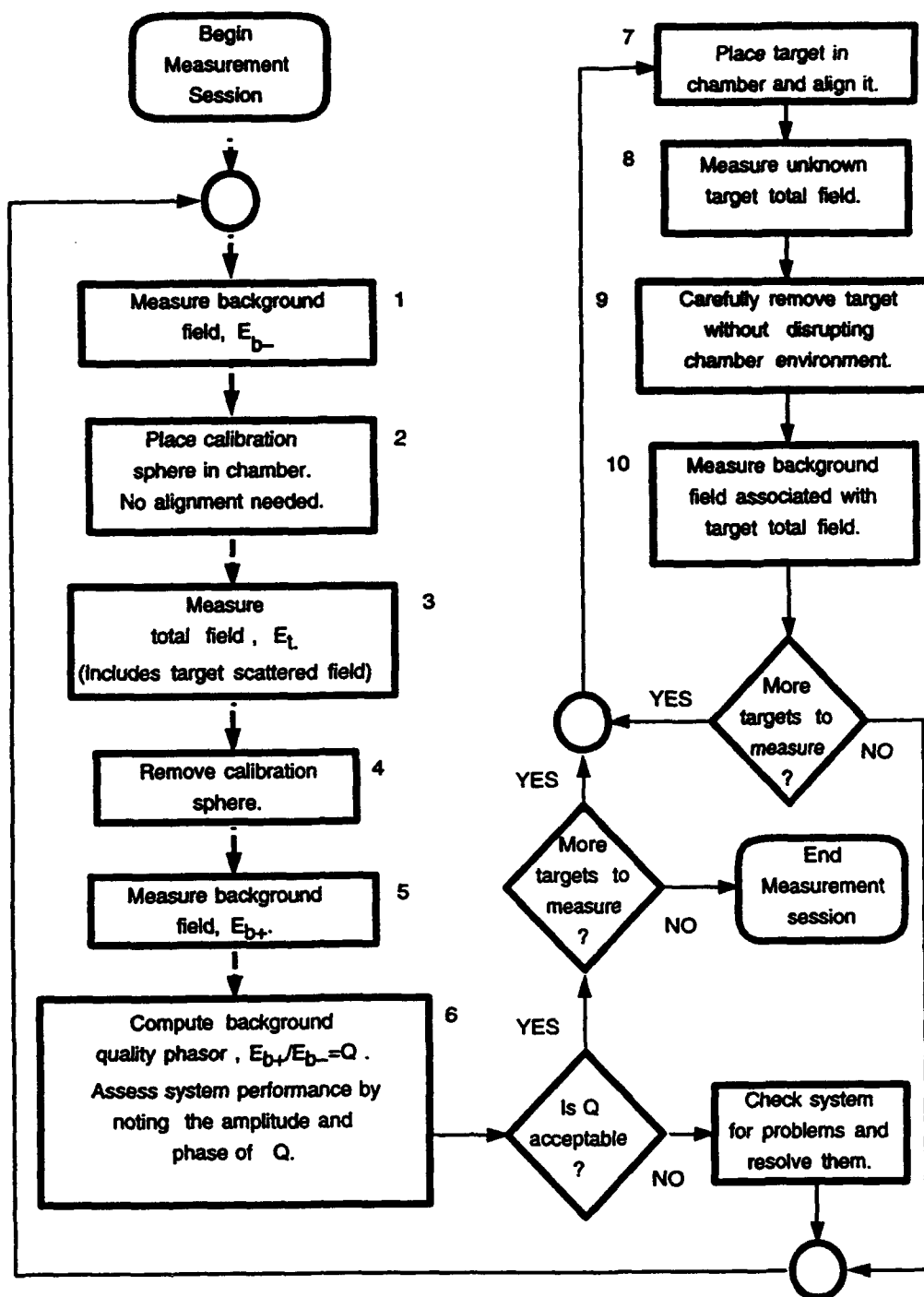


Figure 3: ASBSMS Diagram Summarizing the Measurement Procedure

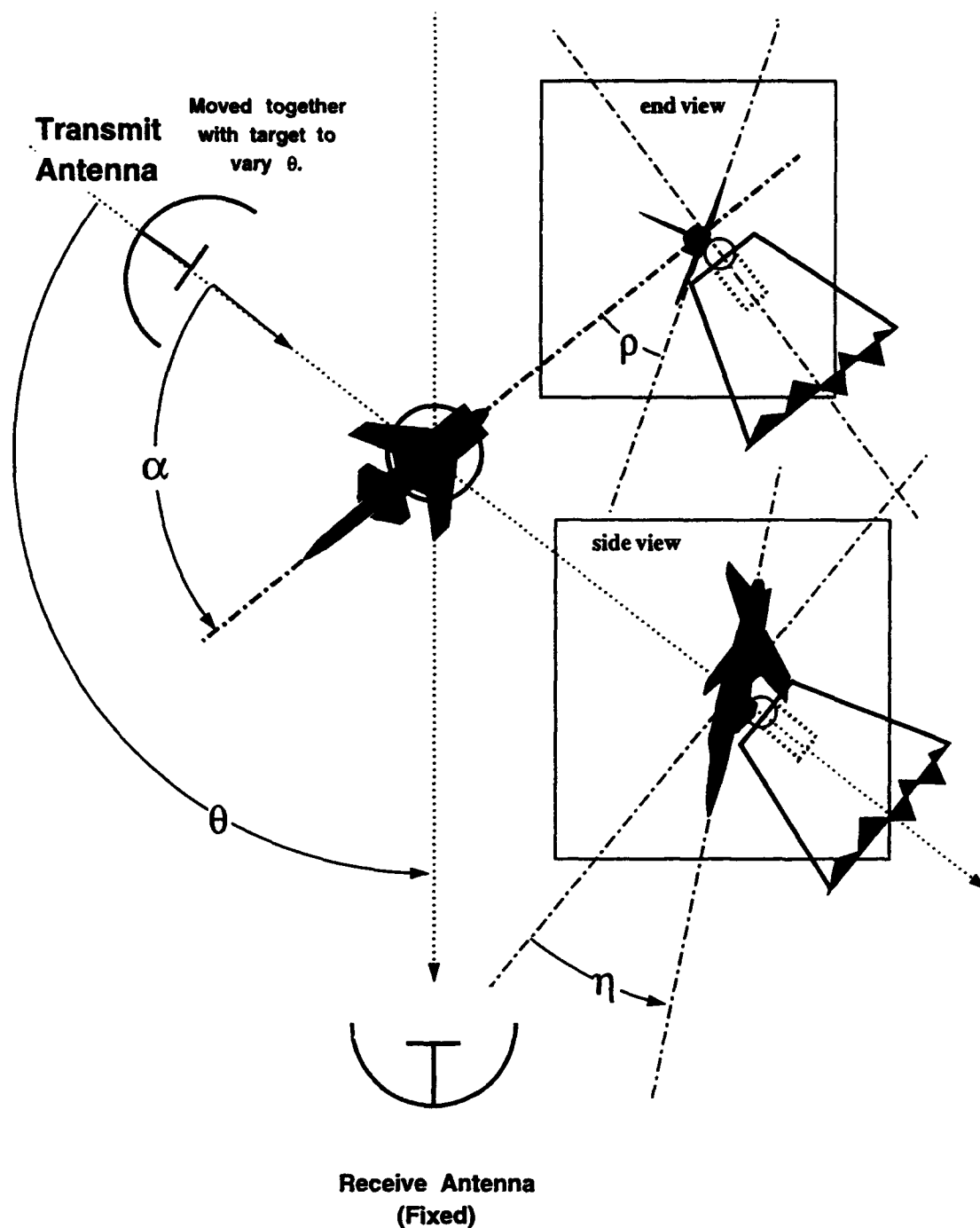


Figure 4: Measurement Geometry Shown in Plan View and Target Orientation Geometry Shown in the Three Views - Plan, Side, and End

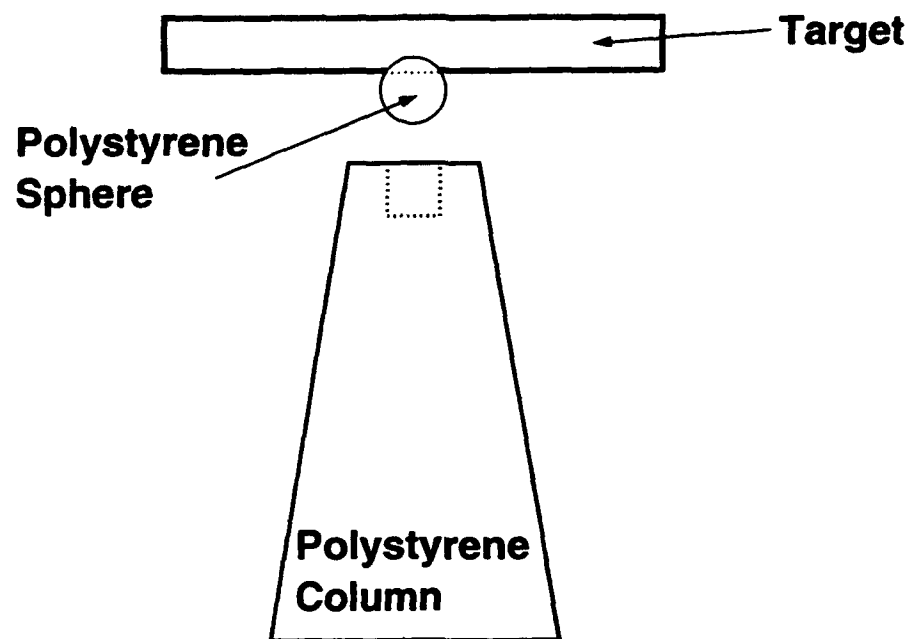


Figure 5: Polystyrene Foam Target Support Pedestal and Target Orientation Apparatus

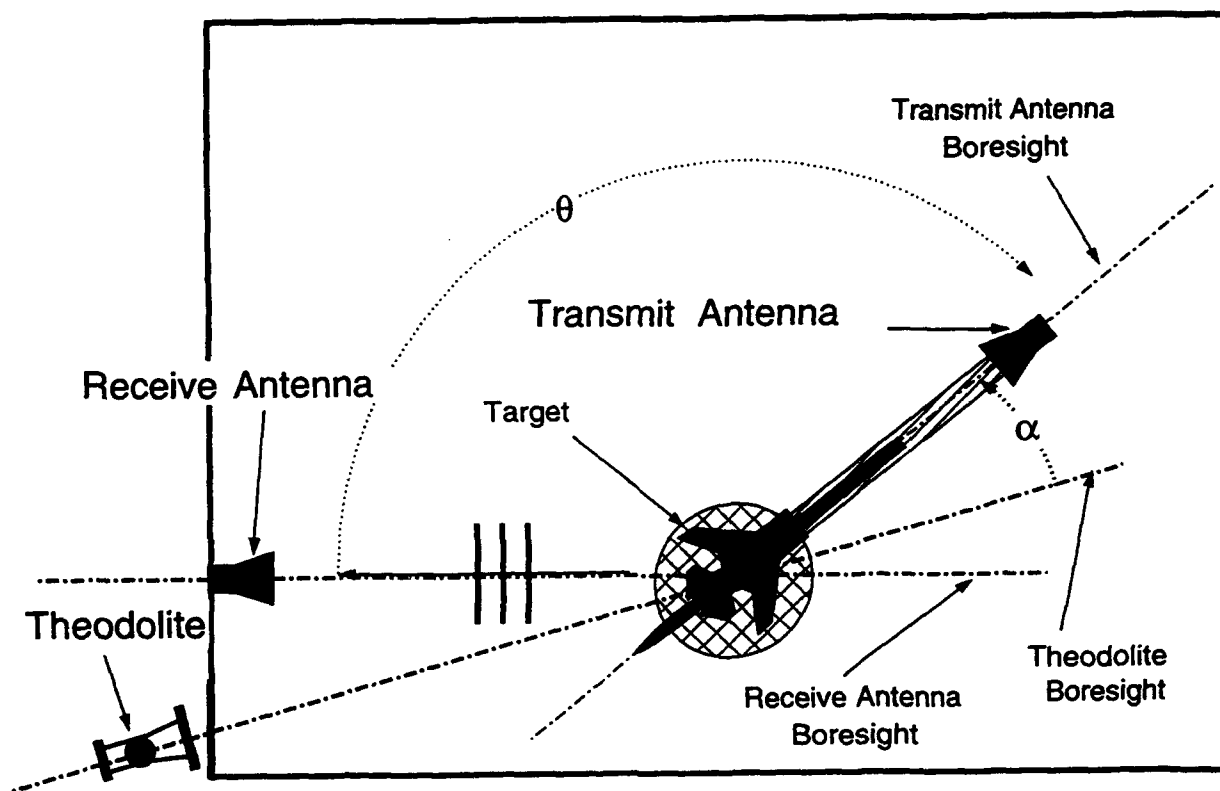


Figure 6: Target Alignment Geometry

operator enters the desired measurement parameters into the computer² controller and commands the computer to begin the automated measurement run. The computer determines the position of the transmit antenna, moves it to a location one sample window before the start angle, and starts the transmit antenna/boom assembly rotating clockwise at a constant angular velocity. The computer monitors the boom position (bistatic angle) by continually reading the pedestal controller display via the IEEE-488 bus. When the bistatic angle is within $\frac{1}{2}$ sample window of a desired sample angle the computer sends a trigger command to the receiver, causing the receiver to begin the sampling cycle. During the sampling cycle the transmit antenna continues to move, increasing the bistatic angle. The computer must wait for the sampling cycle to complete before it can begin monitoring the position again; therefore, the choice of positioning speed is limited by the receiver sampling time, and the measurement sample is an average of the field over the sampling window. Once a sample is obtained, it is put immediately into the computer's RAM memory in a binary format instead of taking the extra time to write the data onto the system hard disc. This is done to minimize the sampling time and therefore a maximum number of data can be collected (recall that we are measuring on the fly, so increasing the sampling time would require enlarging the sampling interval). After all data are collected they are converted from binary format to Hewlett Packard Basic real number format and written into a data base file on the system hard disc. Control of the computer is then returned to the operator. The time required for a measurement run depends on the sampling window. Typically, we choose a 0.1 degree sampling window for a 0.2 degree step angle. For these choices the measurement run takes about 25 minutes, collecting data over the entire observation sector ($0^\circ \leq \theta \leq 180^\circ$).

System performance is assessed to quantify the stability of the background at the time of measurement and to provide data for computing measurement error. This measurement quality check is accomplished by inspecting the ratio of two background electric fields measured close in time. The resulting background perturbation phasor, $\epsilon(\theta)$, should have a nominal amplitude variation of less than 10%, and a phase variation of no more than 10° , over most of the observation sector for X-band measurements. The actual level will depend on the frequency and the antennas, and will be slightly higher in the backscattering region. The background measurements used for the data quality check should be representative of the data from which the scattered field of the target will be extracted. In general, a target must be aligned as described previously, which usually disrupts the chamber environment enough to cause a significant change in the background field phase (the background field amplitude is not usually changed significantly). The target background is generally measured after the target is removed because removing the target is much less disruptive than aligning it and therefore the post-target measurement background is most representative of the actual background component of the total field collected in the presence of the target. The backgrounds taken immediately before and just after the calibration sphere total field

²A complete description of the measurement software (written in Hewlett Packard Basic 3.0) is reserved for another report. We describe here only the aspects of the software critical to the accurate collection of data.

measurements are used for the data quality check for two reasons. First, spheres, by virtue of their symmetry, are easy to place inside and remove from the chamber without significantly disrupting the chamber environment. Second, measuring the sphere simulates the collection time and level of disruption of the chamber that takes place during the target total field and background field measurements. This check can be repeated throughout the course of each measurement session to verify the proper operation of the measurement system, but should be done a minimum of twice every measurement session; once at the outset and once at the end.

4 CALIBRATING THE MEASUREMENTS

Calibrating the target scattered field data requires measuring the scattering from an object with a known scattered field. We use steel and aluminum spheres, exclusively. There are other objects, such as metal disks [6] and rectangular plates, that have known scattered fields to a high degree of accuracy in the specular directions. Although it is theoretically possible, we do not calibrate our system with such targets because they are difficult to align and slight misalignment can lead to large calibration errors, especially if the calibration targets are electrically large.

The calibrating process converts the target measured scattered fields from receiver units ($\sqrt{\text{watts}}$) to absolute units, in our case meters. A point calibration phasor, $\alpha(\theta)$, can be computed according to the equation:

$$\alpha(\theta) = \frac{E_{sc}^T(\theta)}{E_{sc}^M(\theta)} \frac{\text{meters}}{\sqrt{\text{watts}}} \quad (8)$$

where the superscripts M and T refer to measured and true data respectively, and the subscript c denotes the calibration target (in our case a steel or aluminum sphere).

$E_{sc}^M(\theta)$ is the calibration target measured scattered field computed from the measured calibration target total field, $E_{tc}^M(\theta)$, and the measured background field associated with it according to Eq. (5). $E_{sc}^T(\theta)$ is the square root of the true scattering cross section expressed in meters as computed from the Mie series solution [7]³. An example of data used to compute a typical point calibration phasor is shown in Figure 7. Figure 7[top] shows the true radar cross section⁴ of a perfectly conducting sphere with radius 2.86 wavelengths and the measured scattered field power of an aluminum sphere of the same radius. For clarity the measured amplitude curve was multiplied by a constant to make it approximately the same level as the theory curve. Figure 7[bottom] shows the true and measured phase curves of the scattered field for the same target. We notice by comparing the positions of the nulls in the true

³The computer program used to compute the true scattered field of the conducting sphere is a modified version of the program described in [7]. The program in that reference gives radar cross section only. Our version gives $\sqrt{\text{RCS}}$ and includes phase information

⁴The radar cross section is proportional to the square of the scattered field amplitude. We plotted RCS to give the reader an idea of the size of the scatterers that we are dealing with. When computing the point calibration phasor we use the $\sqrt{\text{RCS}}$ with phase data.

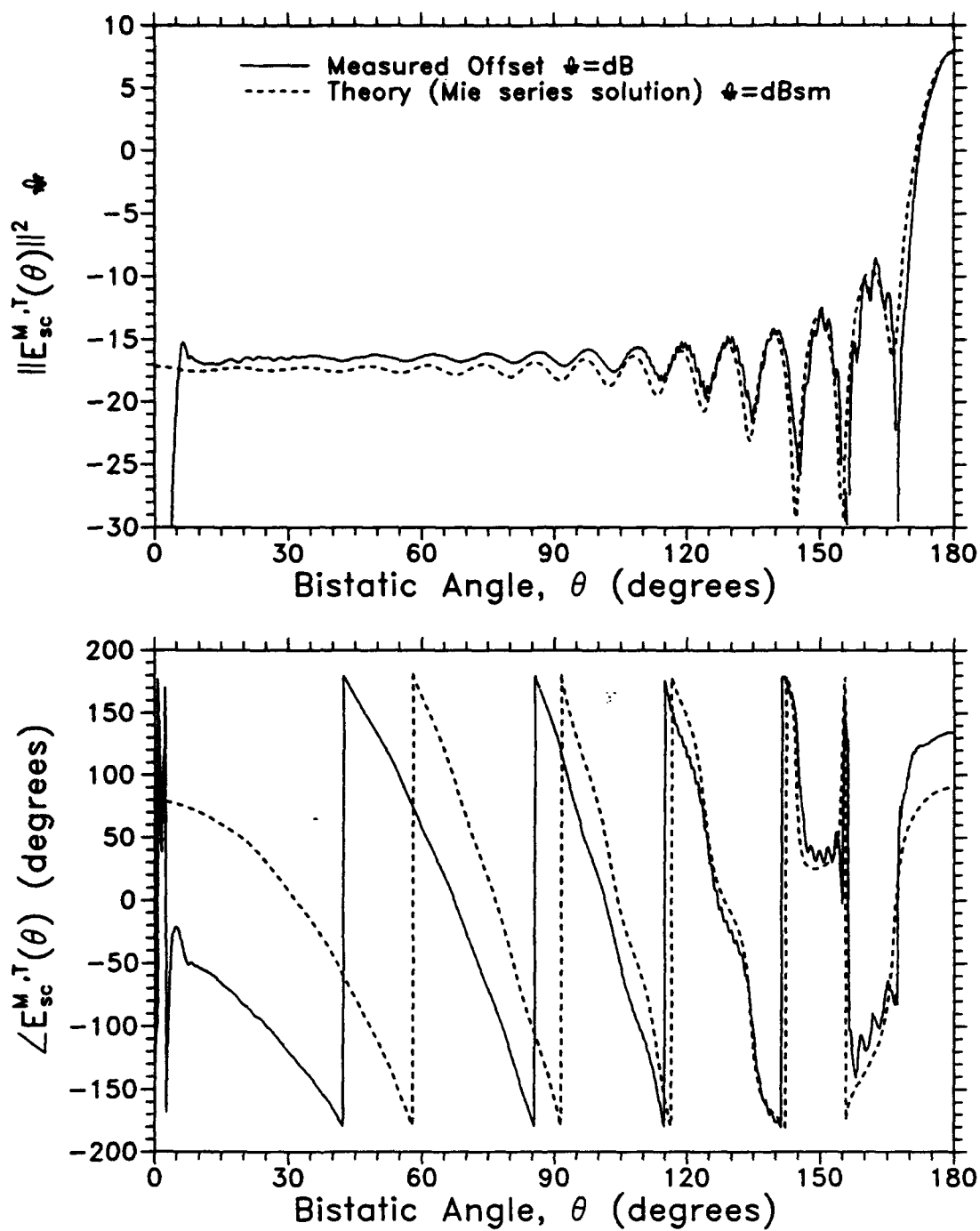


Figure 7: Scattering from a Perfectly Conducting Sphere, $ka = 18$

and measured amplitude patterns that the measured curve is shifted slightly relative to the true curve. This is because the observation sector that we set up was slightly different than the observation sector that we actually collected data over. In other words the bistatic angle read from the positioner controller display during the measurement was wrong by a constant. This problem can be easily remedied by shifting the measured curve so that it reflects the correct observation sector. This sliding of the measured data does not introduce errors provided the cause for the shift is due to improper zeroing of the positioner controller, as it is in this case, and not to improper aspect alignment. If the target is a sphere we can be confident that the displacement of the nulls is not due to improper aspect alignment because the target symmetry insures that the scattering is independent of aspect. For targets other than spheres, apparent constant null offsets could be due to misalignment of the target aspect. We must insure that the shift is a constant offset of the entire pattern and not a shift that changes with bistatic angle in order to attribute the shift to improper zeroing. Before calibrating we must determine the particular shift caused by improper positioner zeroing so that we can shift the data accordingly. Once the angular offset is determined, future measurements can be corrected as they are recorded in the measurement system data base. There are at least two ways to determine how many degrees in bistatic angle our zeroing error has shifted the pattern. One way is to carefully compare the positions of the deepest and sharpest nulls of the true and measured scattering patterns and compute the angular offset from the difference between the bistatic angle positions of corresponding nulls. The second method, which we used, is to compute a set of point calibration phasors according to Eq. (9).

$$\alpha_{\nu}(\theta) = \frac{E_{sc}^T(\theta)}{E_{sc}^M(\theta + \nu)} \quad (9)$$

where ν indicates an offset angle. We compute calibration phasors for a series of offset angles, plot their amplitude as a function of bistatic angle, and compare the curves. The flattest curve indicates the best match between true and measured scattering patterns and we choose the offset angle that corresponds to that curve. Figure 8 shows typical point calibration phasors (amplitude and phase) as a function of bistatic angle. The solid curves show the point calibration phasor computed from the curves plotted in Figure 7 with no offset ($\nu = 0^\circ$). The dashed curves show the phasor computed from the curves given in Figure 7 but with the measured curve offset in θ by eight tenths of a degree ($\nu = +0.8^\circ$). We see that the offset curve is flatter over a larger bistatic sector than the non-offset curve. In the backscattering region ($0 \leq \theta \leq 5^\circ$) the point calibration phasor amplitude and phase curves deviate from a constant level. This deviation occurs because the transmit antenna passes directly in front of the receive antenna so that the receive antenna sees mostly the back lobes of the transmit antenna radiation and very little scattering. The calibration phasor in the backscattering region is erroneous and should be ignored. We concentrate on the dashed curves, which have been corrected for positioner zeroing error. From about $\theta = 10^\circ$ to $\theta = 90^\circ$ there is a relatively flat region that corresponds to the slowly varying portion of the amplitude pattern of the sphere (Figure 7[top]). For $\theta > 90^\circ$, the calibration phasor begins to diverge, showing large deviations from the expected constant level. The largest

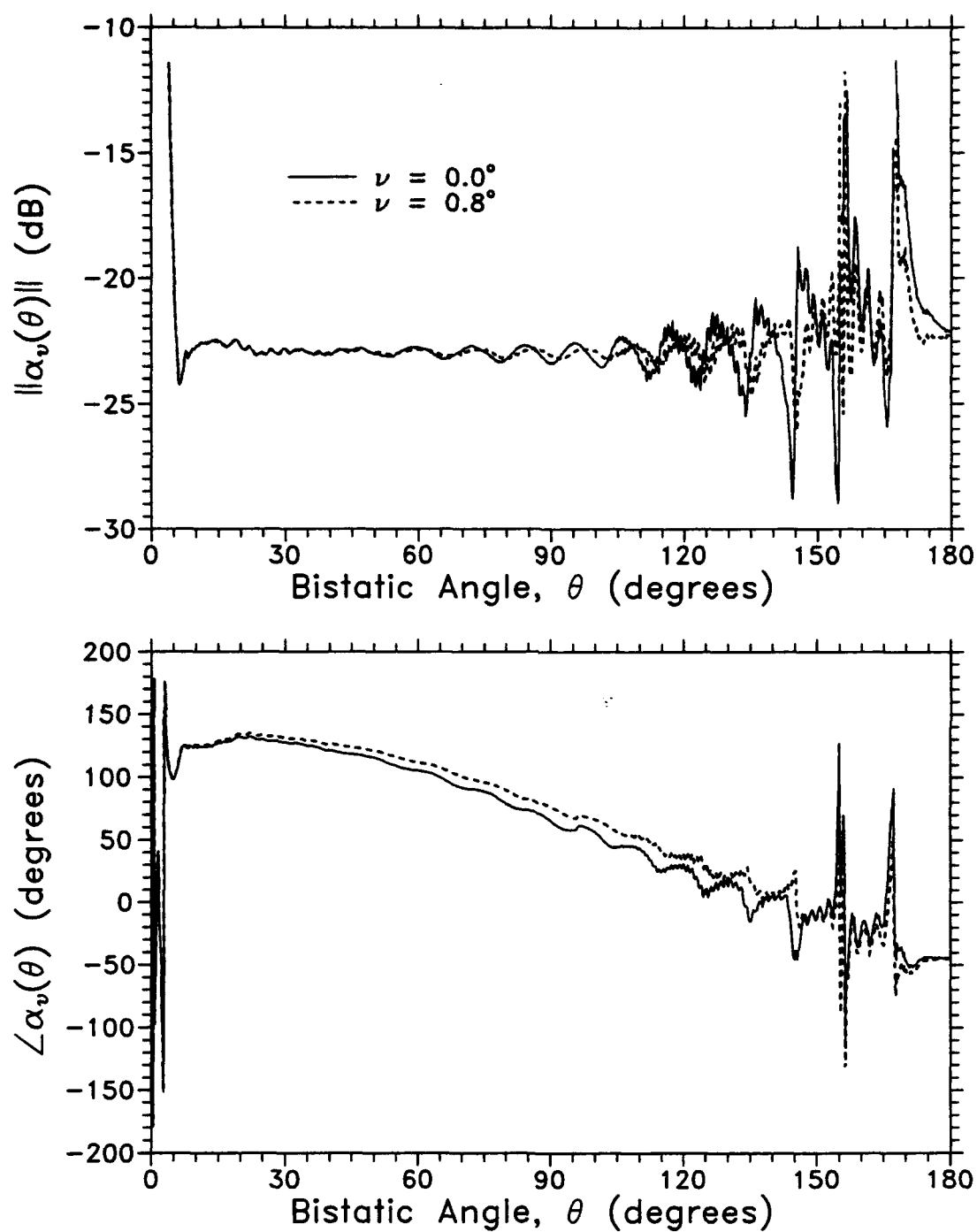


Figure 8: Typical Point Calibration Phasors Computed from Unshifted Measurements (No Offset), and Computed from Measurements Shifted 0.8° Relative to the Exact Solution

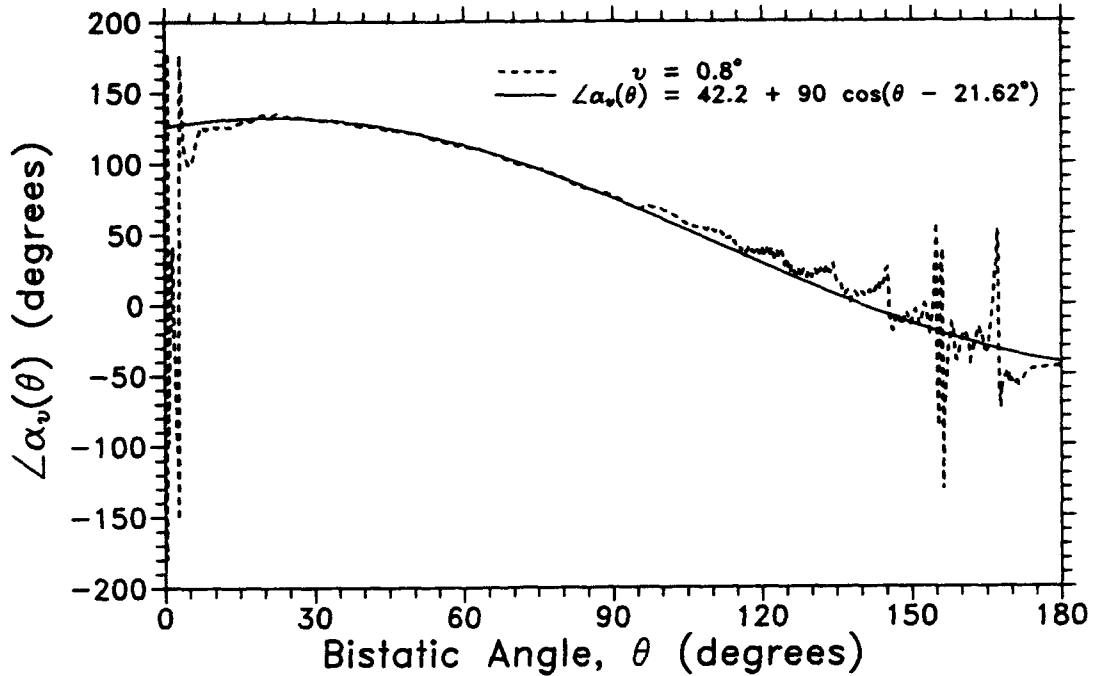


Figure 9: Phase of the Point Calibration Phasor and Best Fit Curve

deviations correspond to nulls in the amplitude pattern of the sphere (Figure 7[top]). These large deviations in the forward scattering region occur because we cannot determine the position at which samples are taken accurately enough to reconstruct the rapidly changing slope in the deepest of nulls. The phase curve (dashed in Figure 8[bottom]) outside of the backscattering and forward scattering regions displays a slowly varying cosine behavior. Closer inspection shows that this behavior varies according to the relation:

$$\arg[\alpha(\theta)] = c + c' \cos \theta + c'' \sin \theta, \quad (10)$$

where c , c' , and c'' are constants. In this case $c = 42.16^\circ$, $c' = 83.70^\circ$, and $c'' = 33.17^\circ$. These constants are computed by picking three points on the smooth part of the point calibration phasor phase-curve, writing an equation for each according to Eq. (10), and solving the resulting system for the three unknowns c , c' , and c'' . Figure 9 shows this curve plotted with the best fit point calibration phasor. We see that the match is very good in the region corresponding to the flattest portion of the amplitude curve of the point calibration phasor. The relation given in Eq. (10) is precisely what one would expect for the phase variation in the scattered field of a target that was offset from the center of rotation of the measurement system by a small amount as shown in Figure 10. A more general and perhaps more useful expression for the phase of the point calibration phasor is:

$$\arg[\alpha(\theta)] = c_o + k\delta \sin(\theta - \beta), \quad (11)$$

where δ is the radial displacement of the target from \mathcal{O} in the measurement plane, k is the free space wave number, c_o is a constant, and β is the angular deviation of the target

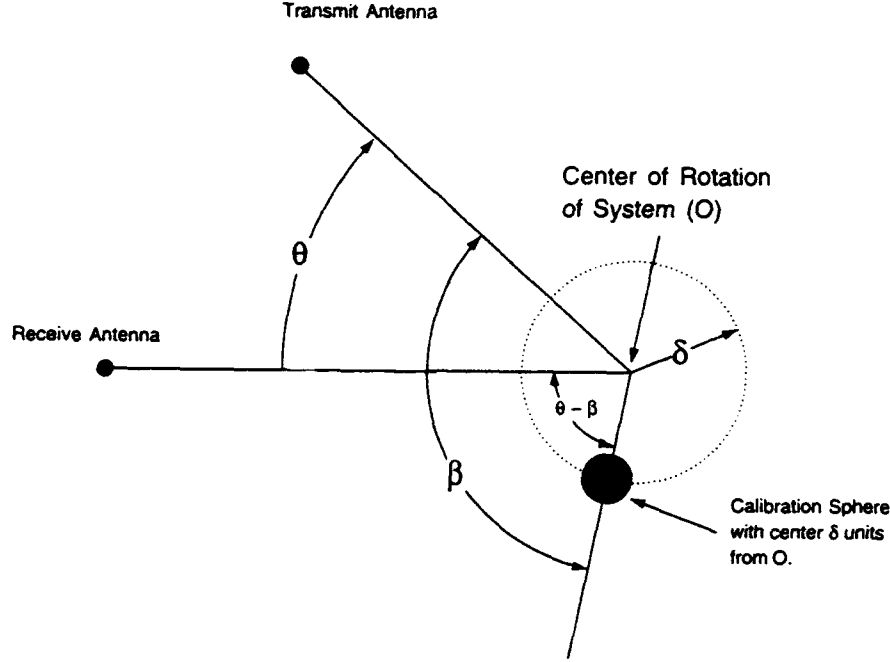


Figure 10: Measurement Geometry with Calibration Sphere Displaced

from the incident energy direction (see Figure 10). Expressed as in Eq. (11), the phase of the point calibration phasor allows us to compute the alignment offset, δ . Expanding the cosine function in Eq. (11) and comparing the results with Eq. (10) we find that $c = c_o$, $c' = k\delta \cos(\beta)$, and $c'' = k\delta \sin(\beta)$. In the present example we compute that the calibration sphere was displaced from the center of rotation of the system by $\delta = 0.667(1.78\text{cm})$, and $\beta = 21.62^\circ$. For our immediate purpose we are concerned only with correcting the phase of the measured target scattered field and so we leave Eq. (11) for the readers reference.

If the point calibration phasor were better behaved in the forward scattering direction we might have been able to apply it directly to calibrate the unknown target scattering at each measurement point. In doing so we would immediately calibrate out the receiver non-linearity and phase variation due to the target not being centered at the measurement system center of rotation. Because of the wild behavior, however, we must instead compute a single average calibration phasor, α_o , by averaging the best fit point calibration phasor over the flattest portion of the curve as given in Eq. (12).

$$\alpha_o = \frac{1}{(N - N_o)} \left(\sum_{n=N_o}^N |\alpha_n(\Delta\theta n)| \right), \quad n = \{0, 1, 2, 3 \dots\}. \quad (12)$$

In Eq. (12), $\Delta\theta$ is the sampling interval (typically, $\Delta\theta = 0.2^\circ$), and N_o and N are the indices corresponding to the bounding angles over which to average the point calibration phasor. We calibrate the unknown target measured scattered field according to Eq. (13),

where superscript C indicates the calibrated data.

$$E_s^C(\theta) = E_s^M(\theta)\alpha_o \exp[-i(c + c' \cos \theta + c'' \sin \theta)] \quad (13)$$

The bracketed term in the exponent compensates for the phase variation due to the target not being centered on the center of rotation of the measurement system^{5 6} ($c' \cos \theta + c'' \sin \theta$), and calibrates the phase (c). For the example at hand we compute the average calibration phasor by summing the $\alpha_\nu(\theta)$ according to Eq. (12) over the bistatic angle sector $25.0^\circ \leq \theta \leq 90.0^\circ$ which, since $\Delta\theta = 0.2^\circ$ and the measurement sector was $0.0^\circ \leq \theta \leq 180.0^\circ$, requires that $N_o = 125$ and $N = 450$. Specifically we compute

$$\alpha_o = \frac{1}{325} \left(\sum_{n=125}^{450} \alpha_{\nu=0.8^\circ}(0.2 \times n) = 0.0682 \exp[i(111.0^\circ)] \right). \quad (14)$$

In the next section we will use this average calibration phasor to calibrate the example measurements presented there.

5 EXAMPLE MEASUREMENTS

The operating procedure described in Section 3 is applied to obtain the E-plane radar cross section of an aluminum cube with a $3/4$ wavelength (0.75λ) side length, for broadside incidence. An aluminum sphere of electrical size $ka = 17.95$ is used as a calibration target.

Figures 11-15 show the total field amplitude and phase curves for the measurements prescribed in steps 1 through 10 of the measurement procedure. Figure 11 presents the background total field taken prior to measuring the calibration target. Figure 12 shows the aluminum sphere total field. Figure 13 shows the background total field measured after the sphere total field measurement. Figure 14 shows the aluminum cube total field data. Figure 15 presents the background total field taken after the cube measurement. We notice that all but the sphere total field measurements look the same in the forward scattering region ($100^\circ < \theta < 180^\circ$). This occurs because the dominant contribution to the total field is the direct coupling between the transmit and receive antennas and this signal is present in all measurements. The sphere total field measurement shows a region of rapidly varying amplitude from about $\theta = 100^\circ$ to $\theta = 140^\circ$, which indicates that the magnitudes of the scattered and direct coupling components of the total field are on the same order. The background total fields show the typical rapidly varying phase indicative of the direct coupling path length change with bistatic angle. The typical target total field shows slowly varying phase at the low bistatic angles with an abrupt change to rapidly varying phase at some large bistatic angle (typically about 100°). This indicates the transition from target scattering dominance of the total field to direct antenna coupling dominance.

⁵This phase correction is made in addition to the phase correction required for non zero pitch and roll measurements, and applies to all measured scattered fields.

⁶The phase factor may be dropped from Eq. (13) if one is concerned only with RCS.

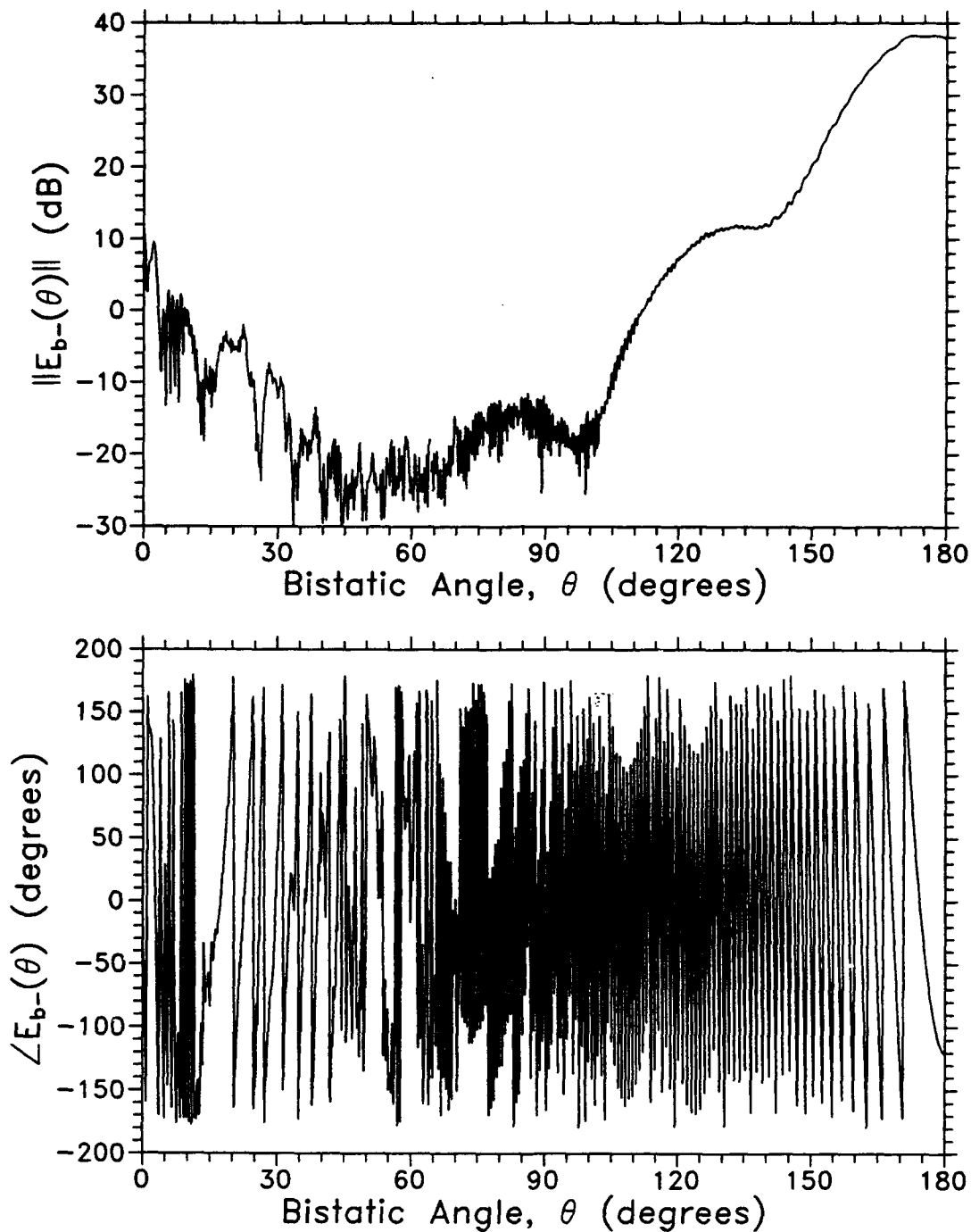


Figure 11: Amplitude and Phase of the Background Field Collected Prior to the Calibration Sphere Measurement. Measurement frequency is 10 GHz and the transmit and receive antennas were both 6 inch diameter dish antennas with dipole feed.

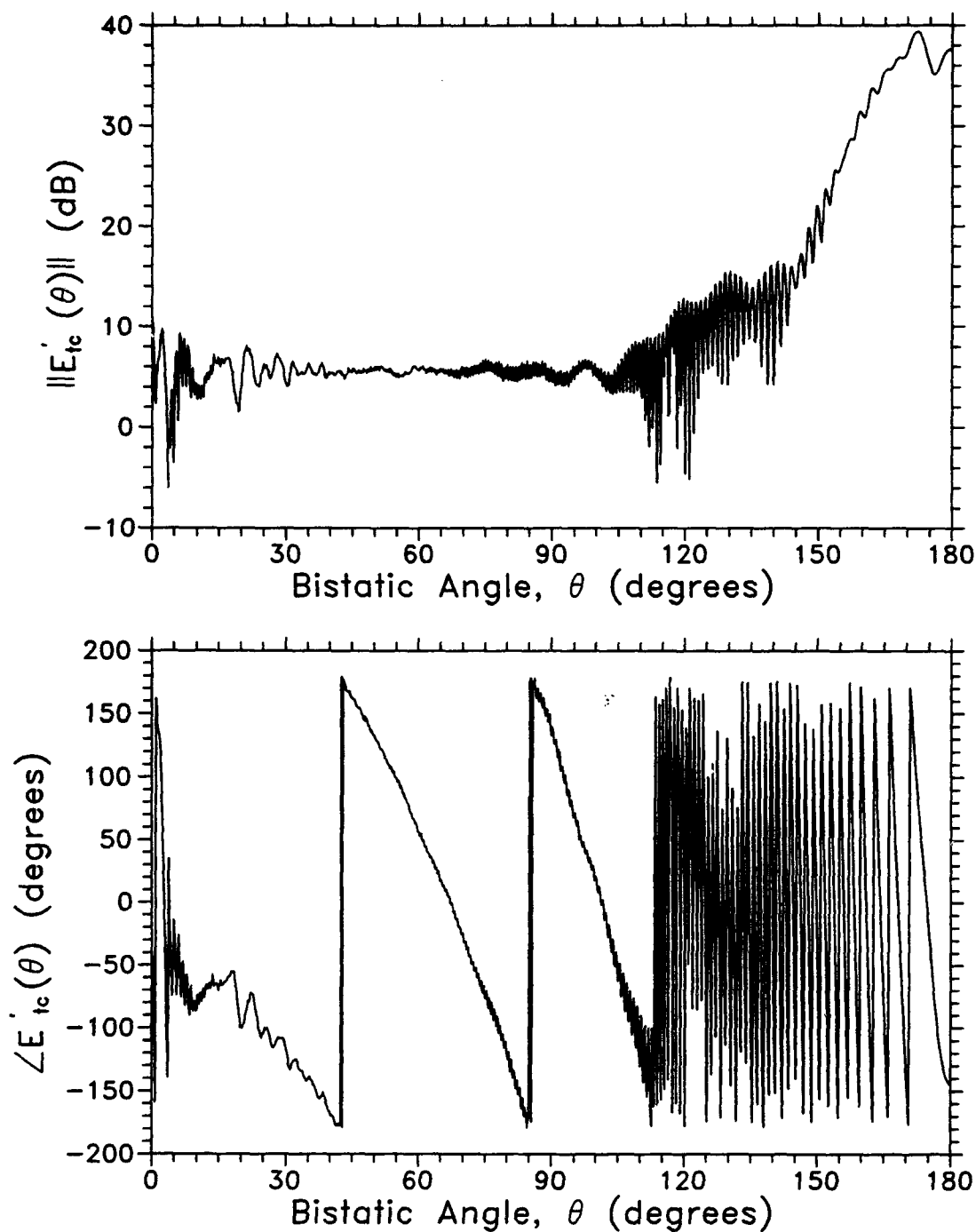


Figure 12: Measured Total Field of the Calibration Sphere ($ka = 18$). Measurement frequency is 10 GHz and the transmit and receive antennas were both 6 inch diameter dish antennas with dipole feed.

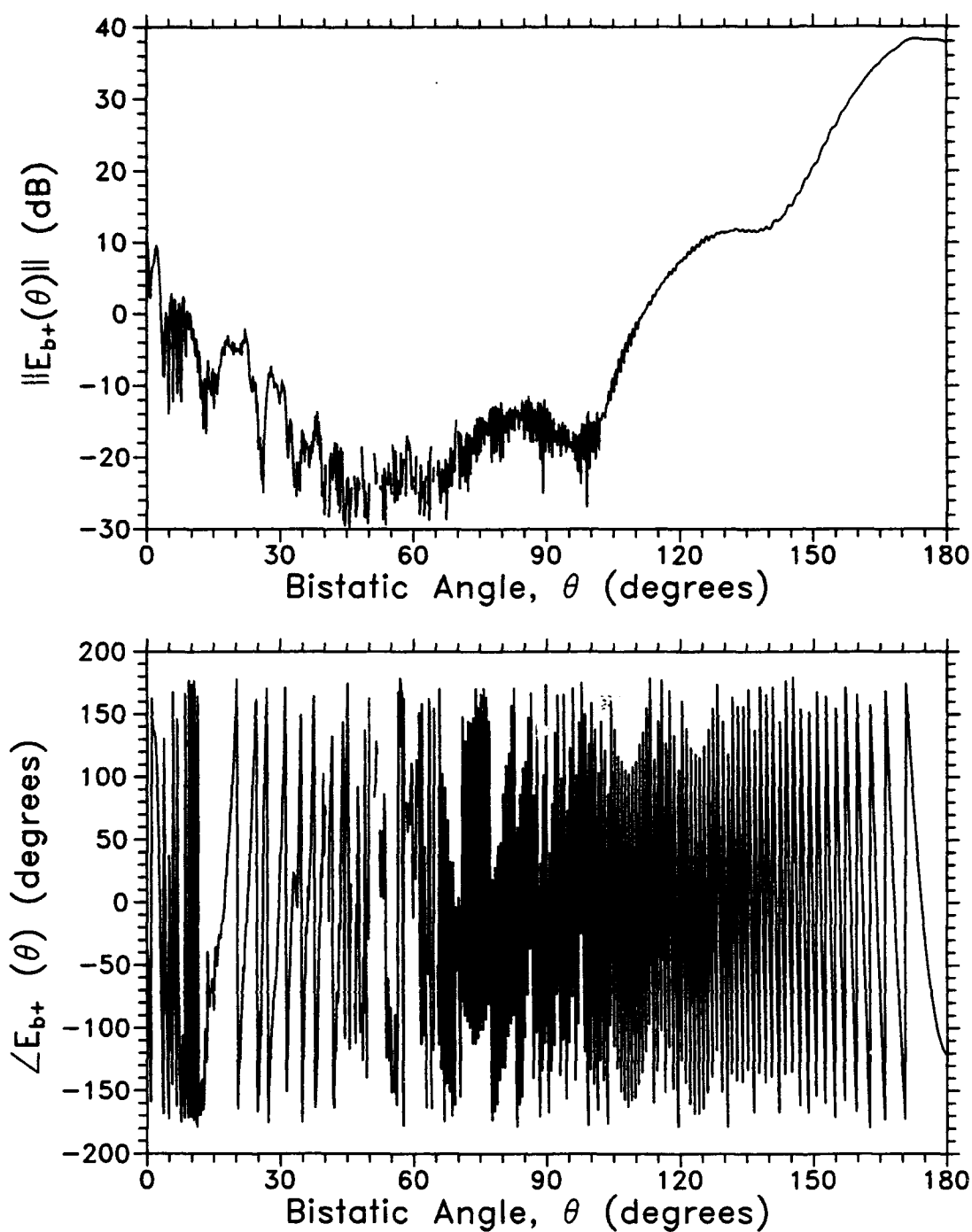


Figure 13: Amplitude and Phase of the Background Field Measured After the Calibration Sphere. Measurement frequency is 10 GHz and the transmit and receive antennas were both 6 inch diameter dish antennas with dipole feed.

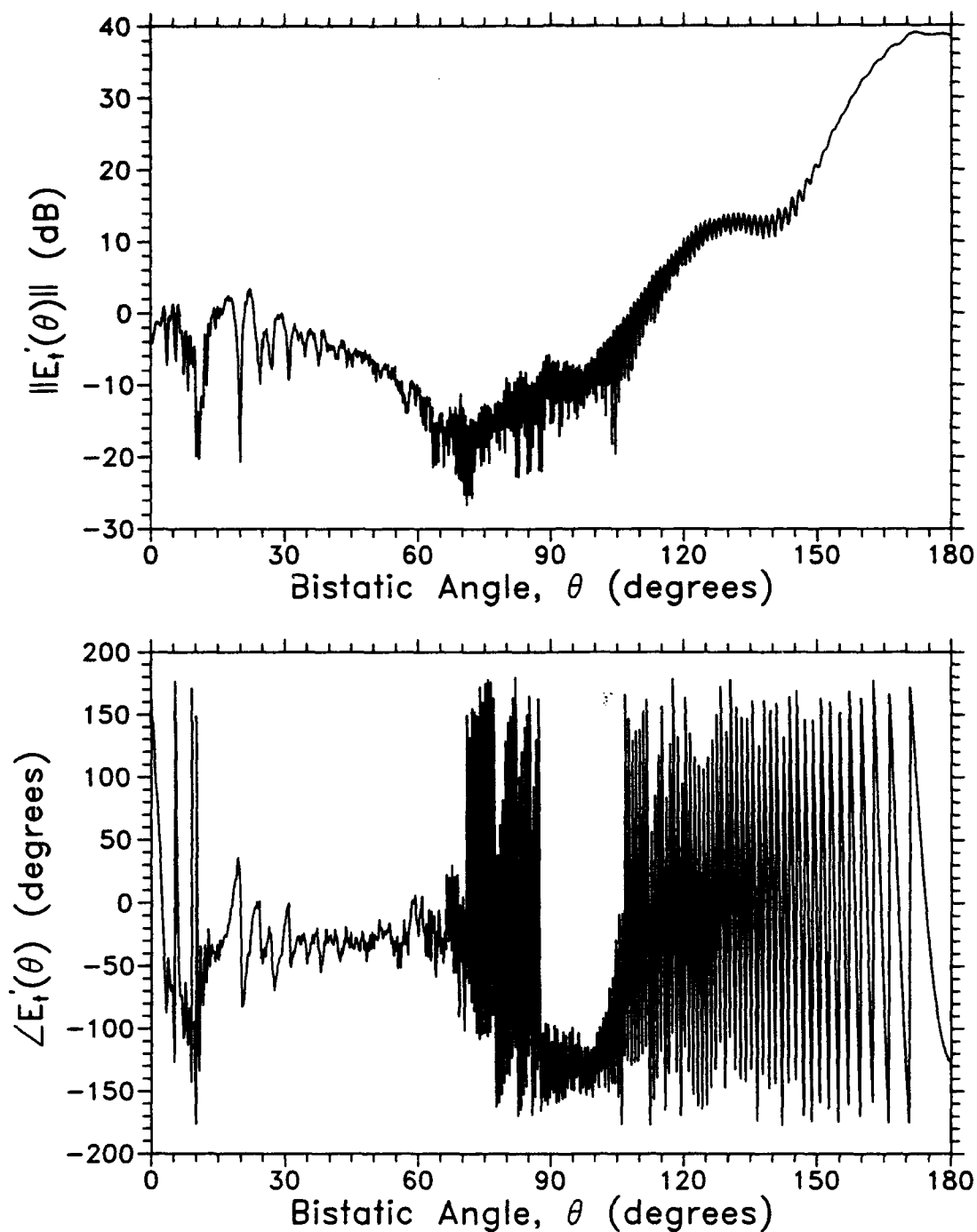


Figure 14: Amplitude and Phase of the Typical Measured Total Field. Here the target is an aluminum cube with side length 0.75λ . Measurement frequency is 10 GHz and the transmit and receive antennas were both 6 inch diameter dish antennas with dipole feed.

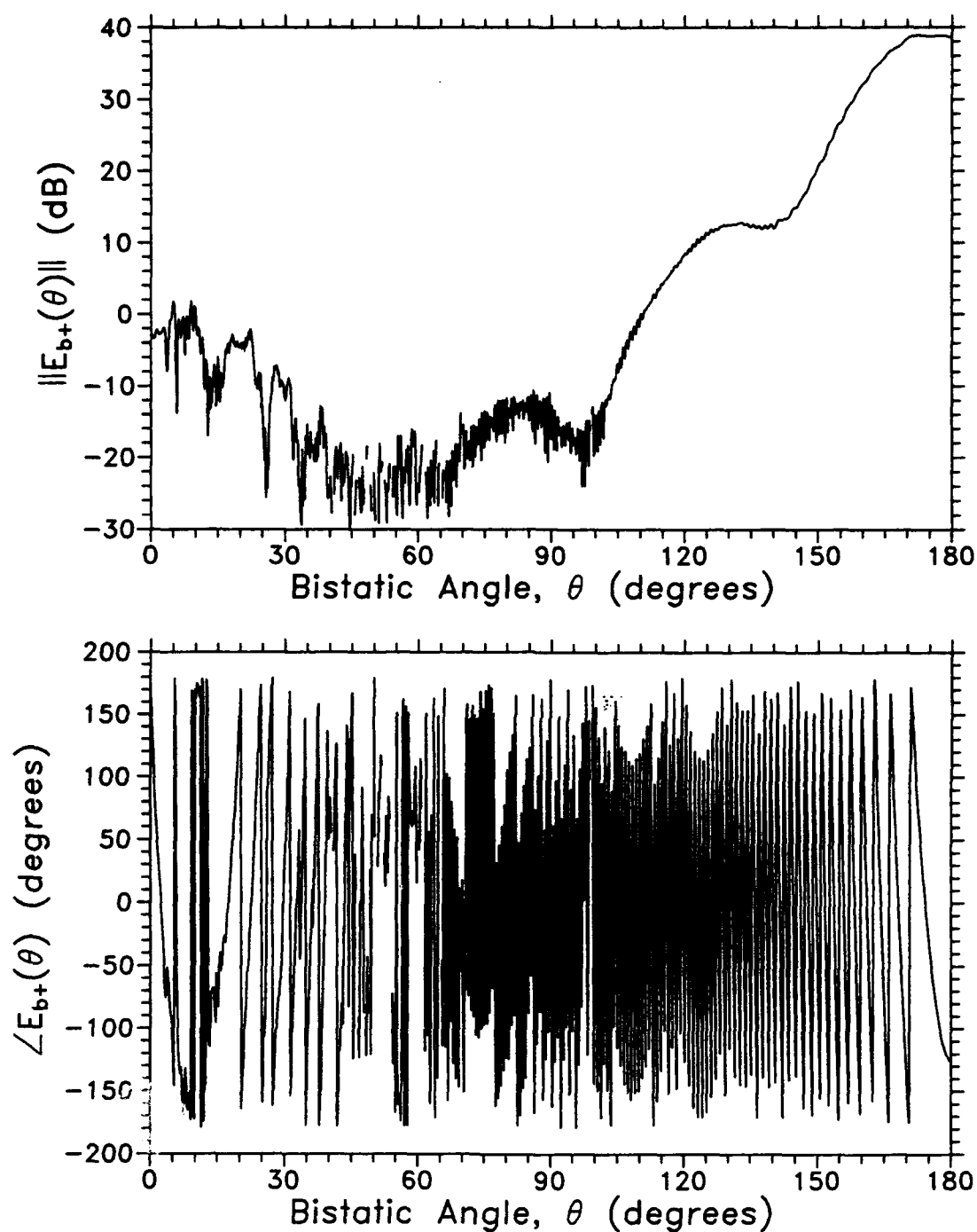


Figure 15: Amplitude and Phase of the Typical Measured Background Field. Measurement frequency is 10 GHz and the transmit and receive antennas were both 6 inch diameter dish antennas with dipole feed.

A measurement quality check is performed by computing the ratio of the two background total field measurements taken before and after measuring the calibration sphere total field. Figure 16 shows this background perturbation phasor, $\epsilon(\theta)$, computed from the background total fields shown in Figures 11 and 13. We can see from the figure that in the example at hand $\epsilon(\theta)$ ranges over $1.0 \pm 0.22(\pm 13^\circ)$. We have neglected the phase deviation of 120° that occurs around $\theta = 62^\circ$ because this is an isolated point and deviates greatly from the other values. It is common, however, to have isolated large excursions from the average value in the typical background perturbation phasor. This acceptable background perturbation factor is typical for X-band frequencies. With the raw measurements collected and acceptable, the cube scattered field can be extracted, calibrated, and assigned error bars. Figure 17 shows the calibration sphere measured scattered field, while Figure 18 shows the measured scattered field of the cube. From the calibration sphere measured scattered field we compute the average calibration phasor as described in Section 4 (recall $\alpha_o = 0.0682 \angle 111.0^\circ$). Inserting the values for the average calibration phasor, the three phase correction constants, $c = 42.16^\circ$, $c' = 83.70^\circ$, and $c'' = 33.17^\circ$ (computed in Section 4), and the raw cube scattered field data (Figure 18) into Eq. (13), we compute the calibrated cube scattered field. In a previous report [5] we presented an equation that estimates the relative error due to background instability when the approximate intensity of the scattered field, and the background perturbation phasor, $\epsilon(\theta)$ are known. The equation is repeated here for convenience,

$$U(\theta) = \frac{E_b(\theta)}{E_s^M(\theta)} \times [1.0 - \epsilon(\theta)], \quad (15)$$

$$\epsilon(\theta) = \frac{E_b(\theta)_-}{E_b(\theta)_+}. \quad (16)$$

The minus (-) and plus (+) signs indicate background measurements made before and after the calibration sphere measurement. From expression (15) we can see that the relative error is proportional to the background-total-field to target-scattered-field ratio and therefore varies as a function of bistatic angle.

To compute error bars for the calibration data we use a modified version of Eq. (15). Specifically, we compute an RMS perturbation phasor, $\epsilon_{RMS}(\theta)$, given by

$$\epsilon_{RMS}(\theta) = 1 + \left[\sqrt{\frac{1}{\pi} \int_{\theta-\Delta\theta}^{\theta+\Delta\theta} |1 - \epsilon(\theta)|^2 d\theta} \right] \exp \left[i \sqrt{\frac{1}{\pi} \int_{\theta-\Delta\theta}^{\theta+\Delta\theta} |\angle \epsilon(\theta)|^2 d\theta} \right], \quad (17)$$

and use a sliding window average of the background-to-scattered field ratio, $R(\theta)$. We choose the angular window, $\Delta\theta = \frac{4}{\Delta f}$, $\Delta f = 1.1k(a + \lambda)$ to be four times the inverse of the spatial frequency bandwidth [5], Δf , of the target to insure that the rapidly varying background field is smoothed while preserving the general structure of the measured scattered field. Computing the measurement error bars directly from Eq. (15) would be confusing at best and wrong at worst. This is because the background perturbation phasor is computed with an estimate of the background component of the target total field and not with the actual

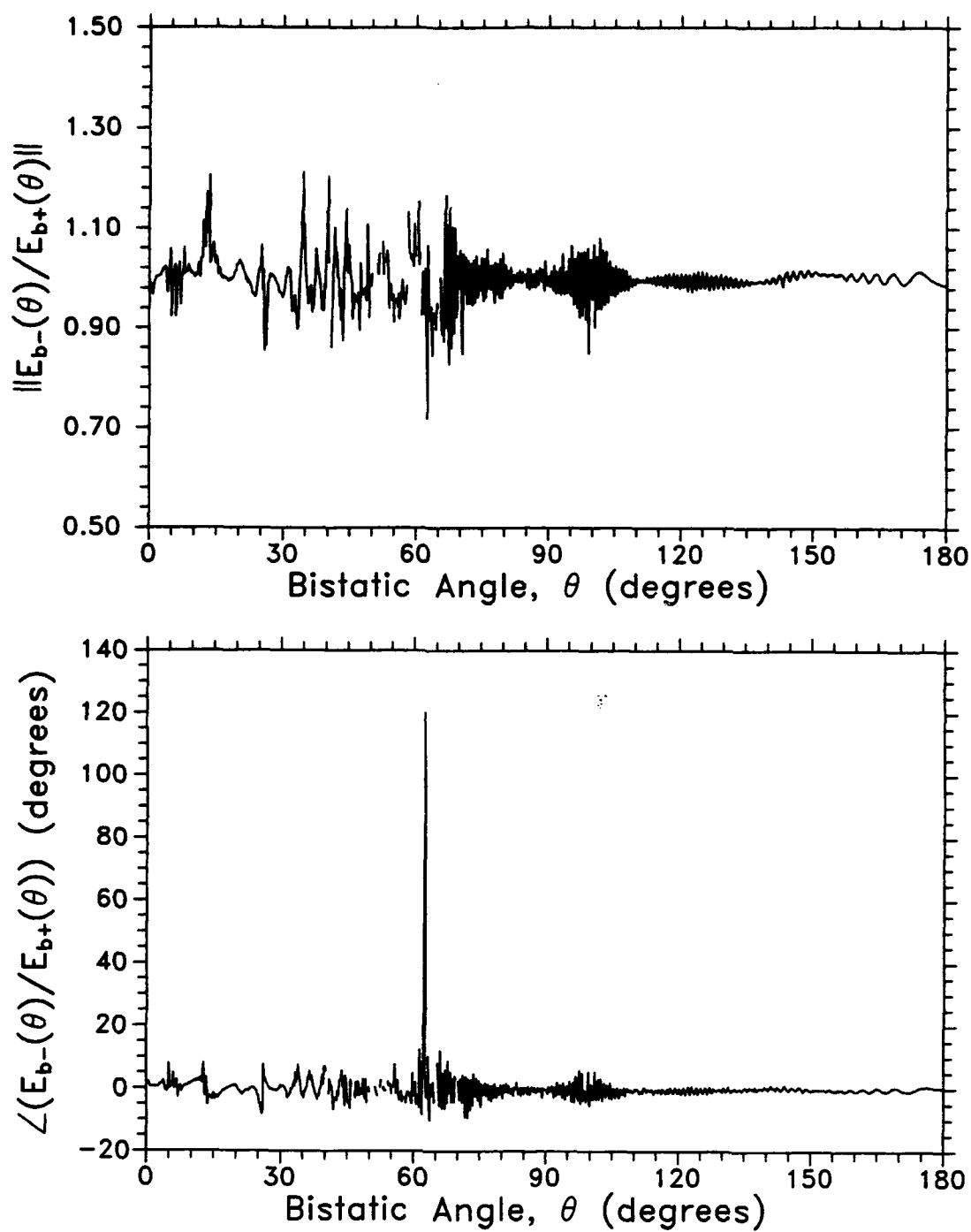


Figure 16: Background Perturbation Phasor Obtained by Computing the Ratio of Figures 11 and 13

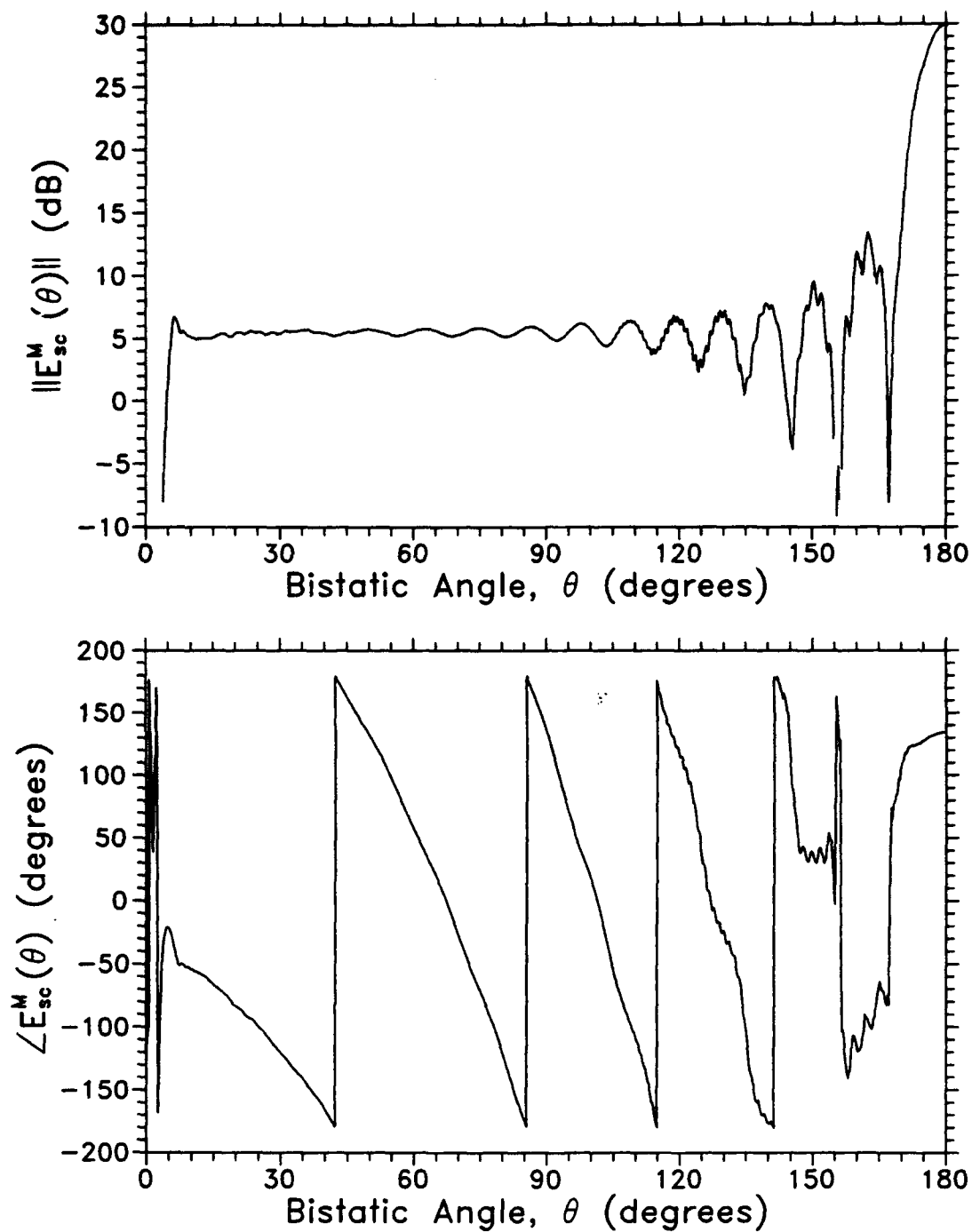


Figure 17: Measured Scattered Field of an Aluminum Sphere ($ka = 18$)

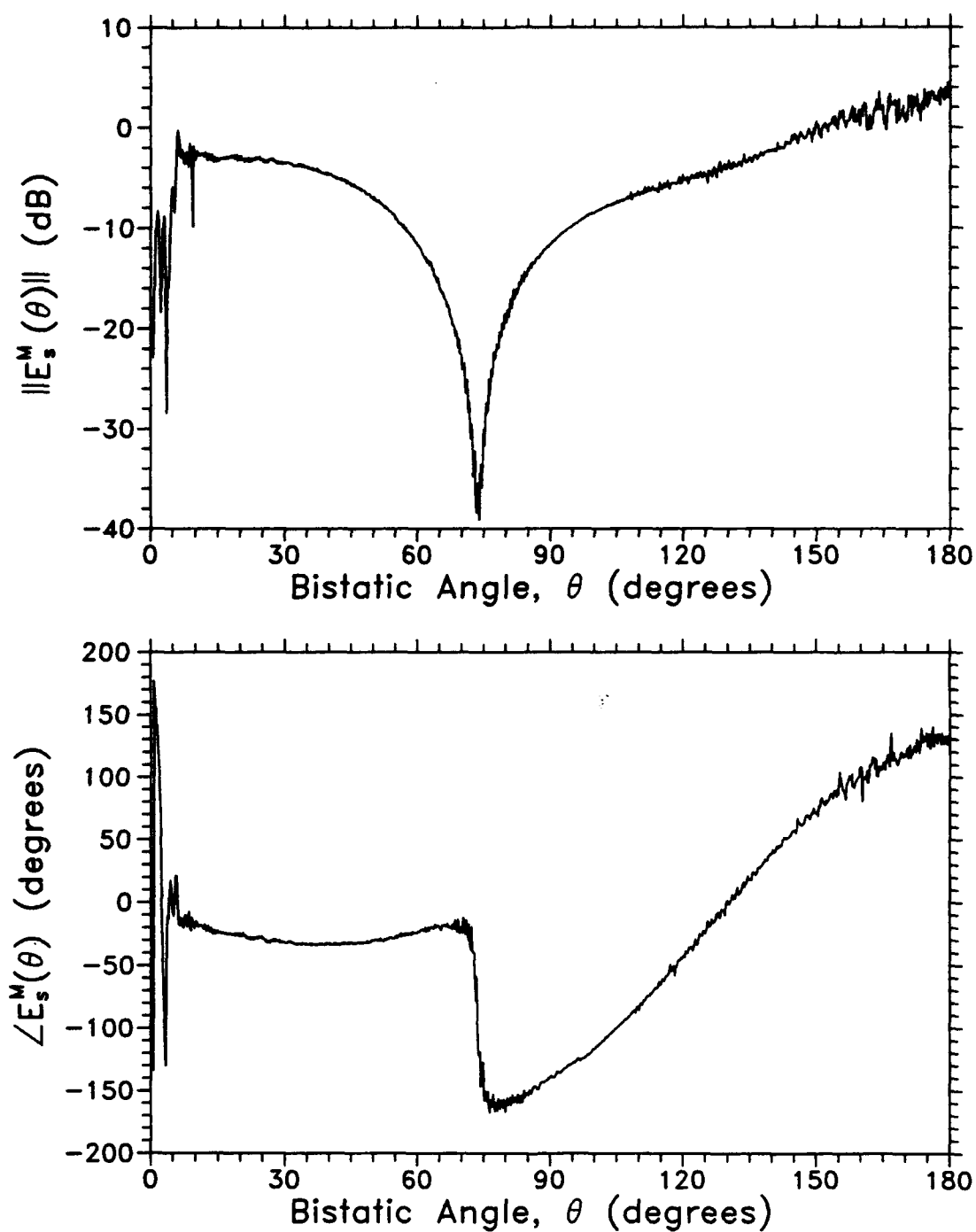


Figure 18: Measured Scattered Field of an Aluminum Cube ($s = 0.75\lambda$)

component. The modified version of Eq. (15) is given in Eq. (18).

$$U_m(\theta) = R_s(\theta) |1 - \epsilon_{RMS}(\theta)| \quad (18)$$

where,

$$R_s(\theta) = \frac{1}{\Delta\theta} \int_{\theta-\Delta\theta}^{\theta+\Delta\theta} |R(\theta)| d\theta. \quad (19)$$

Figure 19 shows the calibrated cube E-plane scattering with error bars plotted against a simulation for the scattering cross section of the cube computed by a dual-surface magnetic-field integral equation (DSMFIE) solution [8] [10]. The DSMFIE solution gives the phase of the scattered magnetic field referenced to the center of the cube's illuminated face. To compare the measured phase with the theory we plotted the magnetic field $[H_s^C(\theta)]$ phase referenced to the face of the cube, which we obtained from Eq. (20). The Δ in Eq. (20) is included to compensate for a misalignment of the cube center relative to the calibration sphere center. For this data $\Delta = 0.19$ cm.

$$\arg[H_s^C(\theta)] = \arg[E_s^C(\theta)] + 180^\circ + k \left(\frac{s}{2} + \Delta \right) [1 + \cos \theta] \quad (20)$$

The error bars were computed in accordance with Eq. (17) and Eq. (18) using smoothed background data and an RMS perturbation phasor. Figure 19 shows that the computed amplitude is within about 1 dB of the measured curve but does not completely lie within the error bars. We attribute this discrepancy to missing multipath errors in our error model. We have presented the example data for illustrative purposes. In a previous publication [8] we also compared the ASBSMS measurements to augmented and dual surface magnetic field integral equations applied to metal cubes as large as 5λ on a side. The measurements agreed very well with the integral equation solutions. For regions of very low scattering from the larger cubes, the phase errors [argument of $\epsilon(\theta)$ in Eq. (15)] were large enough to prevent an accurate determination of the scattered fields. To mitigate this problem we applied a spatial filtering technique that involved the size of the scatterer [5].

6 SUMMARY AND CONCLUSIONS

This report has described the automated swept-angle bistatic scattering measurement system of the Rome Laboratory Electromagnetics and Reliability Directorate. We set forth the measurement technique, and demonstrated that the technique is accurate for bistatic scattering from near backscatter through forward scatter. We presented the operating procedure, which provides for a data quality check as the measurements are collected. In addition, the procedure includes collecting data during each measurement session that gives a good estimate of the measurement error. We described the calibration technique and showed that this technique avoids the positioning problem for large bistatic angles common to the conventional fixed angle bistatic measurement systems. We showed that the calibration sphere's measured scattered field phase gives information about the sphere's position relative to the

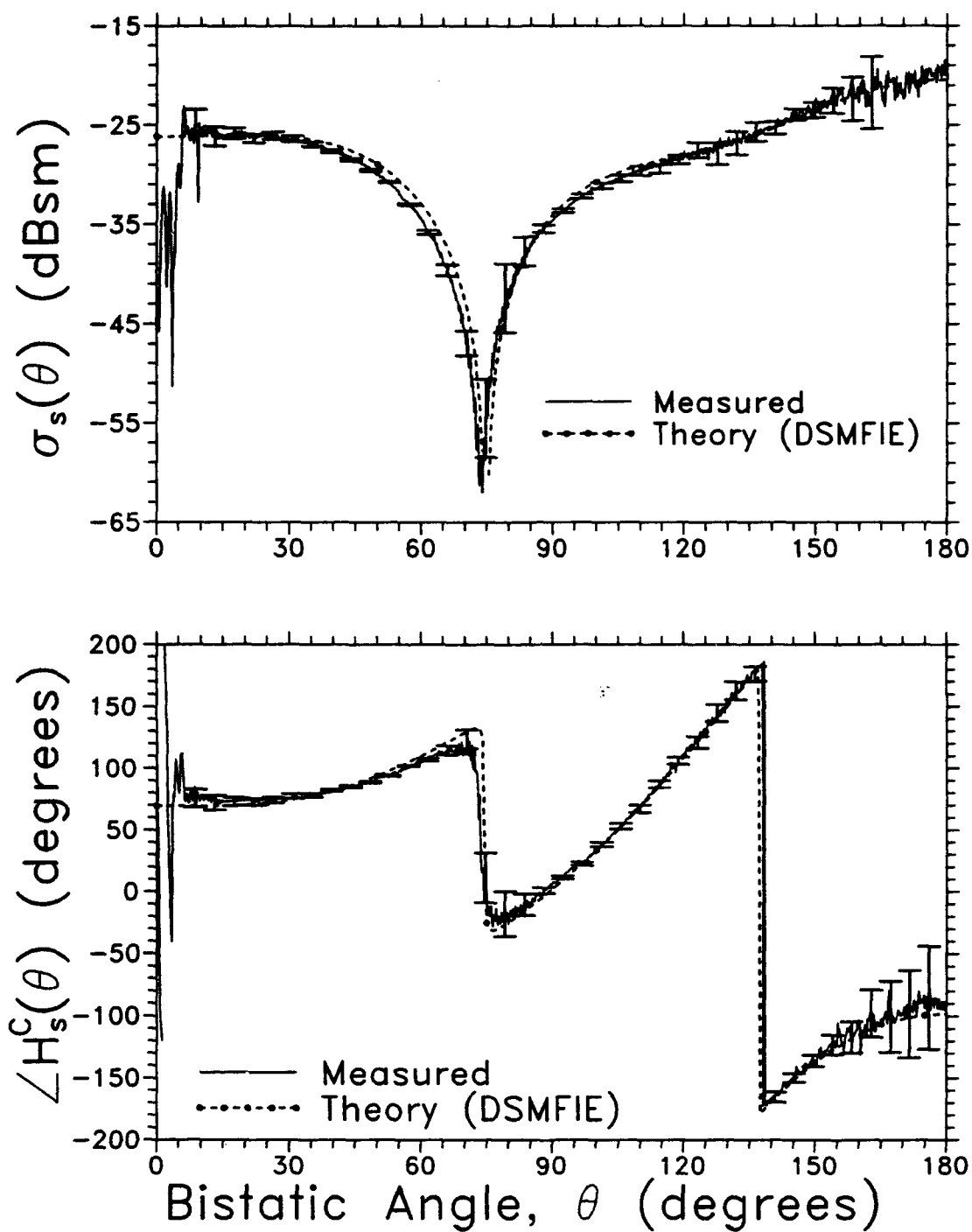


Figure 19: Calibrated Measured Scattering Cross Section of an Aluminum Cube ($s = 0.75\lambda$) with Error Bars, Compared to a Dual-Surface Magnetic-Field Integral Equation (DSMFIE) Solution

center of rotation of the measurement system. A method for correcting this phase error was given. Finally, we demonstrated the capability of the measurement system by examining the E-plane scattering from an aluminum cube with 0.75λ side length, for broadside incidence.

This automated measurement system is unique in its ability to automatically measure bistatic scattering from near backscatter through forward scatter. A first order error model that neglects multipath errors shows how the measurement accuracy varies with bistatic angle and depends on the target measured. Although multipath errors were reduced by a strategically placed absorber they were not eliminated. From our measurements and analysis we can expect improvement in both measurement accuracy and sensitivity in regions away from forward scatter by incorporating a time gating radar, and low sidelobe antennas such as diagonal horns.

References

- [1] McGahan, R. V. (1985) Bistatic scattering from metal cubes: theory and experiment, *URSI/APS Symposium Digest*, Vancouver, Canada.
- [2] McGahan, R. V. (1991) *Scattering experiments at the Ipswich electromagnetics measurements facility: swept angle bistatic measurement system*, RL-TR-91-114.
- [3] McGahan, R. V. (1985) *Scattering experiments at the Ipswich electromagnetic measurement facility: backscatter from metal cubes*, RADC-TR-85-24, ADA157925.
- [4] Scientific Atlanta (1984) Series 1780 Programmable Microwave Receiver Operators Manual, Publication No. 41RO45C.
- [5] Côté, M. G. (1989) *A spatial filtering technique for reducing phase errors in automated swept-angle bistatic scattering measurements*, RADC-TR-89-32, ADA225643.
- [6] Trott, K. D. (1988) *The Disk: A comparison of electromagnetic scattering solutions and its use as a calibration standard for bistatic RCS measurements*, RADC-TR-88-16:pp-19, ADA200327.
- [7] DiBeneditto, J. P. (1984) *Bistatic scattering from conducting calibration spheres*, RADC-TR-84-93, ADA154173.
- [8] Côté, M. G., Woodworth, M. B., and Yaghjian, A. D. (1988) Scattering from the perfectly conducting cube, *IEEE Trans. Antennas Propagat.*, AP-36: pp. 1321-1329.
- [9] Hewlett Packard (1987) *Basic Language Reference*, Part No. 98613-90052.
- [10] Woodworth, M. B., and Yaghjian, A. D. (1991) Derivation, Application and Conjugate Gradient Solution of Dual-Surface Integral Equations for Three-Dimensional, Multi-wavelength Perfect Conductors, *PIER 5, Application of Conjugate Gradient Method to Electromagnetics and Signal Analysis*, J. A. Kong and T. K. Sarkar, Ed., New York: Elsevier, Ch. 4.
- [11] Côté, M. G. (1991) *VAX-based software for processing scattering measurements collected with the RL/ERCT automated RCS measurement system*, RL-TM-91-3.
- [12] Knott, E. F., Shaeffer, J.F., and Tuley M.T. (1985) *Radar Cross Section*, Artech House.

- [13] Blacksmith, P. Jr., Hiatt, R. E., and Mack, R. B. (1965) Introduction to radar cross section measurements, *Proceedings of the IEEE*, **53**, No. 8.
- [14] Freeny, C. C. (1965) Target support parameters associated with radar reflectivity measurements, *Proceedings of the IEEE*, **53**, No. 8.
- [15] Kouyoumjian, R. G., and Peters, L. Jr. (1965) Range requirements in radar cross-section measurements, *Proceedings of the IEEE*, **53**, No. 8.
- [16] Dybdal, R. B. (1987) Radar cross section measurements, *Proceedings of the IEEE*, **75**, No. 4.
- [17] Hunka, J. F., Stovall, R. E., and Angelakos, D. J. (1977) A technique for the rapid measurement of bistatic radar cross section, *IEEE Transactions on Antennas and Propagation*, **AP-25**, No. 2.
- [18] Glaser, J. I. (1985) Bistatic RCS of complex objects near forward scatter, *IEEE Transactions on Aerospace and Electronics Systems*, **AES-21**, No. 1.
- [19] Walton, E. K., and Tubela-Reuning S. (1991) Compact range bistatic scattering measurements, *Proceedings Antenna Measurement Techniques Association Meeting*, Boulder, CO, pp 2.3-2.8.
- [20] Schmitt, K., Heidrich, E., and Wiesbeck, W., (1991) A new calibration technique for bistatic RCS measurements, *Proceedings Antenna Measurement Techniques Association Meeting*, Boulder, CO, pp 2.25-2.29.
- [21] Blanchard, A. J., Colquitt, W. N., Glazner, J. K., Jersak, B. D., Kreneck, B. D., Schindel, R. F., and Williams, B. A. (1991) A novel, bistatic, fully polarimetric radar cross-section measurement facility, *Proceedings Antenna Measurement Techniques Association Meeting*, Boulder, CO, pp 4.25-4.29.
- [22] Côté, M. G. (1992) Automated swept-angle bistatic scattering measurements using continuous wave radar, *IEEE Trans. Instrum. Meas.*, **41**: pp. 185-192.
- [23] Côté, M. G. (1992) An error model for automated swept-angle bistatic scattering measurements, *ANTEM Conference Proceedings*, Winnipeg, Canada, pp. 460-468.

Appendix A

DATA STRUCTURE

Raw measurement data are stored in one of several large database files residing on the system controller hard disc. These database files are named with the common filename and extension (*filename.extension*) convention. The filename identifies the particular measurement program for which the data are collected and the extension is always *DAT* indicating that the file contains raw measurements. The location of a particular measurement (referred to as a data block) within the database file is recorded in a separate file called a program file and has the same filename as the database file but has the extension *PRG*. As each measurement is written to the database file, its location (database file record number) and data block number are written in the program file. This allows fast (random) access of the data because searching for a particular data block requires checking a file (list) that is many times shorter (number of data blocks collected) than would otherwise be necessary (number of data points collected). When the measurement program is completed the database files and their associated program files are written to a cassette tape in Hewlett Packard Basic (BDAT) format. These tapes are kept indefinitely. Normally during a measurement program data are periodically transferred to the ERCT VAX via a Kennedy tape drive based data transfer system. The data arrives on the VAX in a large ASCII formatted data file. The filenames for these files (on the VAX the file name format is *filename.extension* instead of *filename_extension*, as on the Hewlett Packard 9836 running HP-Basic 3.0) are formed by concatenating the database file filename with a number equal to one plus the number of data transfers that have taken place for the particular measurement program. These files have extensions *KDY* to indicate that the data are in a Kennedy tape drive format and must be translated before processing with the VAX based RCS data processor ⁷. These Kennedy files usually contain several data blocks (measurements) and each data block is broken out into a separate ASCII data file via a Fortran V program (KTOV02.FOR). The files are named according to the following convention. The filename is made up of a prefix concatenated with a suffix and the file extension is *RAWD*, to indicate that the raw measurement data

⁷The VAX-11/750 based RCS data processor (RCS DPP) is a Fortran V program that performs several data manipulations that are useful for understanding scattering data, including phasor background subtraction.

may be used by the RCS data processor. The prefix is the same as that used to describe the database file from which the measurement data were extracted and the suffix is a three digit number equal to the data block number. There are two data format structures used by the measurement system: one for the database file data, and the other for the VAX based RCS data processor.

The database file format was designed to accommodate all the information required to reconstruct the pertinent measurement parameters and instrument settings used for the particular measurement. The data are arranged in blocks that are 48 bytes wide (each byte is 8 bits) and $21 + N_{pts}$ (N_{pts} = number of measurement points) records long. The records are 48 bytes long because Hewlett Packard Basic (Bdat) data format requires 8 bytes to represent a real number and 6 numbers are required to represent each measurement point. Figure A.1 shows the data structure for the n th data block. Each data block begins with a record that contains 6 real numbers. The first number, 11111, identifies the beginning of the data block. The second number gives the data block number (dblkno). The remaining 4 numbers are set to 11111 and may be used in the future to store desired information. The next 9 records contain a 428 character alphanumeric string⁸ that contains encoded measurement parameters. Table A.1 defines the codes. Next are nine records containing a 428 character encoded alphanumeric string that describes the receiver setup. This string is stored such that it can be written directly to the receiver to establish the given receiver settings. For a complete description of the receiver setup code refer to the SA Model 1785 programmable Microwave Receiver Operators manual [4]. The next record ($n+19$) contains six real numbers that represent the following (refer to Figure A.1):

- t_o - is the time the measurement run began in HP-basic internal time format [9].
- t_p - is the measurement end time.
- Refmin - is the minimum reference power level in dB encountered during the scan.
- Refmax - is the maximum reference power level encountered during the measurement.
- N - is the number of measurement points collected during the scan.
- 88888.0 - is a dummy value to reserve the space for future use.

The remaining N records contain the measured data - six real number values per record, one record per measured point. Each real number column represents the following:

- Column 1 - the bistatic angle in degrees, θ_n .
- Column 2 - the relative power of the total field in dB, $|E_n|^2$.
- Column 3 - the relative phase of the total field in degrees, $\angle E_n$.
- Column 4 - the IF attenuation of the signal channel in dB, IFA_n^{Sig} .
- Column 5 - the IF attenuation of the reference channel in dB, IFB_n^{Ref} .
- Column 6 - the relative power of the reference signal, $|E_n^{Ref}|^2$.

⁸Note; $9 \times 48 = 432$. The 4 extra bytes are prescribed by the Bdat format and are used to indicate the length of the stored string.

Record	Contents					
	1	2	3	4	5	6
n-1	99999.	99999.	99999.	99999.	99999.	99999.
n	11111.	dblkno	11111.	11111.	11111.	11111.
n+1 to n+9	<p>Encoded alphanumeric string describing the measurement parameters. The format of the string follows:</p> <p style="text-align: center;"><i>code:value,</i></p> <p>where <i>code</i> is a variable length alphanumeric string describing the measurement parameter, <i>:</i> is used to separate the <i>code</i> from its value, <i>value</i> is a variable length alpha numeric string containing the value of the parameter, and <i>,</i> is used to separate adjacent parameters.</p>					
n+10 to n+18	<p>Encoded alphanumeric string describing the receiver (SA-1785) set up parameters. the encoded string is in a form that can be sent directly to the receiver after stripping off the trailing # (the # are used to completely fill the records allotted which allows random access of the data). The meaning of the code can be found in the operators manual [4]. the code format follows.</p> <p style="text-align: center;"><i>codevalue,</i></p> <p>where <i>code</i> is a variable length alpha string, <i>value</i> is a variable length numeric string, and <i>,</i> is used to separate adjacent parameters.</p>					
n+19	t_o	t_f	Ref _{min}	Refmax	N	88888.
n+20	θ_1	$ E_1 ^2$ dB	$\angle E_1$ deg	IFA ₁ ^{Sig} dB	IFA ₁ ^{Ref} dB	$ E_1^{Ref} ^2$ dB
↓	↓	↓	↓	↓	↓	↓
n + N +20	θ_N	$ E_N ^2$ dB	$\angle E_N$ deg	IFA _N ^{Sig} dB	IFA _N ^{Ref} dB	$ E_N^{Ref} ^2$ dB
n + N + 20 + 1	99999.	99999.	99999.	99999.	99999.	99999.
↓	↓	↓	↓	↓	↓	↓

Figure A.1: Data Base File Structure on the ASBSMS System Disc. The data are in Hewlett Packard Basic (BDAT) format.

Table A.1: Description of Mnemonics Used to Encode the Measurement and Receiver Parameters. The measurement parameters are used by the RCS data processor when translating measured data from ASBSMS system disc format to VAX-based format.

CODE	DESCRIPTION	CODE	DESCRIPTION
A1	Aspect positioner start angle	LP	Phase display mode (0 - 360 / ± 180)
A2	Aspect positioner stop angle	LR	LRCS return angle
A3	Aspect positioner stepping an	LS	LRCS speed
AA	Channel A Amplitude mode	LW	LRCS window (accuracy)
AB	Channel B Amplitude mode	M	Recall front panel setup number
AC	Channel C Amplitude mode	MOD	SA-2150 modulation
AO	Aspect positioner zero reference	NA	Channel A IF attenuation
AR	Aspect positioner return angle	NB	Channel B IF attenuation
AS	Aspect positioner speed	NC	Channel C IF attenuation
AW	Aspect positioner window	NCOL	Number of data columns
B	Frequency band select	O	Select recorder output data
B1	Bistatic boom start angle	O2	Date of measurement
B2	Bistatic boom stop angle	PA	Channel A phase mode select
B3	Bistatic boom step angle	PB	Channel B phase mode select
BF	SA-2150 Frequency (start)	PR	Receive probe radius (cm)
C1	Column 1 data	PS	Bistatic boom speed
C2	Column 2 data	PT	Target Pitch
C3	Column 3 data	PTS	Number of data points (rows)
C4	Column 4 data	Q	Select APC control 0=off/1=on
C5	Column 5 data	R	Select frequency reset
C6	Column 6 data	RL	Target Roll
C7	Column 7 data	RP	Receive polarisation
C8	Column 8 data	S	Select search width in MHz
C10	Column 9 data	SF	SA-2150 frequency (step)
CAP	Select preset mixer current (APC)	SP	SA-2150 sweep off/sweep1/sweep2
CAS	Enter stored mixer current (APC)	T	Select frequency tuning mode
CD	Target critical dimension	TE	Time measurement was completed
CS	Number of computer samples/point	TG	Target name
CSP	Select preset mixer current (SIG)	TM	Type of measurement (Monostatic)
CSS	Enter stored mixer current (SIG)	TP	Transmit polarisation
DIR	Directory where stored	TS	Time measurement started
DV	Disc drive where this stored	U	IF Reference off=0/on=1
EA	Measurement average sample select	V	IF mode select
EB	Measurement bandwidth select	W	Receiver output format
EF	SA02150 frequency (stop)	WW	Bistatic boom window (accuracy)
F	Enter frequency in GHz	X2	Not used
FT	Time measurement was taken	X3	Not used
G8765	Parallel poll configuration	X4	Not used
H	Store front panel setup no.	X5	Not used
IC	Initiate IF calibration	X6	Not used
JAP	Channel A amplitude present	X7	Not used
JAR	Clear Ch. A amp present	X8	Not used
JBP	Channel B amplitude present	X9	Not used
JBR	Clear Ch. B amp present	XA	Recall Attenuation command
JCP	Channel C amplitude present	XH	High speed mode
JCR	Clear Ch. C amp present	XL	Low speed mode
KAP	Channel A phase preset	XO	Number of manual entries
KAR	Clear Ch. A phase present	XR	Reset command
KBP	Channel B phase preset	YW	Target yaw
KBR	Clear Ch. B phase present	ZAA	Zero Ch. A amplitude display
L1	LRCS start position	ZAB	Zero Ch. B amplitude display
L2	LRCS stop position	ZAC	Zero Ch. C amplitude display
L3	LRCS step	ZO	Bistatic boom zero reference
LA	Amplitude Display mode (log/lin)	ZPA	Zero Ch. A phase display
LFN	Last file name	ZPB	Zero Ch. B phase display
LO	LRCS zero reference		

Table A.2: System Disc Plotting Code Used by the ASBSMS when Plotting Data at the Measurement Site

CODE	DESCRIPTION
DN	Data block number
SL	Axis scale
TG	Target description
T1	First line of the plot title
T2	Second line of the plot title
T3	Third line of the plot title
X0	Lower limit of plotting range
XF	Upper limit of plotting range
XL	X-axis title
XN	X-axis lower limit label
XX	X-axis upper limit label
YL	Y-axis title
YN	Y-axis lower limit label
YX	Y-axis upper limit label

The last record of each data block contains 6 real numbers each set to 99999.0. This is used to mark the end of the data block.

The data structure of the program file is given in Figure A.2. This file (*PRG*) is used to index the data blocks contained within the data base file (*DAT*). This Bdat file is made up of 404 byte records. The first 10 records contain ASCII strings which describes the particular measurement program at hand. Records 11 through 14 contain default information used by the system controlling software. These records contain the following:

- Record 11 - encoded ASCII string describing measurement parameters used for the last measurement run made. (Refer to Table A.1 for codes)
- Record 12 - encoded ASCII string describing the receiver set up used for the last measurement. (Refer to receiver operator's manual [4] for codes.)
- Record 13 - two entries - first is the number assigned to the last data block. This entry has the format < 0092 >, where the 0092 is a 4 character string indicating that the last measurement data is contained within data block 92. Second is a 10 character ASCII string containing the name of the data base file. For example, CUBE01.DAT.
- Record 14 - encoded ASCII string containing plotting parameters for last data file plotted. (See Table A.2)

The remaining records (15 and greater) are organized in 2 record blocks, each set containing

Record	Contents
1 through 10	ASCII string containing descriptive information about the particular measurement program.
11	Encoded default measurement parameters.
12	<???? >, <i>datafile</i> Where ???? = data block number of the last measurement, and <i>datafile</i> is the name of the Bdat database file containing the measured data.
13	Encoded default receiver setup string.
14	Encoded default plotter settings.
Records 15 and below, index particular measurements. The required information is contained in two record sets. The first record gives the data block number and the data file record number where the measured data are located.	
15	data block number 1, <i>datafile</i> record number.
16	Encoded measurement parameters for data block 1.
17	data block number 2, <i>datafile</i> record number.
18	Encoded measurement parameters for data block 2.
↓	↓
$2 \times N_{\text{dat}}$	data block number N_{dat} , <i>datafile</i> record number.
$2 \times N_{\text{dat}} + 1$	Encoded measurement parameters for data block N_{dat} .

Figure A.2: Data Base Index-File Structure on the ASBSMS System Disc. Note that N_{dat} is the number of data points contained in the given data set.

information about the measurements that are stored in the data base file. The first record of the set has two real number entries, a data block number, and data base file record number where the data block containing the particular measurement begins. The second record contains the encoded measurement parameter string. Figures A.3 and 6 present example program (SASX_PRG) and database (SASX_DAT) files, respectively.

The VAX-based data structure was designed to be more general than the HP data structure, which was set up exclusively for swept angle bistatic scattering data. The VAX-based data must contain information about the data processing, in addition to information about the conditions under which the raw measurements were made. All data files generated by the VAX RCS data processor contain information to link the processed data to the raw measurements. The VAX data structure is illustrated in Figure A.4. Records 1 through 11 comprise the header. Records 12 through $12 + NPTS + 1$ contain the measured (or processed) data, each record characterizing a single data point with six real numbers. Record 11 of the headers is a 78 character ASCII string describing what each of the six column entries contain. For raw measurements arriving from Ipswich the six column entries are:

- Column 1 - Bistatic angle degrees.
- Column 2 - Relative total field proportional to volts.
- Column 3 - Relative phase of the total field in degrees.
- Column 4 - Signal channel IF attenuator setting in dB.
- Column 5 - Reference channel IF attenuator setting in dB.
- Column 6 - Relative reference signal level proportional to volts.

These data files have .RAWD extensions. Data files containing processed data will have extensions indicative of the particular processing. For example .SUBT files contain scattered field data because they result from performing the phasor subtraction of a total field data set (.RAWD) and a background field data set (.RAWD). A complete description of the data processing software (RCS DPP) and the resulting data are described in Rome Laboratory Tech-memo RLTM-91-3 [11]. The last record in each VAX based data file contains the value 99999.0 in each of the six columns. This last line is used by the RCS data processor and indicates the end of file. The header records describe the conditions under which the data was collected. A description of the parameters comprising the header is given in Table A.3 indicating which parameters are associated with the raw measurements and which are used for processing. Table A.3 should be read in conjunction with Figure A.4, which gives the position of each parameter within the header. Figures A.5 and A.6 give examples of VAX-based raw (.RAWD) measurement data files. Figure A.5 is the total field of a square aluminum flat plate with side length 5.0λ . Figure A.6 is the background field associated with the cube total field. The flat plate measurement was a cut in the $\phi = 45^\circ$ plane⁹ with horizontal transmit and receive polarization at 10 GHz. This data was collected on 22 March 1990 and was translated to the VAX-based RCS DPP data structure on 26 March 1990.

As an example of a processed data file we include the phasor subtraction of the data files given in Figures A.5 and A.6, shown in Figure A.7.

⁹Refer to Figure 4 and to Appendix B for a complete description of the measurement geometry.

PROGRAM FILE: SASX_PRG

..[Record Length - 404 bytes] || Record

The purpose of this project is to obtain bistatic RCS data on
general ... 0001

↓

↓

TM:2,TG:BACKGROUND,CD:000000,PT:00000,RL:00000,YW:00000,TP:H,RP:H,CS:01,B...	0011
AA1,AB1,LA1,PA1,EA05,EB7,NA20,NB40,T1,CSS4.20,CAS4.20,F10.00,S050,B5;	0012
<0443>,SASX_DAT	0013
DN:0441,TG:AMPLITUDE ,T1:X_BAND F=10.00 GHz ,T2: ...	0014
326 1	0015
TM:2,TG:BACKGROUND,CD:000000,PT:00000,RL:00000,YW:00000,TP:H,RP:H,CS:01,B...	0016
327 383	0017
TM:2,TG:BACKGROUND,CD:000000,PT:00000,RL:00000,YW:00000,TP:H,RP:H,CS:01,B...	0018

↓

↓

Figure A.3: Example System Disc Index-File (*SASX_PRG*)

DATABASE FILE: SASX_DAT	..[Record Length - 48 bytes]	Record
-------------------------	------------------------------	--------

11111	326	11111	11111	0	0	0001
TM:2,TG:BACKGROUND,CD:000000,PT:00000,RL:00000,Y						0002
AW:00000,TP:H,RP:H,CS:01,BA:000000,EA:018000,SA:						0003
000050,WW:00010,BF:10000,EF:10000,SF:00000,Z0:02						0004
293,PR:28245,RS:1,PS:-07;#####						0005
#####						0006
#####						0007
#####						0008
#####						0009
#####						0010
AA1,AB1,LA1,PA1,EA05,EB7,NA20,NB40,T1,CSS4.20,CA						0011
S4.20,F10.00,S050,B5,W0,V1,00,Q1,PB0,LP2,AC0,G87						0012
65,XH;#####						0013
#####						0014
#####						0015
#####						0016
#####						0017
#####						0018
#####						0019
28 Feb 1990 08:25:53 28 Feb 1990 08:38:43						0020
2.11E+11	769.84002	-31.69	-31.68	361	88888	0021
0	-63.62	-175.7	20	40	-31.69	0022
.5	-44.30	-118.8	20	40	-31.69	0023
↓						↓
TT180	-3.89	178.4	20	40	-31.69	0381
99999	99999	99999	99999	99999	99999	0382
11111	327	11111	11111	0	0	0383
TM:2,TG:BACKGROUND,CD:000000,PT:00000,RL:00000,Y						0384
AW:00000,TP:H,RP:H,CS:01,BA:000000,EA:018000,SA:						0385
000050,WW:00010,BF:10000,EF:10000,SF:00000,Z0:02						0386
293,PR:28245,RS:1,PS:-07;#####						0387
#####						0388
#####						0389
#####						0390
#####						0391
#####						0392
AA1,AB1,LA1,PA1,EA05,EB7,NA20,NB40,T1,CSS4.20,CA						0393
↓						↓

Figure A.4: Example System Disc Data Base File (SASX_DAT)

Table A.3: Description of Mnemonics Used in Figure 3.4 to Describe the Measurement Parameters. This table can be used by customers to decode the header information contained in each measurement data file.

CODE	TYPE	UNITS	DESCRIPTION
DBNO	REAL	N/A	Data block number
DBPN	REAL	N/A	Data block number of data file required in addition to DBNO file in given data process.
TPRCS	CHAR*12	N/A	Type of data process that generated the data file.
DTBS	CHAR*12	N/A	Measurement project code name.
MTYPE	CHAR*78	N/A	Measurement configuration. (Fixed angle Bistatic, Monostatic, etc.).
TARGET	CHAR*78	N/A	Target description
PITCH	REAL	Degrees	Pitch angle of target fixed coordinates.
ROLL	REAL	Degrees	Roll angle of target fixed coordinates.
YAW	REAL	Degrees	Yaw angle of target fixed coordinates.
ACCF	REAL	meters/ $\sqrt{\text{watts}}$	Amplitude of the complex calibration factor computed on the observation sector bounded by ATHTO and ATHTF.
PCCFT	REAL	Degrees	Phase of the complex calibration factor computed on the observation sector bounded by ATHTO and ATHTF.
CFT	REAL	meters/ $\sqrt{\text{watts}}$	Calibration factor computed from magnitude data only.
RXPOL	REAL	Degrees	Polarization of receive probe measured from vertical. 0 = Vertical, 90 = Horizontal.
TXPOL	REAL	Degrees	Polarization of transmit antenna measured from vertical. 0 = Vertical, 90 = Horizontal.
FRQ0	REAL	GHz	Start frequency.
FRQF	REAL	GHz	Stop frequency.
DFRQ	REAL	GHz	Step frequency.
TDIM	REAL	Centimeters	Significant target dimension. Usually the radius of the target minimum circumscribing sphere.
THT0	REAL	Degrees	Start bistatic angle.
THTF	REAL	Degrees	End bistatic angle.
DTHT	REAL	Degrees	Step bistatic angle.
PHI0	REAL	Degrees	Start aspect angle.
PHIF	REAL	Degrees	End aspect angle.
DPHI	REAL	Degrees	Step aspect angle.
KAT	REAL	N/A	Electrical radius of the target minimum circumscribing sphere.
MUSD	REAL	N/A	Number of modes used in spatial filtering of the data.
ATHT0	REAL	Degrees	Start angle of observation sector over which average calibration factor was computed.
ATHTF	REAL	Degrees	End angle of observation sector over which average calibration factor was computed.
THTOFF	REAL	Degrees	Offset angle used during data calibration.
RPRNG	REAL	Centimeters	Receiving probe range.
HDTOM	CHAR*21	N/A	DATA COLLECTION DATE:
TDM	CHAR*18	N/A	Time that raw data was collected.
HDTFC	CHAR*21	N/A	FILE CREATION DATE:
TFC	CHAR*18	N/A	Time that data file was created.
SIGMIN	REAL	See DLABEL	Signal minimum of data in column 2. Units are the same as given in DLABEL.
SIGMAX	REAL	See DLABEL	Signal maximum of data in column 2. Units are the same as given in DLABEL.
REFMN	REAL	Volts (relative)	Value of minimum reference signal recorded during measurement.
REFMX	REAL	Volts (relative)	Value of maximum reference signal recorded during measurement.
NPTS	REAL	N/A	Number of data points contained in the data file. Number of rows between DLABEL and 99999. rows.
DTIME	REAL	Minutes	Time separation between target and background total field measurements.
RDUM	REAL	N/A	Dummy real number reserved for future use.
CD12	CHAR*12	N/A	Dummy character string reserved for future use.
DLABEL	CHAR*78	N/A	Labels the units and kind of data contained in each column of the data file. Data follows this line.
VAR	REAL	See DLABEL	Measurement variable. THT (bistatic angle), or PHI (aspect angle), or FRQ (frequency). See measurement type (MTYPE).
MET	REAL	See DLABEL	Determined from TPRCS but usually the magnitude of signal of interest.
PET	REAL	See DLABEL	Determined from TPRCS but usually the phase of signal of interest.
RET	REAL	See DLABEL	Determined from TPRCS but usually real part of the signal of interest.
IET	REAL	See DLABEL	Determined from TPRCS but usually the imaginary part of the signal of interest.
REF	REAL	See DLABEL	Determined from TPRCS but usually the reference signal level in $\sqrt{\text{watts}}$ (volts relative).
11111	REAL	N/A	Signals beginning of data.
99999	REAL	N/A	Signals end of data.

Record	Format	Contents					
		1	2	3	4	5	6
1	1001	11111.	DBNO	DBPN	RDUM	TPRCS	DTBS
2	1002	MTYPE					
3	1002	TARGET					
4	1004	PITCH	ROLL	YAW	ACCFT	PCCFT	CFT
5	1004	RXPOL	TXPOL	FRQ0	FRQF	DFRQ	TDIM
6	1004	THT0	THTF	DTHT	PHI0	PHIF	DPHI
7	1004	KAT	MUSD	ATHT0	ATHTF	THTOFF	RPRNG
8	1006	CD12	RDUM	RDUM	CD12	RDUM	RDUM
9	1005	HDTOM		TDM	HDTFC		TFC
10	1004	SIGMIN	SIGMAX	REFMN	REFMX	NPTS	DTIME
11	1002	DLABEL					
12	1004	VAR^1	MET^1	PET^1	RET^1	IET^1	REF^1
↓	↓	↓	↓	↓	↓	↓	↓
NPTS+11	1007	VAR^m	MET^m	PET^m	RET^m	IET^m	REF^m
NPTS+12	1007	99999.	99999.	99999.	99999.	99999.	99999.

Format No.	Fortran V Format
1001	[4(F12.6,1X),2(A12,1X)]
1002	[A78]
1004	[6(F12.6,1X)]
1005	[2(A21,A18)]
1006	[2(A12,F12.6,1X)]
1007	[6(E12.5,1X)]

Figure A.5: VAX-Based Data File Structure Required by the RCS Data Processor (RCSDPP) which Runs the RL/ERCT VAX 11750. This data structure is used when data are delivered to customers. Note that subscript m indicates the number of measured points ($m = \text{NPTS}$).

11111.000000	393.000000	0.000000	0.000000	RAW DATA	SASX04
BISTATIC WITH FIXED TRANSMITTER					
PLATE5FLAT					
0.000000	45.000000	45.000000	999.000000	2.000000	999.000000
90.000000	90.000000	10.000000	0.000000	0.000000	10.599000
0.000000	185.000000	0.500000	0.000000	0.000000	0.000000
22.210000	22222.000000	22222.000000	22222.000000	22222.000000	282.450000
N/Applicable	22222.000000	22222.000000	N/Applicable	22222.000000	22222.000000
DATA COLLECTION DATE:22 Mar 90 09:23:20 FILE CREATION DATE:26-MAR-90 16:51:08					
0.20869E-01	6.08135E+01	7.345139	7.353600	371.000000	88888.000000
ANGLE deg #	E v/m #	ARG(E) deg #	RE(E) #	IM(E) #	REF FD v/m #
0.000000	0.039446	-54.400002	0.022962	-0.032073	7.353600
0.500000	0.037068	66.000000	0.015077	0.033863	7.353600
1.000000	0.050292	85.900002	0.003596	0.050163	7.353600
1.500000	0.020869	-177.100006	-0.020842	-0.001056	7.353600
2.000000	0.078524	-144.300003	-0.063768	-0.045822	7.353600
2.500000	0.071040	-141.900009	-0.055903	-0.043834	7.353600
3.000000	0.073114	-70.000000	0.025006	-0.068705	7.353600
3.500000	0.157398	-59.100002	0.080830	-0.135058	7.353600
4.000000	0.213059	-71.599998	0.067252	-0.202167	7.353600
↓	↓	↓	↓	↓	↓
178.500000	5.565446	6.800000	5.526296	0.658971	7.345139
179.000000	5.774309	7.500000	5.724909	0.753699	7.345139
179.500000	5.991009	12.000000	5.860091	1.245601	7.345139
180.000000	6.011737	17.500000	5.733496	1.807764	7.345139
180.500000	5.649370	22.200001	5.230585	2.134562	7.345139
181.000000	5.260173	25.900000	4.731829	2.297653	7.345139
181.500000	5.188000	31.100000	4.442314	2.679775	7.345139
182.000000	5.432503	39.799999	4.173703	3.477398	7.345139
182.500000	5.591135	52.700001	3.388163	4.447600	7.345139
183.000000	5.489086	69.800003	1.895371	5.151469	7.345139
183.500000	5.182031	89.599998	0.036177	5.181905	7.345139
184.000000	5.040806	111.599998	-1.855644	4.686823	7.345139
184.500000	5.420009	132.400009	-3.654726	4.002434	7.345139
185.000000	6.081350	149.800003	-5.255958	3.059040	7.345139
99999.000000	99999.000000	99999.000000	99999.000000	99999.000000	99999.000000

Figure A.6: Example of a VAX-Based Total-Field Data File (File Name SASX040393.RAWD) Showing Total-Field Measurement Data for an E-plane Cut of a Square Plate at 10 GHz

```

11111.000000  395.000000  0.000000  0.000000  RAW DATA  SASX04
BISTATIC WITH FIXED TRANSMITTER
BACKGROUND
  0.000000  0.000000  0.000000  999.000000  2.000000  999.000000
 90.000000  90.000000  10.000000  0.000000  0.000000  0.000000
  0.000000  185.000000  0.500000  0.000000  0.000000  0.000000
  0.000000  22222.000000  22222.000000  22222.000000  22222.000000  282.450000
N/Applicable 22222.000000 22222.000000 N/Applicable 22222.000000 22222.000000
DATA COLLECTION DATE:22 Mar 90 10:19:55 FILE CREATION DATE:26-MAR-90 16:51:28
0.20749E-01 0.72110E+01 7.336686 7.345139 371.000000 88888.000000
ANGLE deg # |E| v/m # ARG(E) deg # RE(E) # IM(E) # REF FD v/m #
  0.000000  0.037325 -56.000000  0.020872 -0.030944 7.336686
  0.500000  0.036644  65.300003  0.015312  0.033291 7.345139
  1.000000  0.051050  85.000000  0.004449  0.050856 7.336686
  1.500000  0.020749 173.300003 -0.020607  0.002421 7.336686
  2.000000  0.076208 -148.000000 -0.064628 -0.040384 7.345139
  2.500000  0.068391 -146.600006 -0.057096 -0.037648 7.345139
  3.000000  0.064047 -69.099998  0.022848 -0.059833 7.345139
  3.500000  0.147401 -57.099998  0.080064 -0.123761 7.345139
  4.000000  0.203939 -69.900002  0.070086 -0.191518 7.336686

↓           ↓           ↓           ↓           ↓           ↓
178.500000  6.637431  17.600000  6.326737  2.006959 7.336686
179.000000  6.846995  18.000000  6.511879  2.115838 7.336686
179.500000  7.120328  21.600000  6.620314  2.621168 7.336686
180.000000  7.211075  26.200001  6.470197  3.183732 7.336686
180.500000  6.894456  30.700001  5.928214  3.519916 7.345139
181.000000  6.546362  34.400002  5.401491  3.698479 7.336686
181.500000  6.508786  38.400002  5.100893  4.042918 7.336686
182.000000  6.799860  45.299999  4.782986  4.833337 7.345139
182.500000  6.998420  55.799999  3.933696  5.788257 7.345139
183.000000  6.870684  69.400002  2.417393  6.431370 7.336686
183.500000  6.426877  85.500000  0.504247  6.407065 7.336686
184.000000  6.032537 103.599998 -1.418503  5.863391 7.336686
184.500000  6.046444 122.500000 -3.248752  5.099519 7.336686
185.000000  6.360628 139.900009 -4.865381  4.097030 7.345139
99999.000000 99999.000000 99999.000000 99999.000000 99999.000000 99999.000000

```

Figure A.7: Example of a VAX-Based Background-Field Data File (File Name *SASX040395.RAWD*) Showing E-plane Background-Field Measurement Data at 10 GHz

```

11111.000000  393.000000  395.000000  88888.000000  SUBTRACT          SASX04
BISTATIC WITH FIXED TRANSMITTER
PLATE5FLAT
  0.000000    45.000000    45.000000    999.000000    2.000000    999.000000
 90.000000    90.000000    10.000000     0.000000     0.000000    10.590000
  0.000000   185.000000     0.500000     0.000000     0.000000     0.000000
  0.000000   766.421692  22222.000000  22222.000000  22222.000000    282.450000
N/Applicable 22222.000000 22222.000000 N/Applicable 22222.000000 22222.000000
DATA COLLECTION DATE:22 Mar 90 09:23:20 FILE CREATION DATE:26-MAR-90 16:58:40
0.61800E-03  0.15731E+01    7.345139    7.353600   371.000000  88888.000000
ANGLE deg # |E| v/m # ARG(E) deg # RE(E) v/m # IM(E) v/m # dummy #
  0.000000    0.002376   -28.387100    0.002091   -0.001130  22222.000000
  0.500000    0.000618   112.372131   -0.000235    0.000572  22222.000000
  1.000000    0.001099  -140.949265   -0.000854   -0.000692  22222.000000
  1.500000    0.003485   -93.866539   -0.000235   -0.003477  22222.000000
  2.000000    0.005505   -81.013161    0.000860   -0.005438  22222.000000
  2.500000    0.006300   -79.091751    0.001192   -0.006186  22222.000000
  3.000000    0.009130   -76.325760    0.002158   -0.008872  22222.000000
  3.500000    0.01133    -86.121445    0.000766   -0.011297  22222.000000
  4.000000    0.011019  -104.901840   -0.002834   -0.010649  22222.000000

↓           ↓           ↓           ↓           ↓           ↓

178.500000    1.567731  -120.702034   -0.800442   -1.347989  22222.000000
179.000000    1.573132  -120.016991   -0.786970   -1.362139  22222.000000
179.500000    1.571662  -118.927711   -0.760222   -1.375567  22222.000000
180.000000    1.560775  -118.164864   -0.736701   -1.375968  22222.000000
180.500000    1.551092  -116.728645   -0.697628   -1.385353  22222.000000
181.000000    1.552662  -115.550056   -0.669662   -1.400826  22222.000000
181.500000    1.513898  -115.786720   -0.658579   -1.363143  22222.000000
182.000000    1.486538  -114.196480   -0.609283   -1.355939  22222.000000
182.500000    1.447400  -112.142113   -0.545532   -1.340657  22222.000000
183.000000    1.382263  -112.188637   -0.522022   -1.279900  22222.000000
183.500000    1.311529  -110.909241   -0.468070   -1.225161  22222.000000
184.000000    1.255151  -110.381996   -0.437141   -1.176568  22222.000000
184.500000    1.169790  -110.306877   -0.405974   -1.097085  22222.000000
185.000000    1.109042  -110.620384   -0.390576   -1.037990  22222.000000
99999.000000  99999.000000  99999.000000  99999.000000  99999.000000  99999.000000

```

Figure A.8: Example of a VAX-Based Scattered-Field Data File (File Name *SASX040393.SUBT*) Showing Scattered-Field Measurement Data for an E-plane Cut of a 5λ Square Plate at 10 GHz

Appendix B

RL/ERCT SYSTEM

The RL Automated Swept Angle Bistatic Scattering Measurement System (ASBSMS) was activated in mid-1986 and continues to be improved and upgraded with the long term goal of 2-40 GHz frequency coverage in each of the following configurations: swept angle bistatic, fixed angle bistatic, and monostatic, with both coherent continuous wave, and stepped frequency synthesized pulse radars employed. This appendix describes the core system only - swept angle bistatic configuration using a coherent continuous radar (2-12.4 GHz). The ASBSMS includes the six subsystems: chamber, receiver, transmitter, positioner, target aligner, and system controller. Each of the subsystems is described in this section. A summary of pertinent technical specifications can be found at the end of this Appendix.

Figure B.1 shows the chamber subsystem. The chamber has the sole function of simulating a free-space environment for the target. The chamber was originally designed for backscattering measurements and thus is not of optimum dimension for bistatic measurements. A coordinate system is superimposed over the floor of the chamber schematic to simplify the subsystem description. The 35'x18'x20' room is lined on all walls, floor, and ceiling with 24" pyramidal absorber except at the center of the back wall where there is a 10'x10' square section of 36' absorber. The 36' absorber section is included to reduce the backscattering from the portion of the wall that when illuminated normal to its surface will scatter energy directly into the receive antenna. The chamber houses the positioner. The azimuth positioner, to which the trussed wooden boom is attached, is bolted to the chamber floor so that its center of rotation is at $X = 157''$, $Y = 64''$. This set-up restricts the measurements to a 180° bistatic angle sector. The distance from the source antenna to the center of rotation of the azimuth positioner determines the maximum target size that will meet the $2\frac{D^2}{\lambda}$ far field criterion. Figure B.2 shows the maximum target dimension that can be accurately measured in the chamber as a function of frequency¹⁰. The distance from the center of rotation of the azimuth positioner to the aperture plane of the transmit antenna (length of boom, R) is 111.2 inches. The transmit antenna and target are moved together in front of the fixed receive antenna. The azimuth positioner is surrounded by an octagonal

¹⁰The rigorous far field requirement has D equal to the sum of the maximum target dimension and the antenna aperture width.

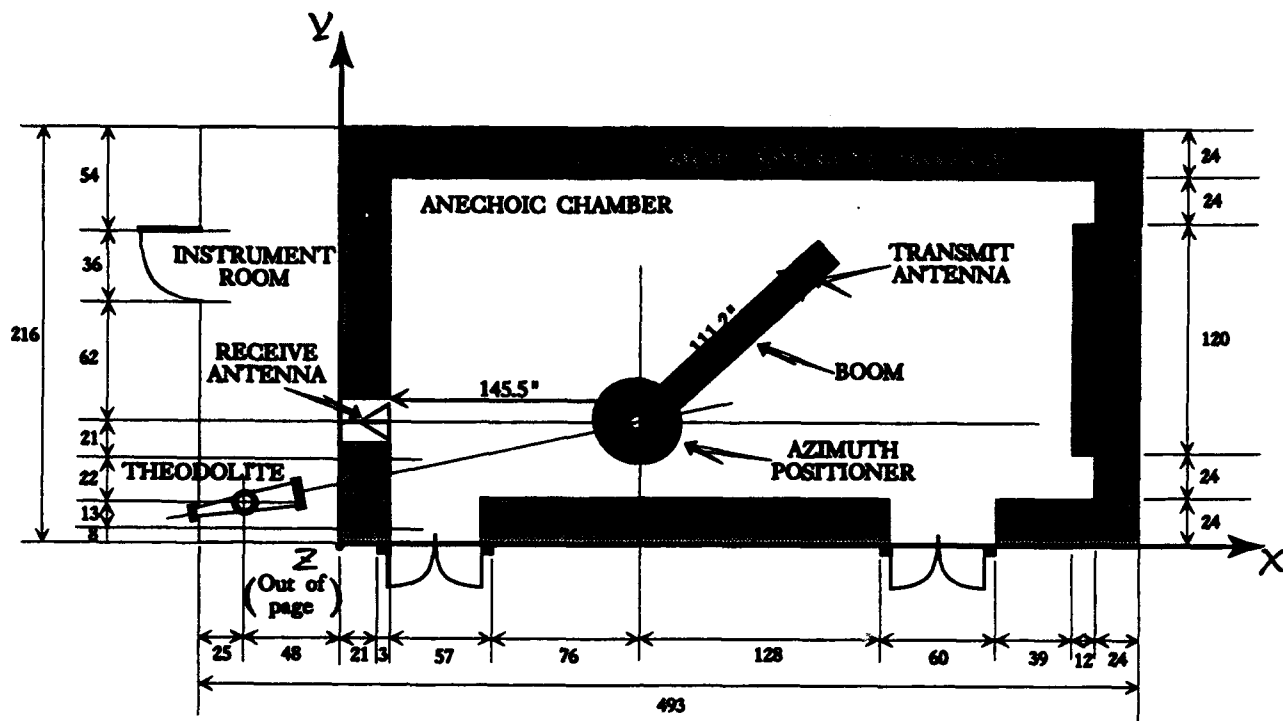


Figure B.1: Anechoic Chamber Subsystem with Cartesian Coordinate System Superimposed. All dimensions are in inches.

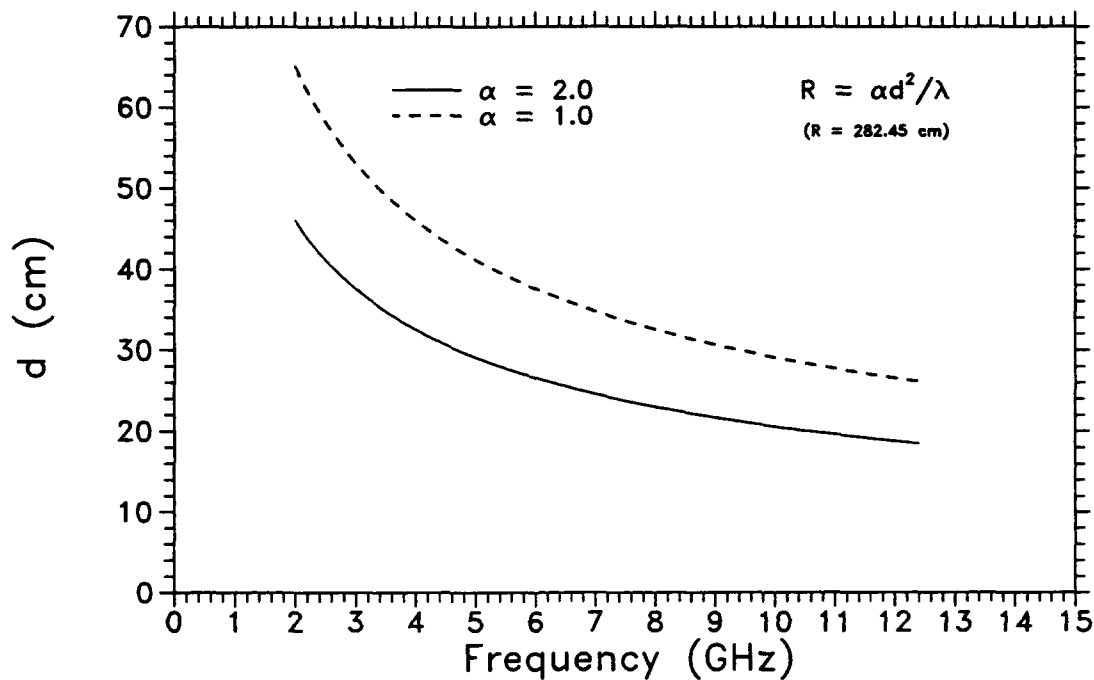


Figure B.2: Maximum Target Dimension for Accurate Scattering Measurements

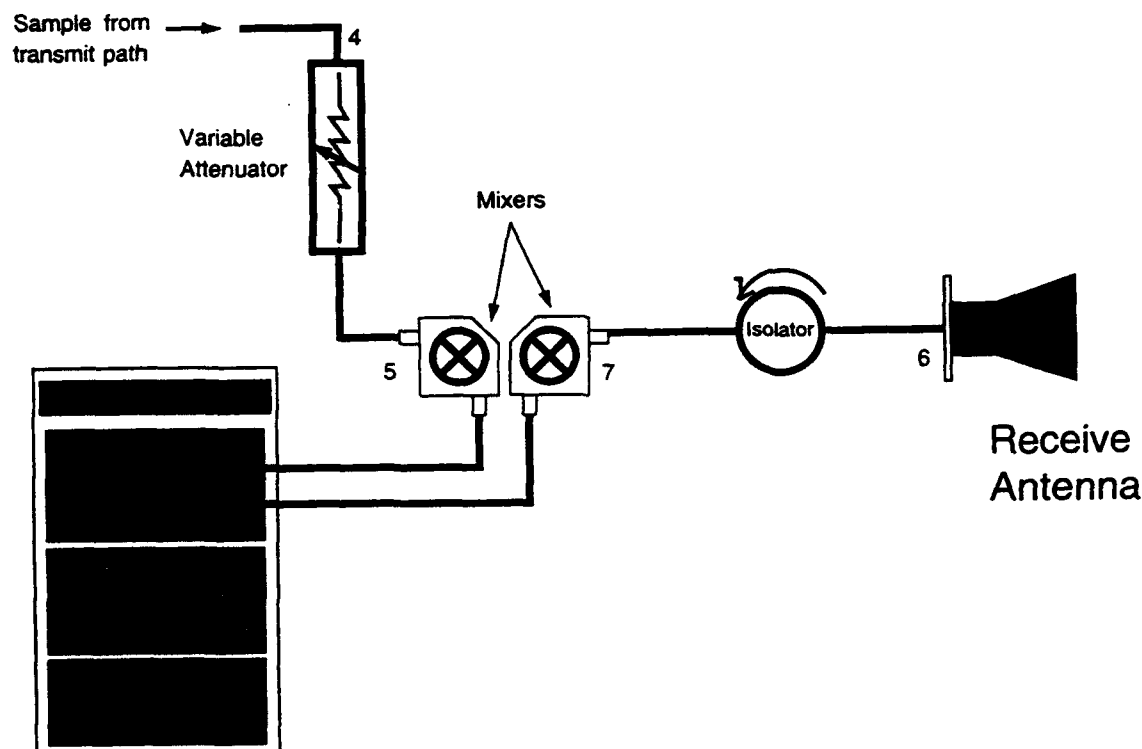


Figure B.3: Receive Subsystem Schematic

wooden skirting with 24 inch pyramidal absorber laid against it to minimize scattering from the metal positioner. The front wall ($x = 0$ plane) has two removable diamond-shaped ports. One (centered at $\{0,72,77\}$ inches) is aluminum and machined to accept the receive antenna and the other (centered at $\{0,38.5,77\}$ inches) is plywood covered with 24 inch pyramidal absorber. It is easily removed and replaced so that targets can be aligned by a theodolite installed in the instrument room located behind the front wall at $\{-48, 21, 72.5\}$ inches.

The receive subsystem is shown in block diagram form in Figure B.3 and includes the receive antenna, receive passive components, signal and reference channels' harmonic mixers, and phase-amplitude receiver. All components are located in the instrumentation room behind the front chamber wall ($x < 0$). The variable attenuator in the RF portion of the reference channel adjusts the reference signal to an optimum level and prevents over-driving the reference channel mixer (SA model 14-5: maximum RF power input is -30 dBm). The isolator on the output of the receive antenna diminishes the effects of multiple reflections between the antenna aperture and the signal channel mixer (also SA model 14-5). The phase-amplitude receiver is a Scientific Atlanta model 1785 [4]. Figure B.4 shows the measured receiver linearity at 10 GHz.

Figure B.5 shows the transmit subsystem which includes a Scientific Atlanta model 2150 signal source with a SA model 2155 frequency synthesizer, an Avantek low noise amplifier

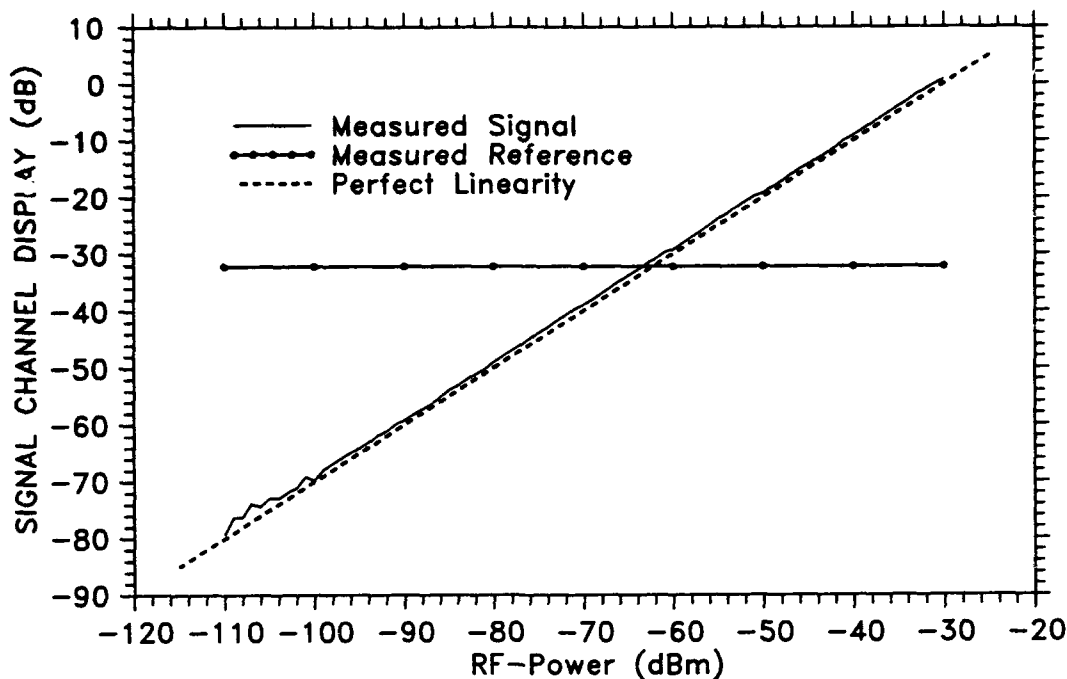


Figure B.4: Measured Linearity of SA-1785 Receiver with SA 14-5 Mixers at 10 GHz

(X-band operation only), isolator, 30 dB directional coupler, and an antenna.

The positioning subsystem is shown in Figure B.6. The positioner is a SA model 53150 azimuth over elevation type with elevation option disabled. The boom, which is bolted to the positioner, was made in house and is constructed of pine boards and studs. An Interface Engineering model 538 positioner controller (located in the instrument room) controls the positioner- boom assembly and provides angle information to a precision of 0.01 degree (positioner accuracy is 0.03 degree).

The target aligning subsystem consists of a theodolite, mounted on a rigid tripod (Keuffel & Esser Co. model 71-5015).

The system controller subsystem, shown in Figure B.7, consists of a Hewlett Packard 9836 desk top computer equipped with 2 megabytes of RAM memory, a HP model 7946 55 megabyte hard disc with cassette tape drive, and an HP model 2563B high speed line printer. The measurement software is written in HP BASIC version 3.0. A complete description of the measurement software is reserved for a future report.

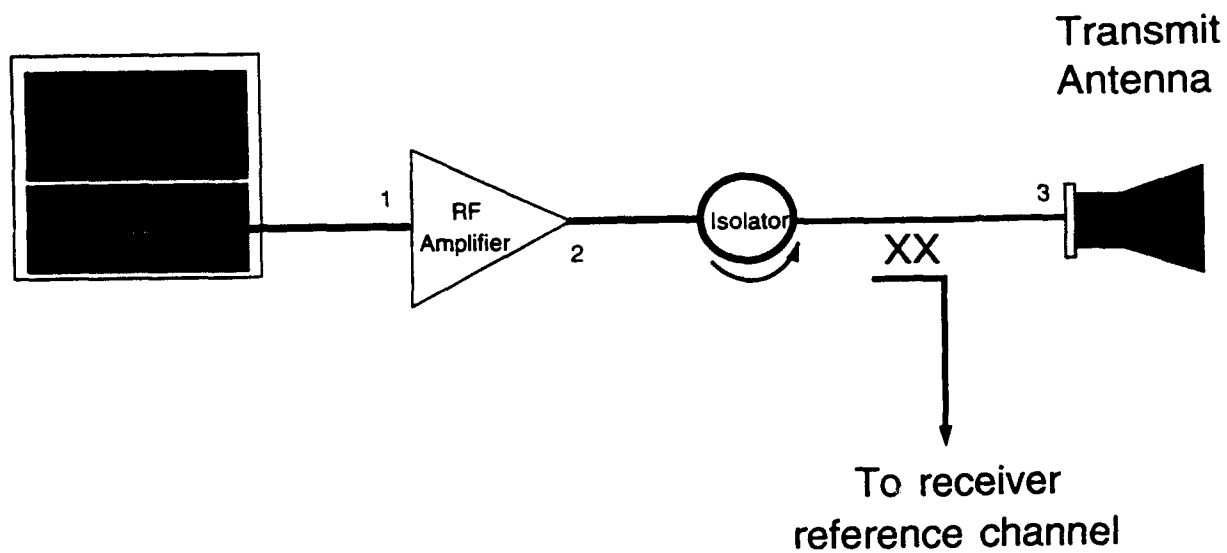


Figure B.5: Transmit Subsystem Schematic

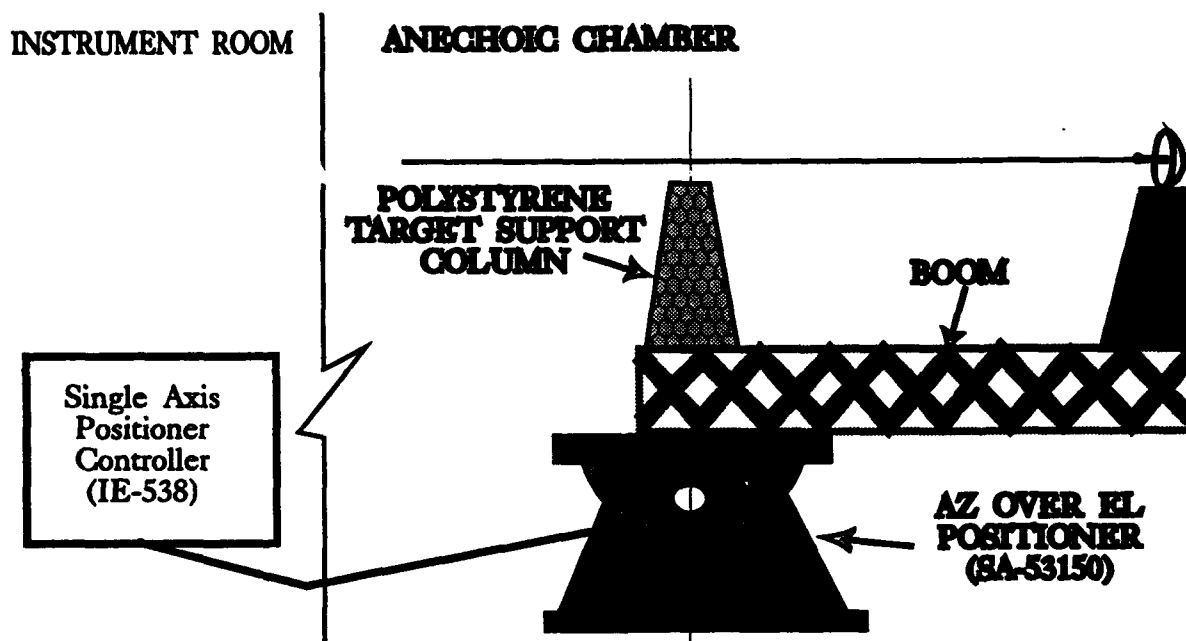


Figure B.6: Schematic Diagram of the ASBSMS Positioning Subsystem

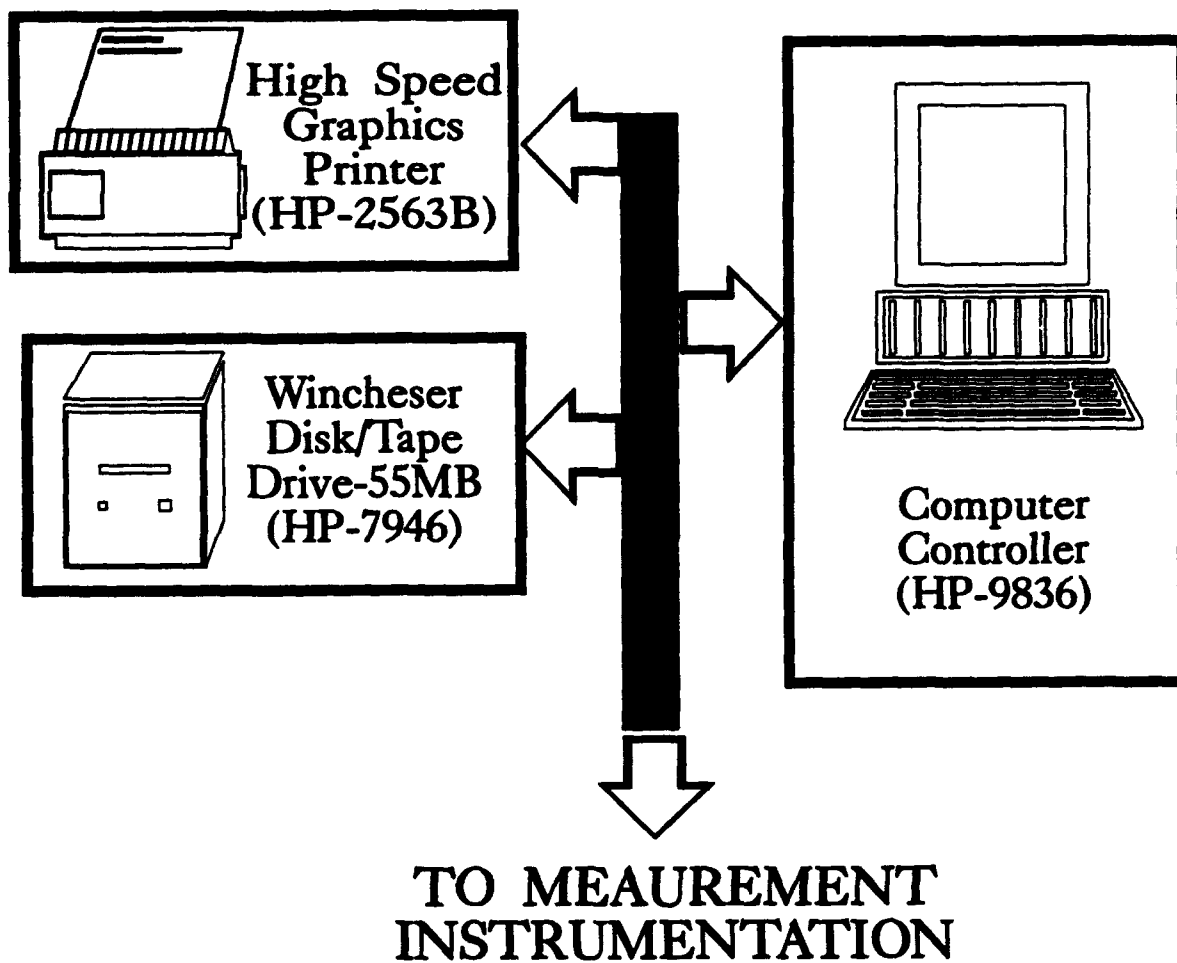


Figure B.7: System Controller Subsystem Schematic

SUMMARY OF THE SYSTEM SPECIFICATIONS

Chamber	:	
Dimensions	:	35' 0" x 18' 0" x 20' 0" (without absorber)
Absorber	:	24" pyramidal absorber on walls, floor, and ceiling except for 10' square section in the center of the back wall where there is 36" pyramidal absorber.
Shielding	:	Absorber attached to foil covered plywood.
Receiver	:	
Receiver	:	Scientific Atlanta Model 1785
Frequency	:	1.0 - 12.2 GHz.
Mixers	:	Scientific Atlanta Model 14-5
Passive components	:	2 Step attenuators (10 dB steps) HP model 8496B 110 dB maximum attenuation, (1 dB steps) HP model 8494B 11 dB maximum attenuation. 1 Directional coupler (20 dB) Narda model 4226-20.
Antennas	:	2 Dipole fed 6" diameter parabolic dishes, (X-band coverage), 2 dual polarized circular horn antennas, EM Systems Inc. Model A6100, 2.0-18.0 GHz coverage. The dual polarized antennas have wide beamwidths at S-band frequencies. This makes all but targets with high RCS difficult or impossible to measure accurately.
Transmitter	:	
Source	:	Scientific Atlanta Model 2150 with Model 2155 Synthesizer.
Amplifiers	:	AVANTEK Model AWT-18057 (X-band operation only)
Frequency	:	1.0 - 12.2 GHz
Power output	:	+15 dBm (maximum)
Frequency Stability	:	$\pm 6\text{ppm}$ This means a maximum phase error of $\frac{0.0022}{\Delta\ell}$. Where $\Delta\ell$ is the difference between the reference and scattering paths in wavelengths. For our system this difference is 1034 cm. At 10 GHz, $\Delta\ell \sim 345\lambda$, which gives a maximum phase error due to frequency instability of about 0.76° .
Positioner	:	
Positioner	:	Scientific Atlanta Model 53150 azimuth over elevation. Elevation option is disabled.
Controller	:	Interface Engineering Model 538 programmable. Controllable over the IEEE-488 interface bus and is a listen only device (it cannot interrupt the system controller).
Target Aligner	:	
Theodolite	:	Keuffel & Esser Co. Model 71-5015
System Controller	:	
Computer	:	Hewlett Packard Model 9836 microcomputer.
Printer	:	Hewlett Packard Model 2563B
Data Storage	:	Hewlett Packard Model 7946 Disc/Tape drive (55 Mbyte)

Appendix C

BACKGROUND LEVELS AT 10 GHz

This Appendix demonstrates the background level, background stability, and the background behavior with time for both H-plane and E-plane cuts at 10 GHz. In addition we derive the lower limit of 53 dB below the ambient background power for measuring target scattering. This limit is a numerical limit due to amplitude resolution of the receiver.

The 10 GHz background data presented was collected as part of a series of H-plane and E-plane scattering measurements made on a set of 3 aluminum spheres ($ka = 5.32, 7.98, \text{ and } 21.29$) to characterize the impact of a system configuration change on the system measurement performance. The H-plane and E-plane data were collected over a period of 3 and 5 days respectively. The experiment was a series of alternating sphere and background measurements with adherence to the operating procedure put forth in Section 3 of this report. As discussed in Section 3, spheres, by virtue of their symmetry, require no alignment prior to measurement and therefore the chamber environment is essentially undisturbed when the sphere is installed or removed from the target mount. The background measurements are a realistic representation of the behavior of the background with time. The data are presented in five different forms:

1. calibrated raw measurements in amplitude $[\sigma_b(\theta)]$, and relative phase ($\angle[E_b(\theta)]$),
2. calibrated raw measurements averaged over the measurement period $\sigma_b^{AVG}(\theta)$ and $\angle[E_b^{AVG}(\theta)]$,
3. calibrated residual backgrounds $[\sigma_{\Delta b}(\theta)]$,
4. residual backgrounds averaged over the measurement period ($\sigma_{\Delta b}^{AVG}$), and
5. ratio of consecutive measurements $|\epsilon_i(\theta)|$, $\angle[\epsilon_i(\theta)]$.

Figures C.1, C.2, and C.3 show the calibrated H-plane backgrounds for day 1, day 2, and day 3 of the measurement period. Three E-plane calibrated backgrounds spanning the 5-day measurement period are plotted in Figures C.4, C.5, and C.6. Comparing the H-plane

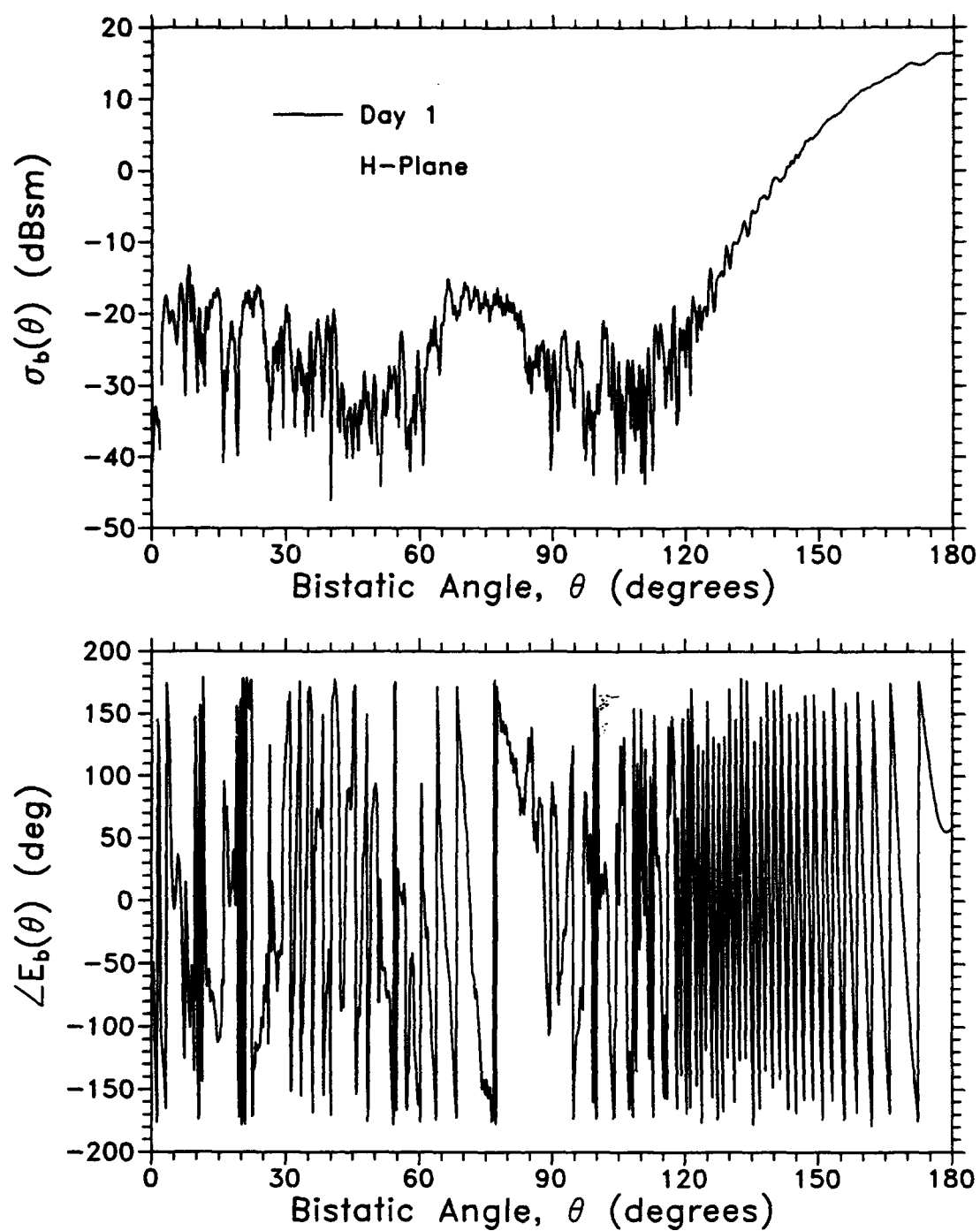


Figure C.1: Calibrated H-plane Background Measurement Collected on the First Day of the Experiment

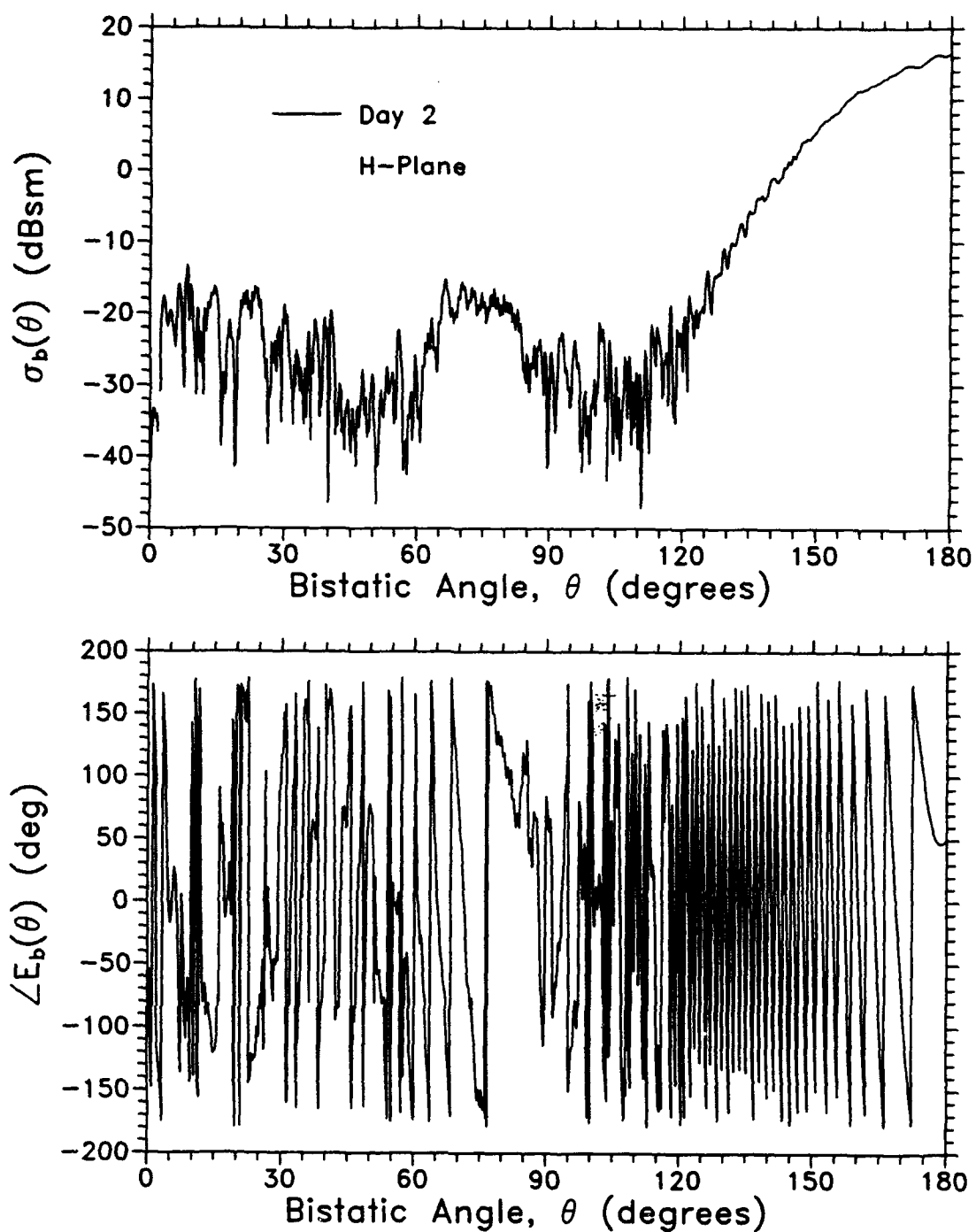


Figure C.2: Calibrated H-plane Background Measurement Collected on the Second Day of the Experiment

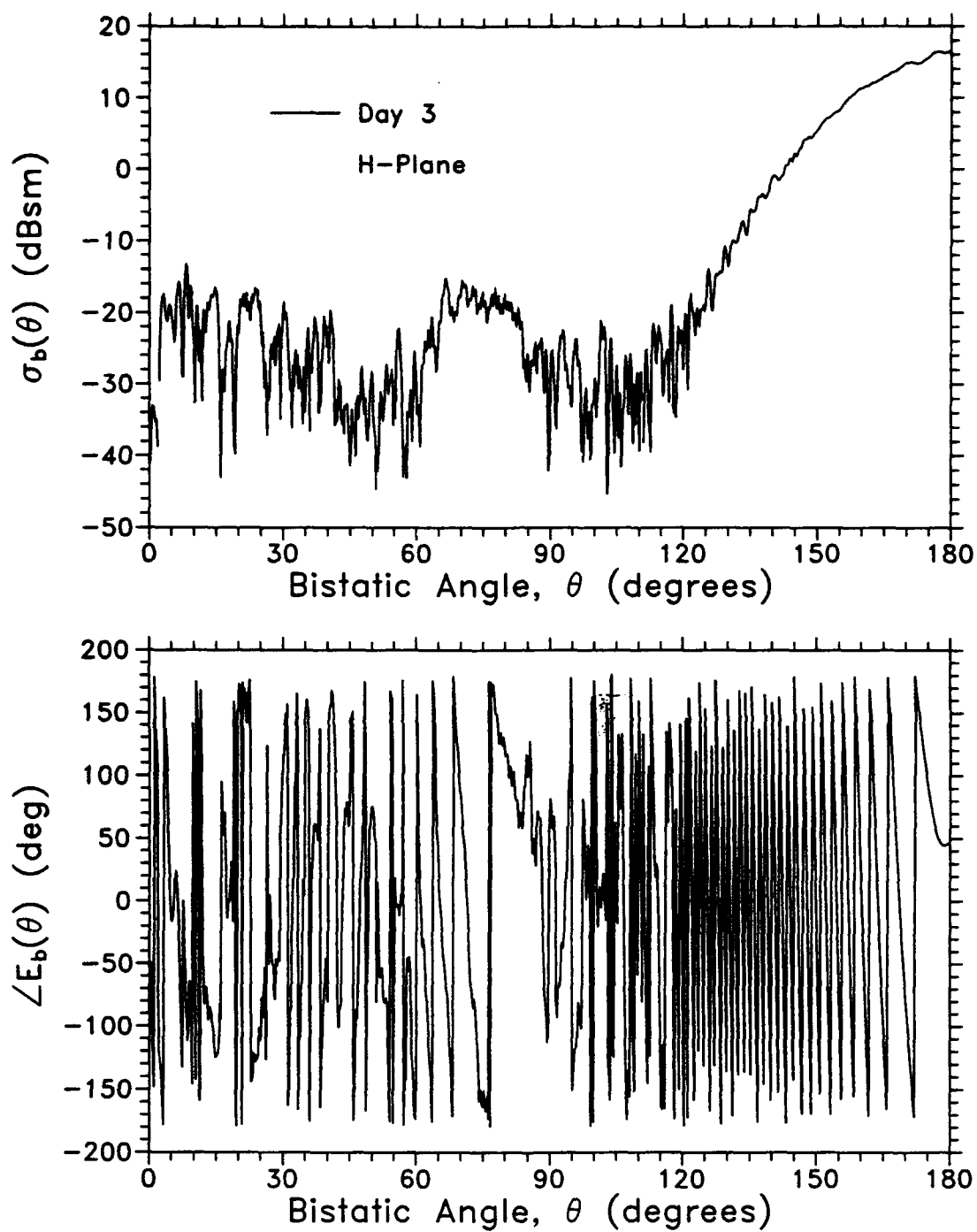


Figure C.3: Calibrated H-plane Background Measurement Collected on the Third Day of the Experiment

and E-plane backgrounds we notice that the H-plane background is slightly lower than the nominally -15 dBsm E-plane background, and the H-plane phase varies more slowly than the E-plane phase in the backscattering region especially between $\theta = 60^\circ$ and $\theta = 90^\circ$. The slowly varying phase with the corresponding distinct lobe in the power pattern of the H-plane cut indicates that there is some structure in the chamber that is scattering vertically polarized fields with an intensity significantly higher than the direct coupling fields. The rapidly varying phase of the E-plane background from backscatter to forward scatter shows that for horizontally polarized fields the chamber has no significant localized scatterers. Figures C.7 and C.8 show the average H-plane and E-plane backgrounds, respectively. The averages were computed using Eqs. (C.1) and (C.2).

$$\sigma_b^{AVG}(\theta) = \left[\frac{1}{N} \sum_{\tau=0}^{\Delta T} \sqrt{\sigma_b^{\tau}(\theta)} \right]^2, \quad (C.1)$$

$$\angle[E_b^{AVG}(\theta)] = \pm \frac{1}{N} \sum_{\tau=0}^{\Delta T} | \angle[E_b^{\tau}(\theta)] |, \quad (C.2)$$

where τ is the approximate time relative to the first background measurement made on the first measurement day of the background measurement being summed, ΔT is the duration of the measurement period (approximately 3 days for H-plane and 5-days for E-plane), N is the number of backgrounds in the ensemble, and σ_b indicates the calibrated background RCS. The \pm in Eq. (C.2) is chosen to correspond to the sign of $\angle[E_b^0(\theta)]$. For each cut about 10 background measurements were averaged ($N = 10$). We note no significant difference between the average background and the individual backgrounds for either H-plane or E-plane cuts.

The calibrated residual background radar cross section (RCS) estimates the lowest RCS measurable with the ASBSMS. Figure C.9 shows the H-plane residual RCS ($\sigma_{\Delta b}$) for time separations (ΔT) between backgrounds of about 1 hour and 26 hours. We notice that for the typical time separation between total field and background field measurements of about an hour (Figure C.9) the residual background RCS is nominally -50 dBsm in the backscattering region and rises to about -30 dBsm near forward scatter. For the 26 hour separation (Figure C.10) we notice a marked rise in the nominal RCS to about -35 dBsm in the backscattering region and nearly +5 dBsm at forward scatter. This rise was traced to a constant phase offset of about 10° that was introduced into the system at the start of the third measurement day. The cause of the shift is not known but could be due to many factors, for example, a slight adjustment in the source power level, a change in the signal or reference channel IF attenuation, or a change in the reference channel RF attenuation. The phase offset will become more evident later in this appendix. Figure C.10 illustrates the importance of maintaining system continuity from total field measurement to background measurement. For the E-plane, (Figures C.11 and C.12) the residual background RCS is about 5 dB higher in the backscattering region and about the same near forward scatter when compared with the H-plane. Figures C.13 and C.14 show the average residual RCS

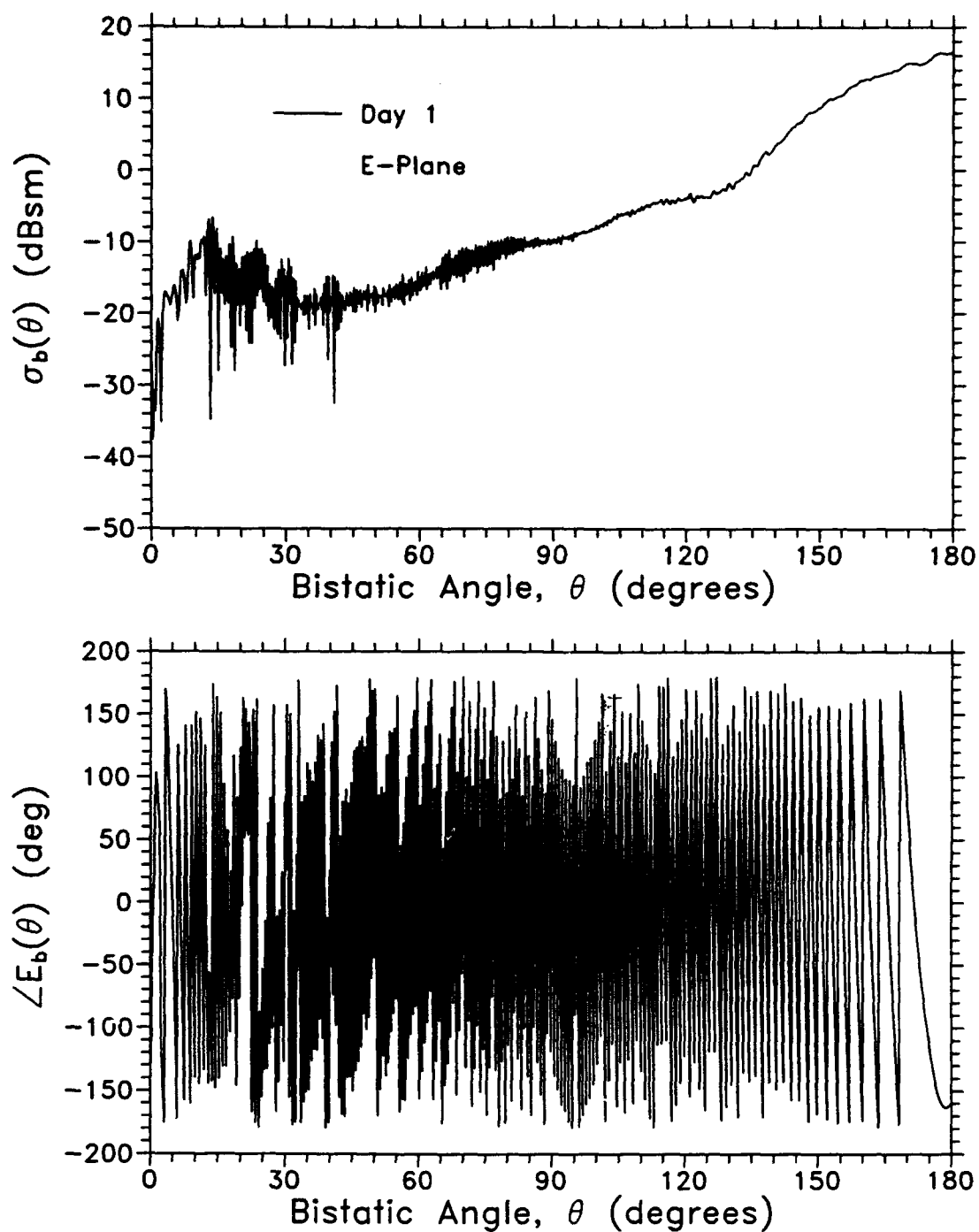


Figure C.4: Calibrated E-plane Background Measurement Collected on the First Day of the Experiment

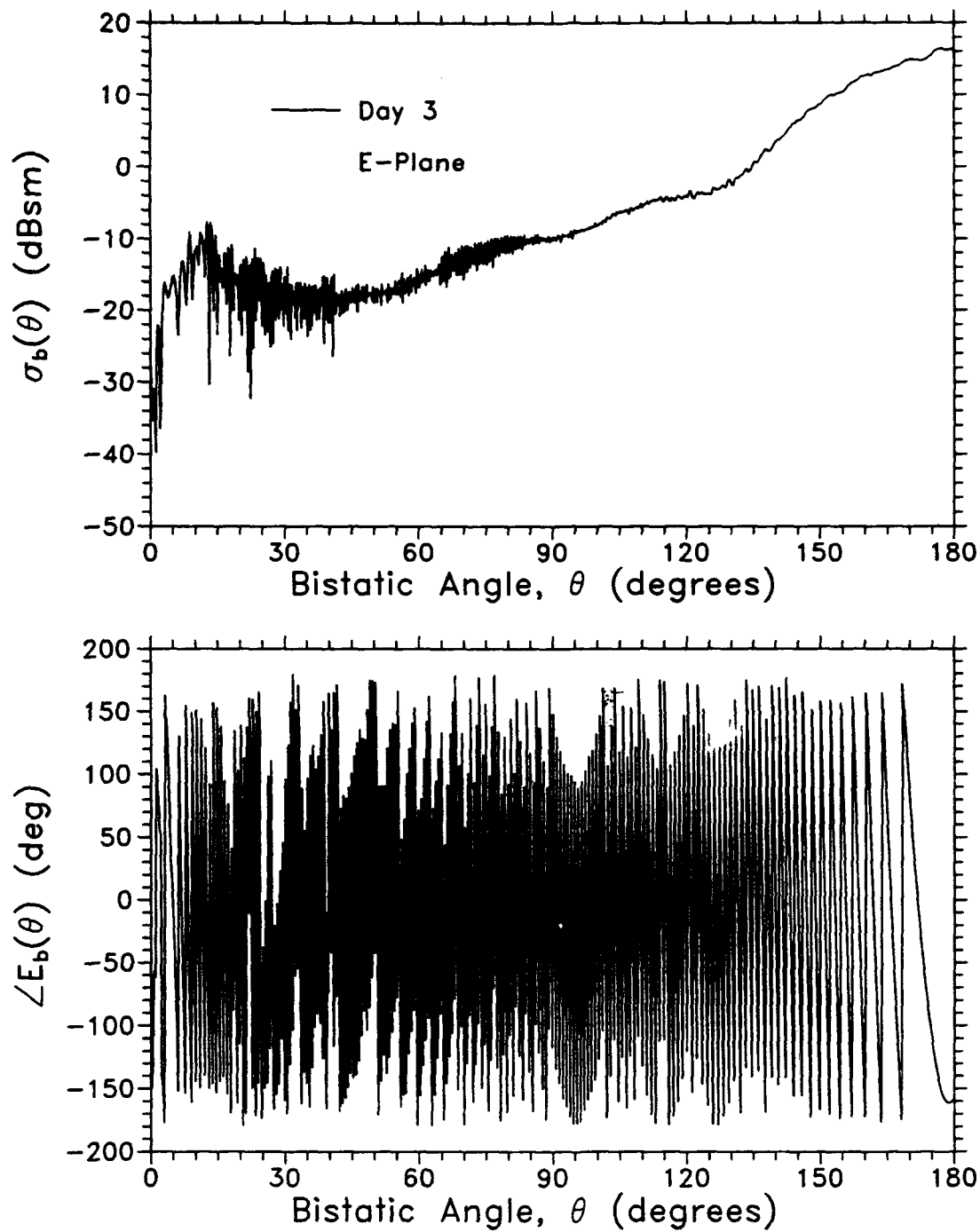


Figure C.5: Calibrated E-plane Background Measurement Collected on the Third Day of the Experiment

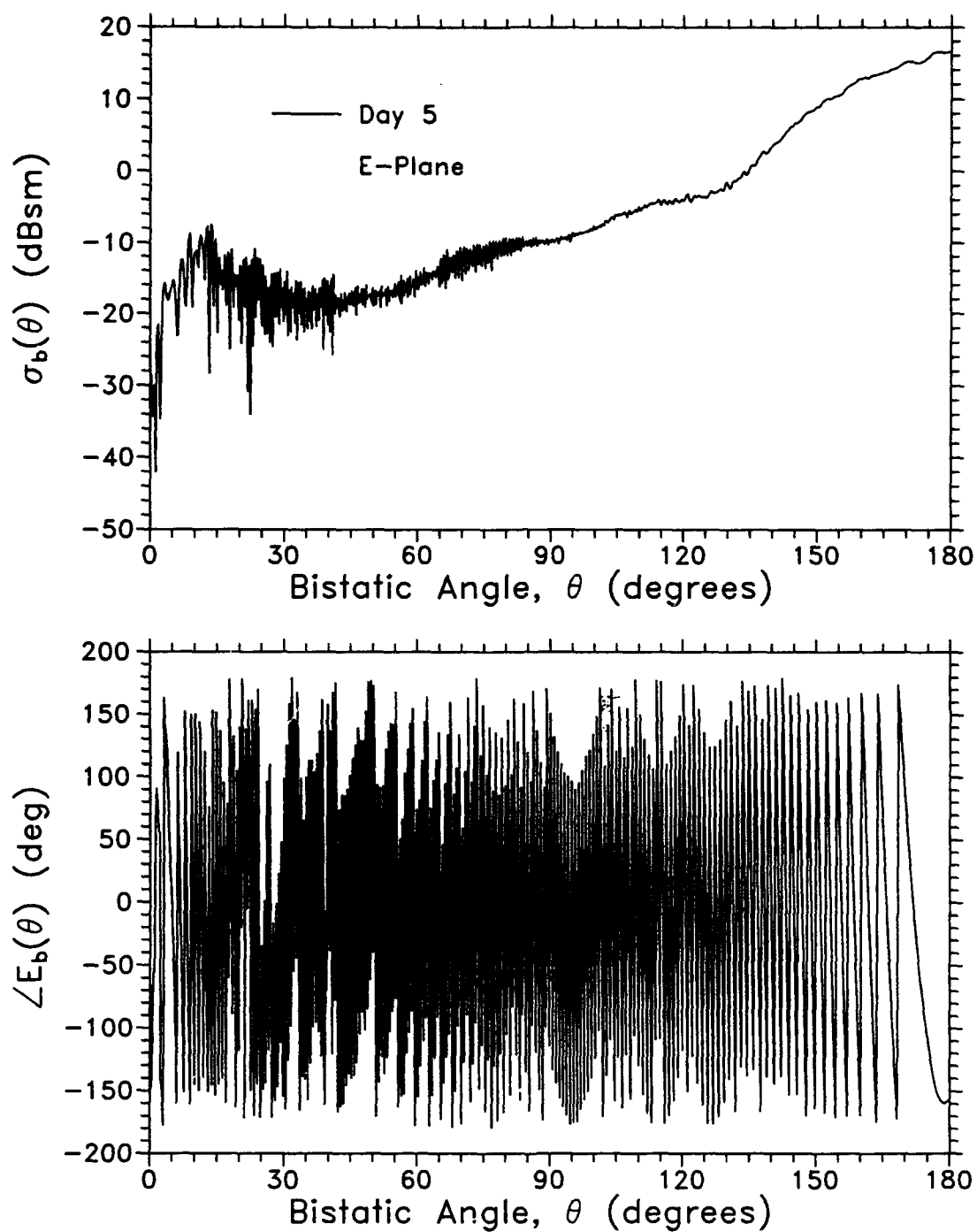


Figure C.6: Calibrated E-plane Background Measurement Collected on the Fifth Day of the Experiment

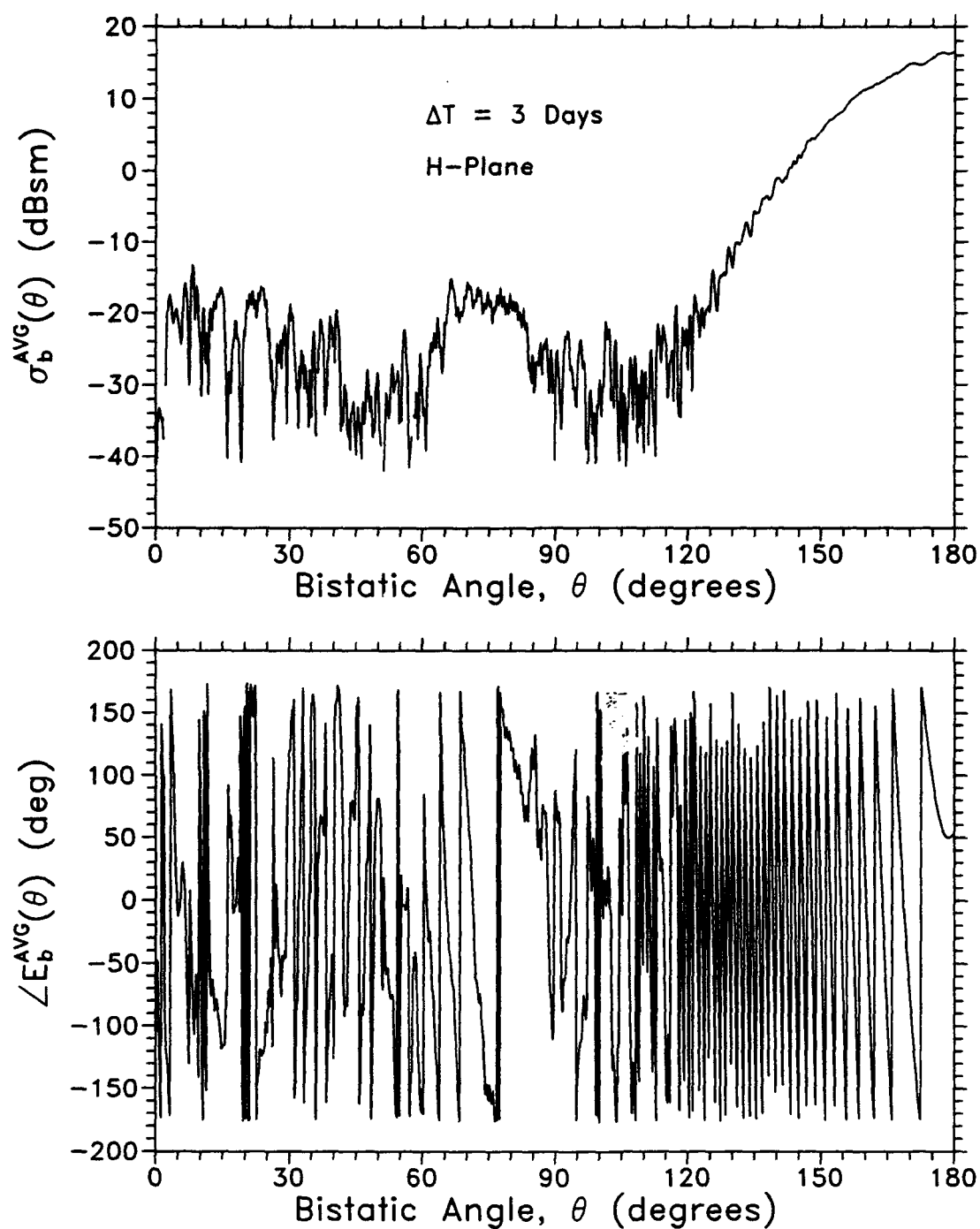


Figure C.7: Average Calibrated H-plane Background Measurements. Ten background data sets spread over three days of the experiment were averaged to obtain the plot.

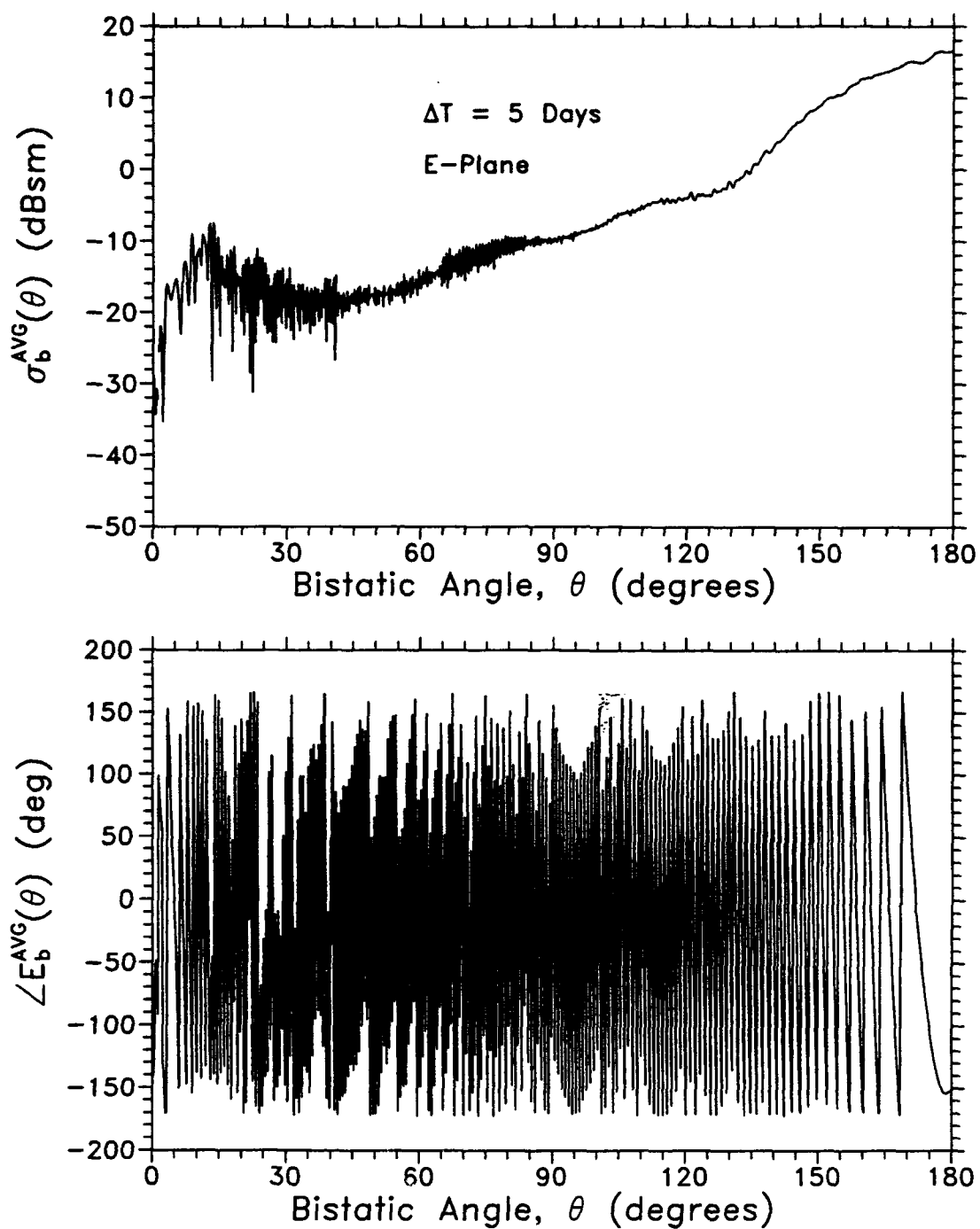


Figure C.8: Average Calibrated E-plane Background Measurements. Ten background data sets spread over five days of the experiment were averaged to obtain this plot.

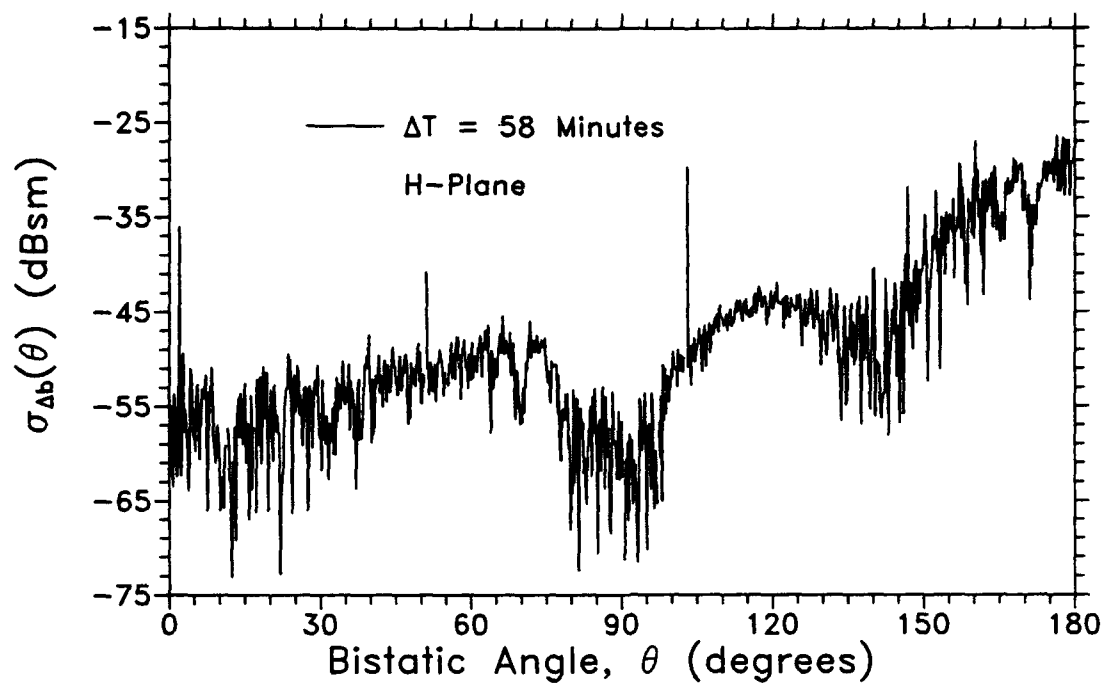


Figure C.9: Calibrated H-plane Residual Background Computed for Two Background Measurements Separated in Time by Approximately 1 Hour

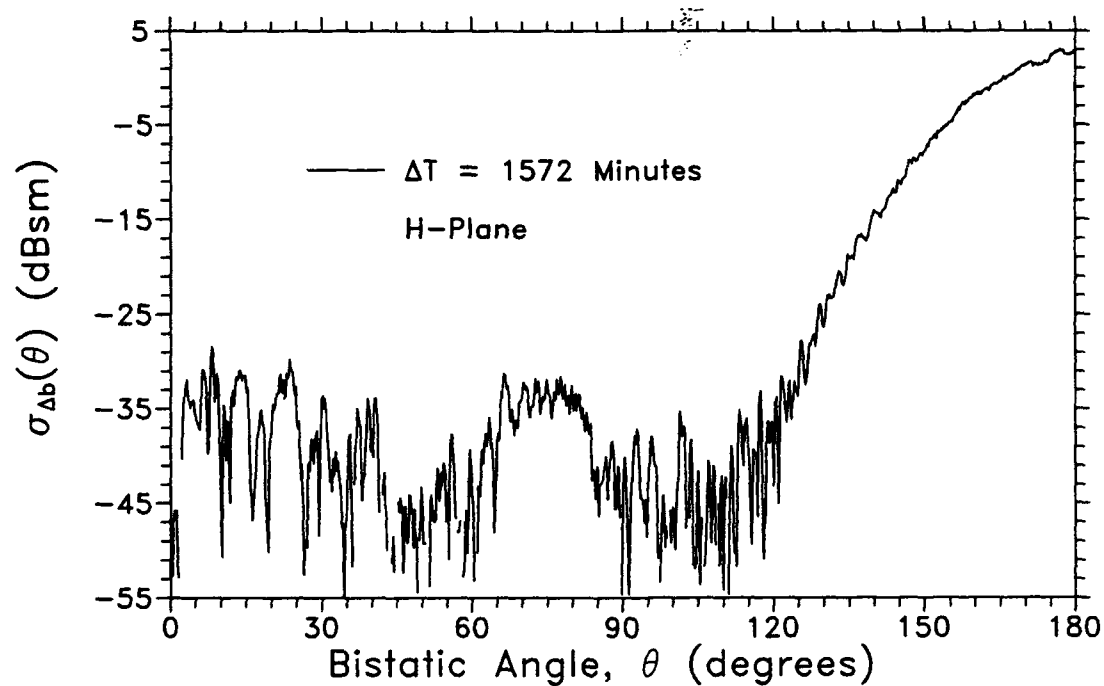


Figure C.10: Calibrated H-plane Residual Background Computed for Two Background Measurements Separated in Time by Approximately 1 day and 2 Hours

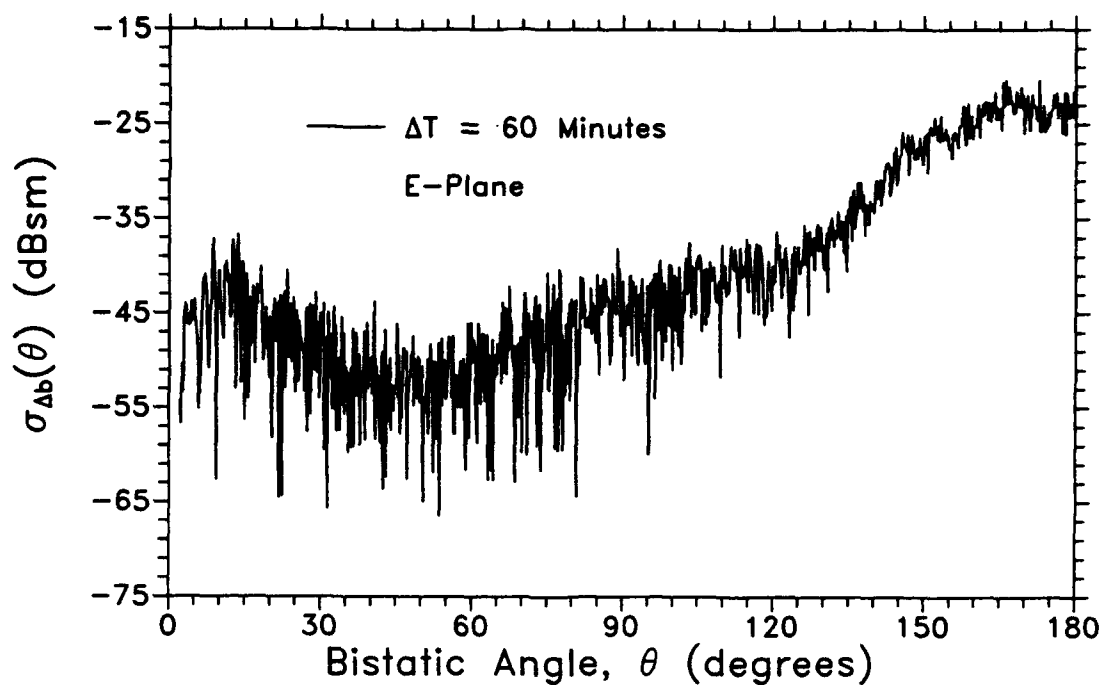


Figure C.11: Calibrated E-plane Residual Background Computed for Two Background Measurements Separated in Time by Approximately 1 Hour

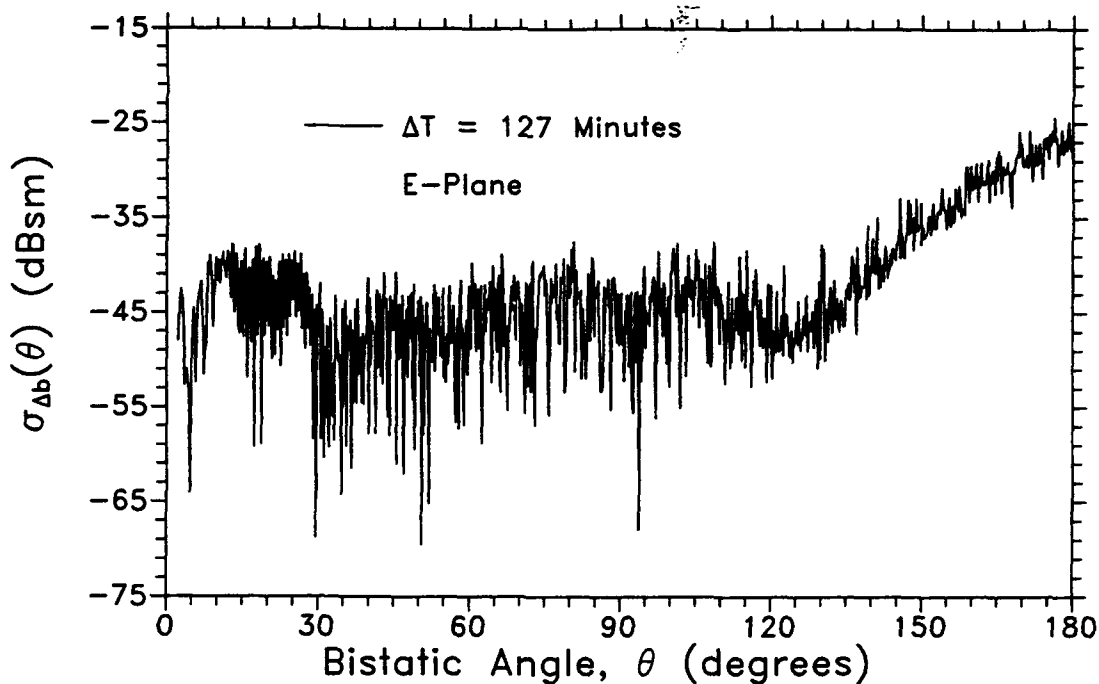


Figure C.12: Calibrated E-plane Residual Background Computed for Two Background Measurements Separated in Time by About 2 Hours

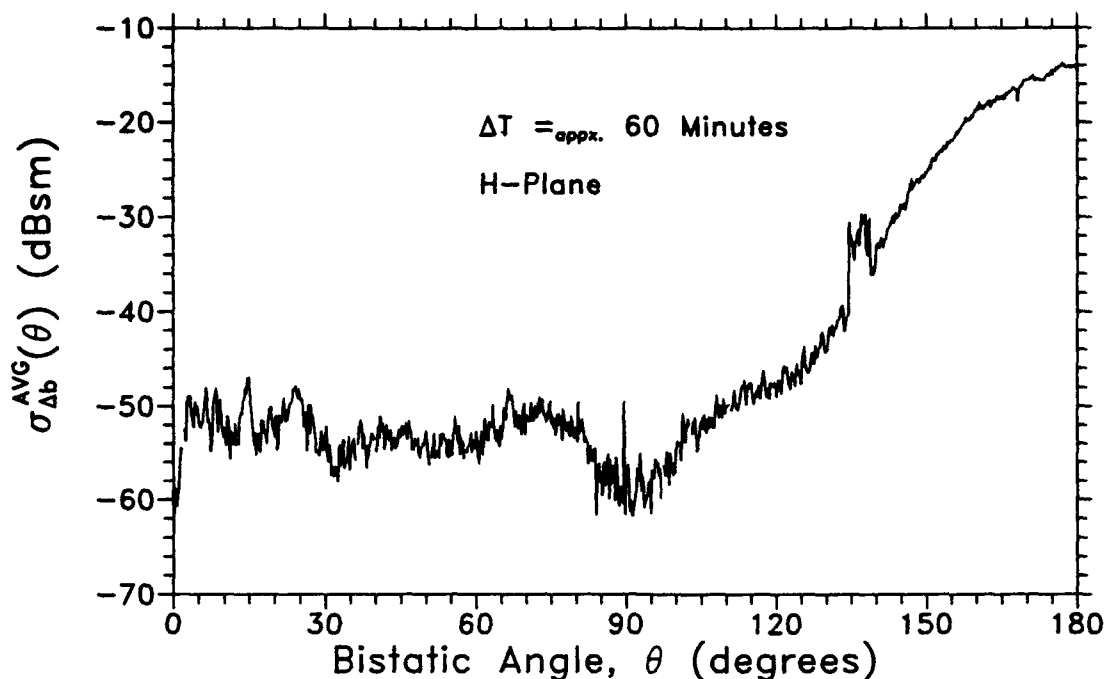


Figure C.13: Average Calibrated H-plane Residual Backgrounds. Only residual backgrounds computed from backgrounds separated in time by approximately 1 hour were considered.

($\sigma_{\Delta b}^{AVG}$) respectively, for the H-plane and E-plane. Using Eq. (C.1)¹¹, averages were computed on all the residual background with separation times of about 1 hour taken over the 3 and 5 day measurement periods. We notice that the H-plane and E-plane averages are much more similar than the individual residual background RCS curves shown in Figures C.9 and C.11. Both planes are nominally -50 dBsm in the backscattering region with the H-plane slightly higher than the E-plane near forward scatter. The glitch in the H-plane curve near $\theta = 135^\circ$ is typical, linked to one data field, and its cause is not known.

To show the behavior of the background with time we have plotted a series of background perturbation phasors, $\epsilon_t(\theta)$ (Equation 5.2), dividing the first background measurement with subsequent backgrounds. The subscript, t , indicates the elapsed time between the numerator and denominator background fields. A perturbation phasor having amplitude 1 and phase 0 represents a perfectly repeated background. Deviations in the amplitude that are much greater than 1 are amplified relative to those less than 1. For example a 90% difference in the background amplitudes are either 10 or 0.1, that is, 9 units above 1, or 0.9 units below 1. This should be kept in mind as one studies the figures.

The H-plane series is presented in Figures C.15 through C.24 with time separations ranging from about 1 hour to just over 48 Hours. We note two distinct excursions from the ideal, one centered near $\theta = 50^\circ$ and the other near $\theta = 115^\circ$. In the forward scattering region we see a relatively flat amplitude and phase due to the dominance of the very repeatable

¹¹ Phase information is meaningless for residual backgrounds.

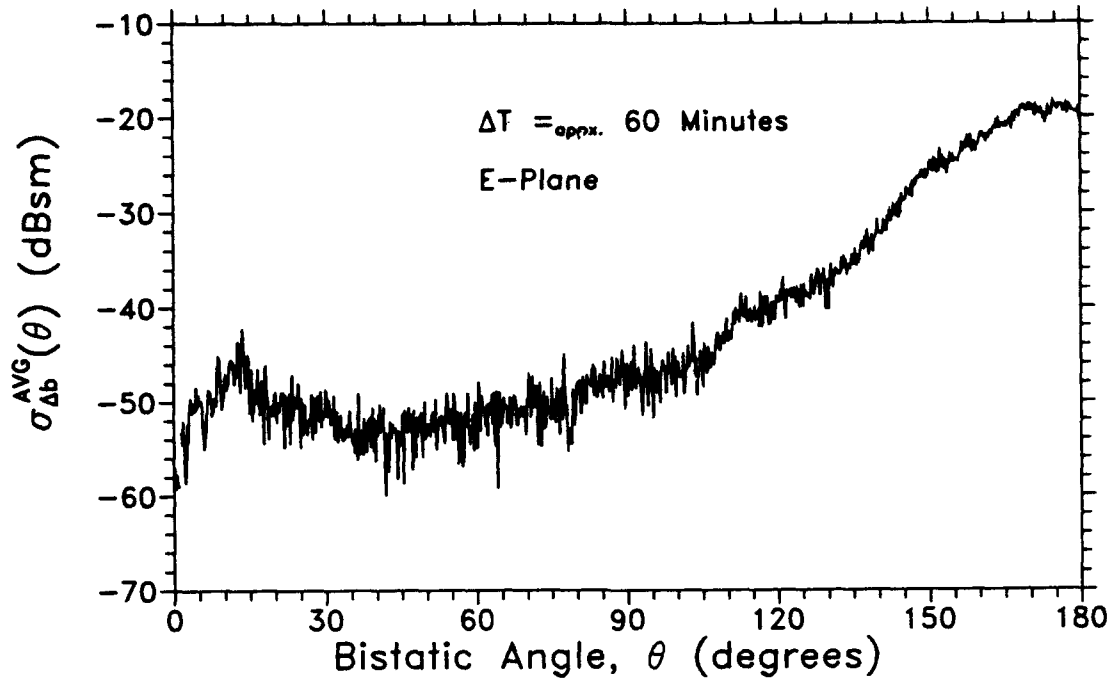


Figure C.14: Average Calibrated E-plane Residual Backgrounds. Only residual backgrounds computed from backgrounds separated in time by approximately 1 hour were considered.

direct coupling of the transmit and receive antenna main lobes. In Figures C.15 through C.18 we note both the amplitude and phase curves vary about the ideal, $|\epsilon| = 1$ and $\angle[\epsilon] = 0^\circ$. These curves were computed with data collected on the first and second measurement days. Data taken on the third measurement day are shown in Figures C.19 through C.24. We notice that for these data the phase curves vary about $+10^\circ$, indicating a change in the system as discussed earlier in this appendix. Studying the phasors taken collectively shows a general degradation in the backscattering region ($0^\circ < \theta < 40^\circ$) with time and very little change in the forward scattering regions.

For the E-plane, Figures C.25 through C.35, we observe deviations from the ideal near backscatter and a very flat response over the observation sector, $40^\circ < \theta < 180^\circ$. Figures C.28 through C.31 show a phase shift of about -15° and represent data taken on the third measurement day. This phase shift is not observed on the fourth measurement day as can be seen from Figures C.32 through C.35. The general trend is a worsening response with time, over the observation sector $0^\circ < \theta < 90^\circ$ with a stable response from $\theta = 90^\circ$ to forward scatter. Comparing the H-plane and E-plane perturbation phasors shows that the E-plane is much more stable (repeatable) than the H-plane. This is because the H-plane background power pattern is about 10 dB lower than the E-plane, and therefore has lower measurement accuracy.

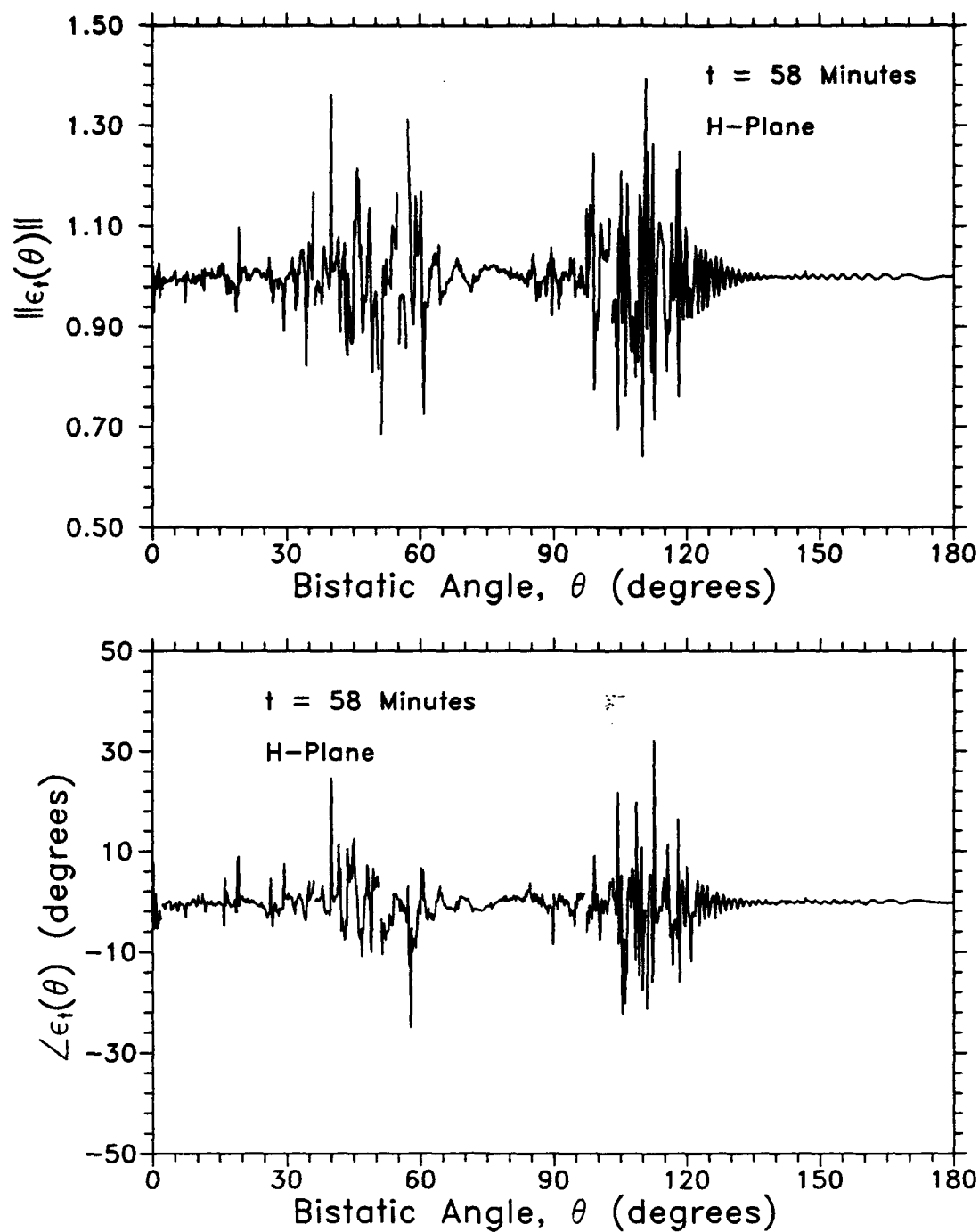


Figure C.15: Perturbation Phasor Computed from Two H-plane Background Measurements Separated in Time by Approximately 1 Hour

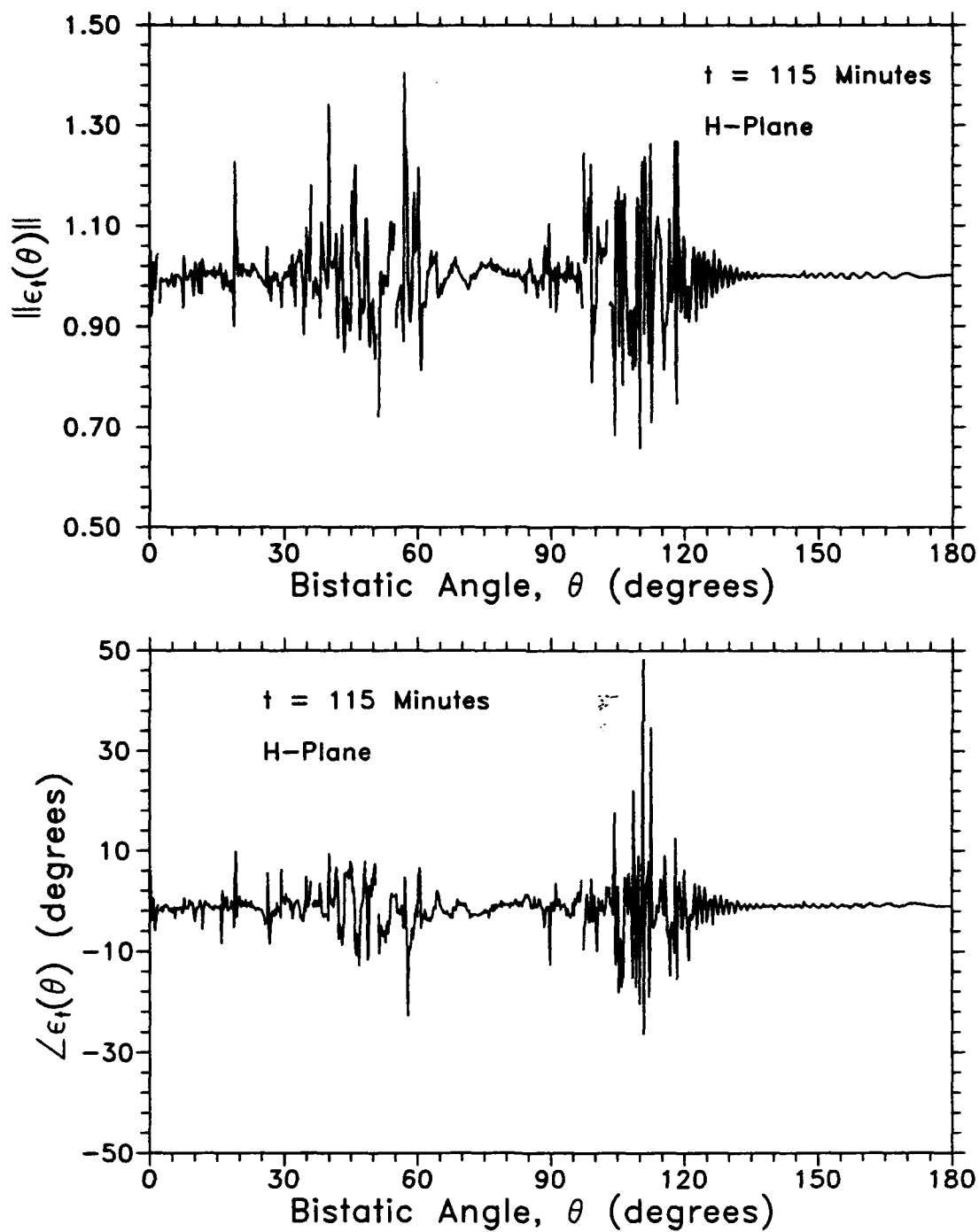


Figure C.16: Perturbation Phasor Computed from Two H-plane Background Measurements Separated in Time by About 2 Hours

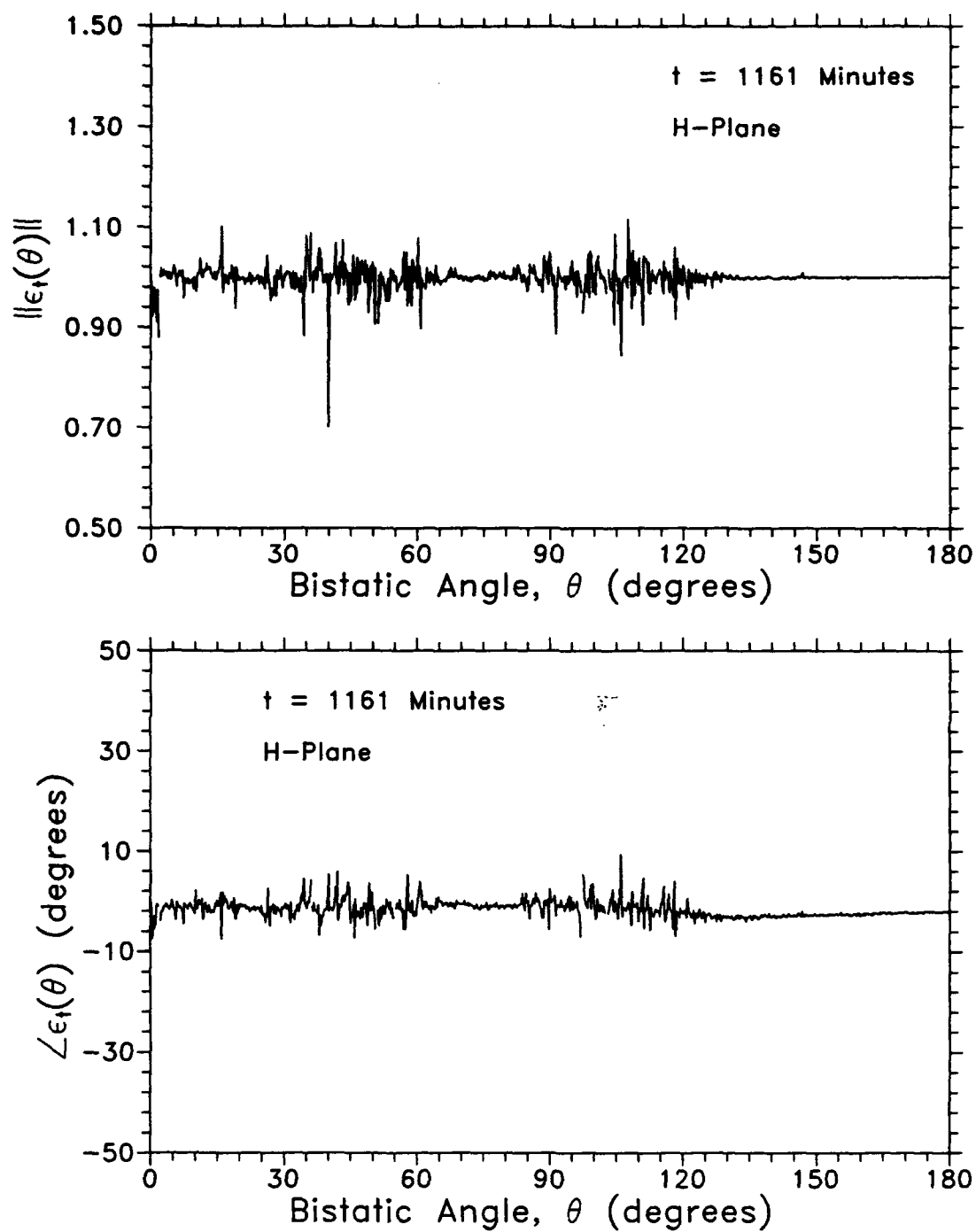


Figure C.17: Perturbation Phasor Computed from Two H-plane Background Measurements Separated in Time by About 19 Hours

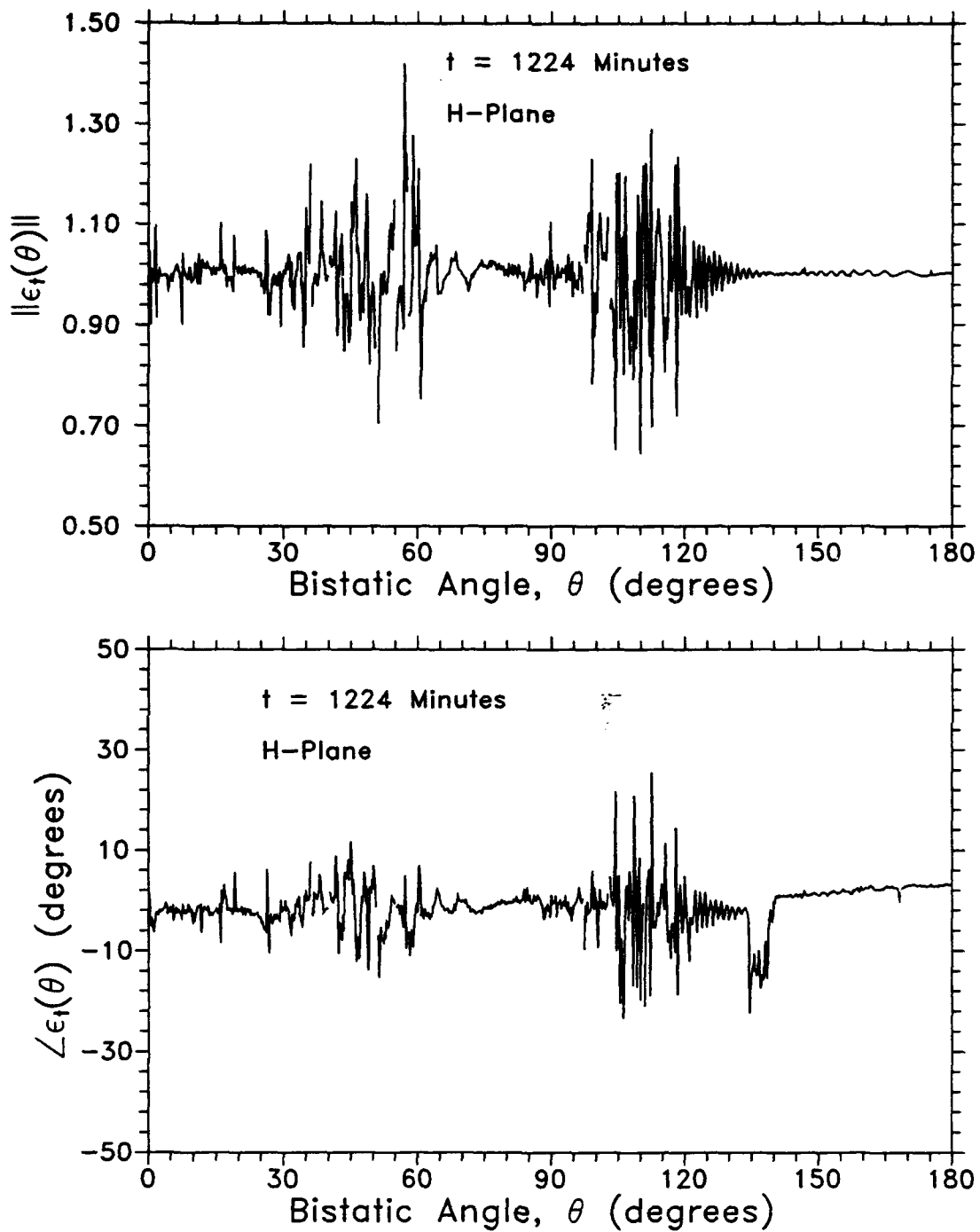


Figure C.18: Perturbation Phasor Computed from Two H-plane Background Measurements Separated in Time by About 20 Hours

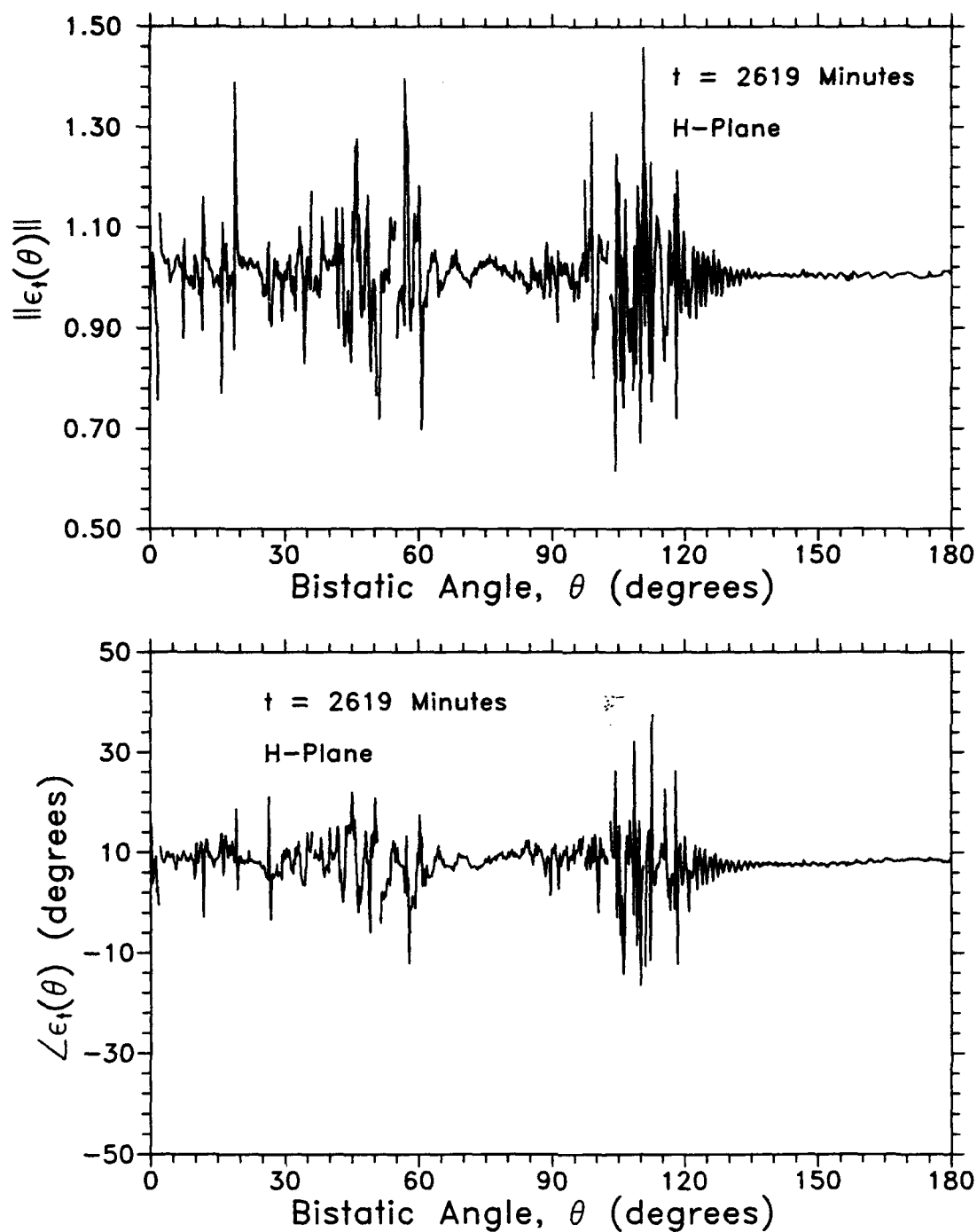


Figure C.19: Perturbation Phasor Computed from Two H-plane Background Measurements Separated in Time by About 44 Hours

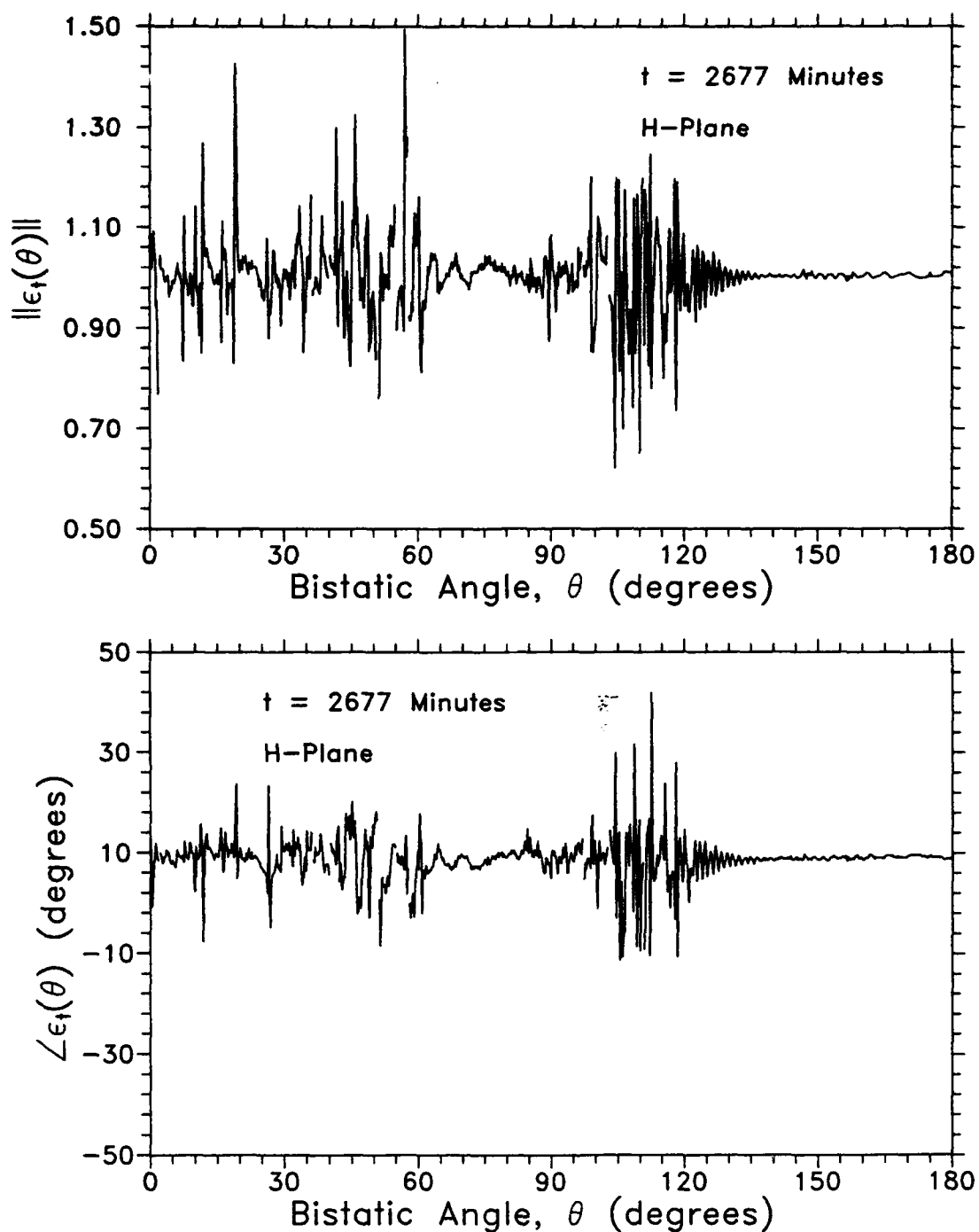


Figure C.20: Perturbation Phasor Computed from Two H-plane Background Measurements Separated in Time by About 45 Hours

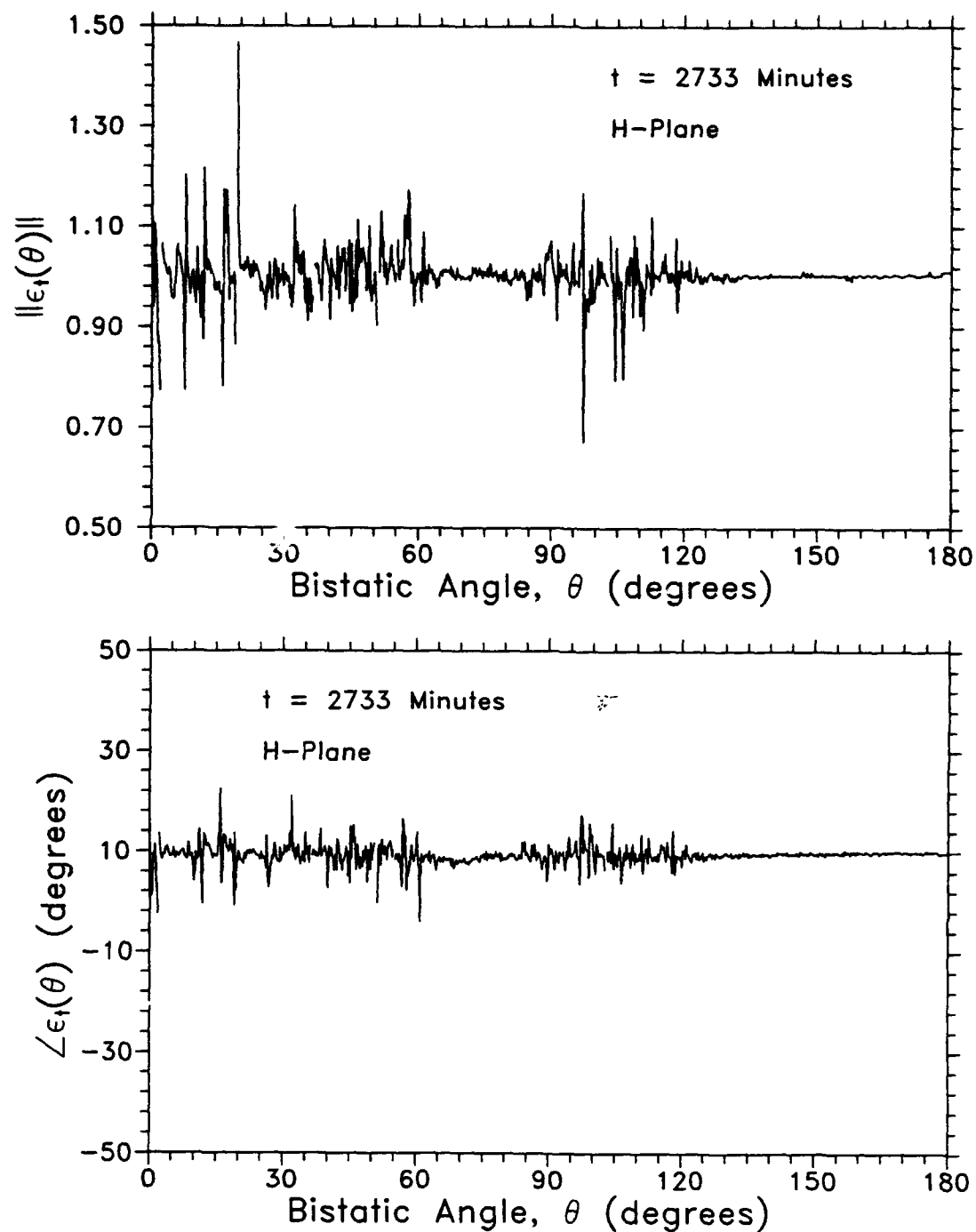


Figure C.21: Perturbation Phasor Computed from Two H-plane Background Measurements Separated in Time by About 46 Hours

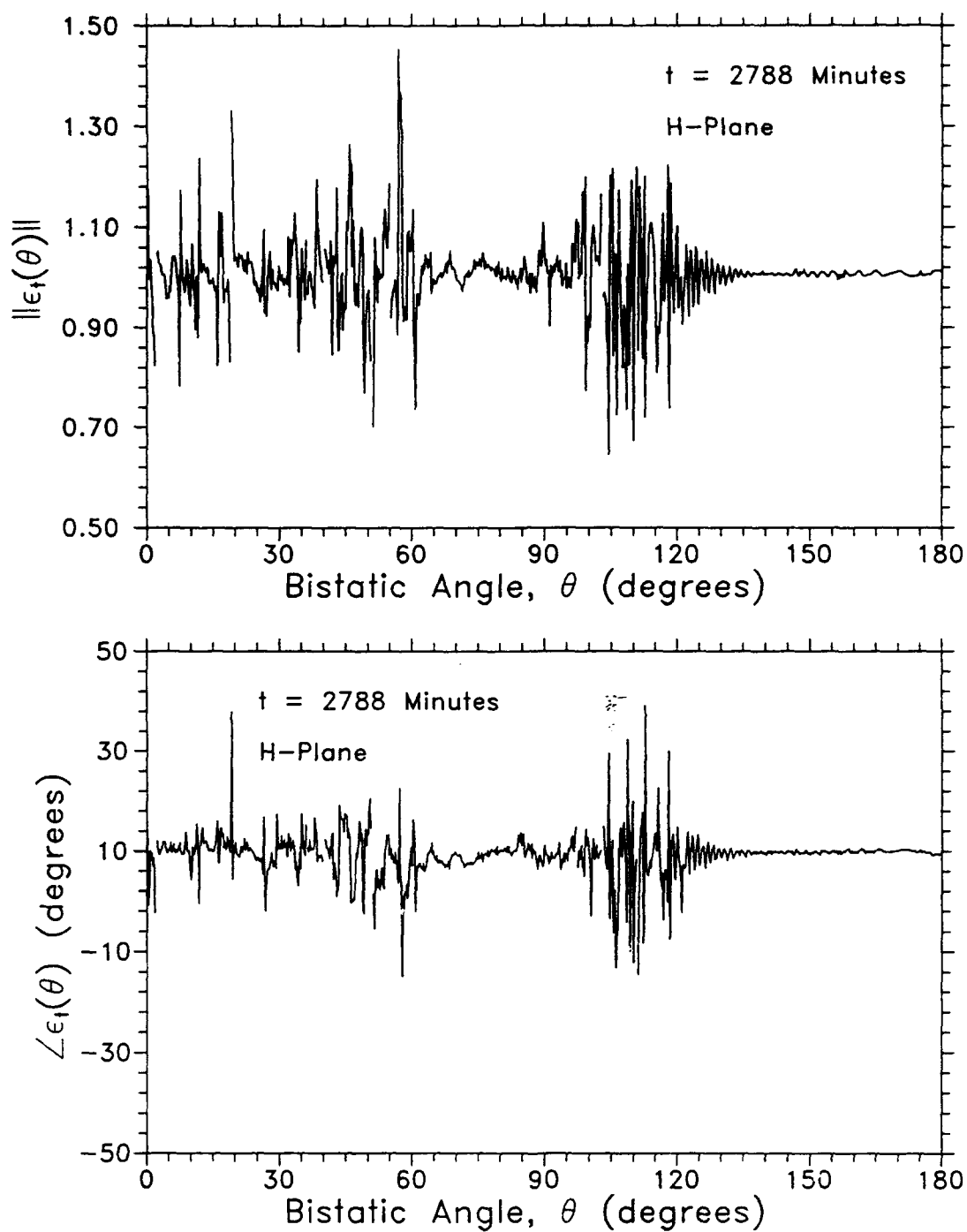


Figure C.22: Perturbation Phasor Computed from Two H-plane Background Measurements Separated in Time by About 46.5 Hours

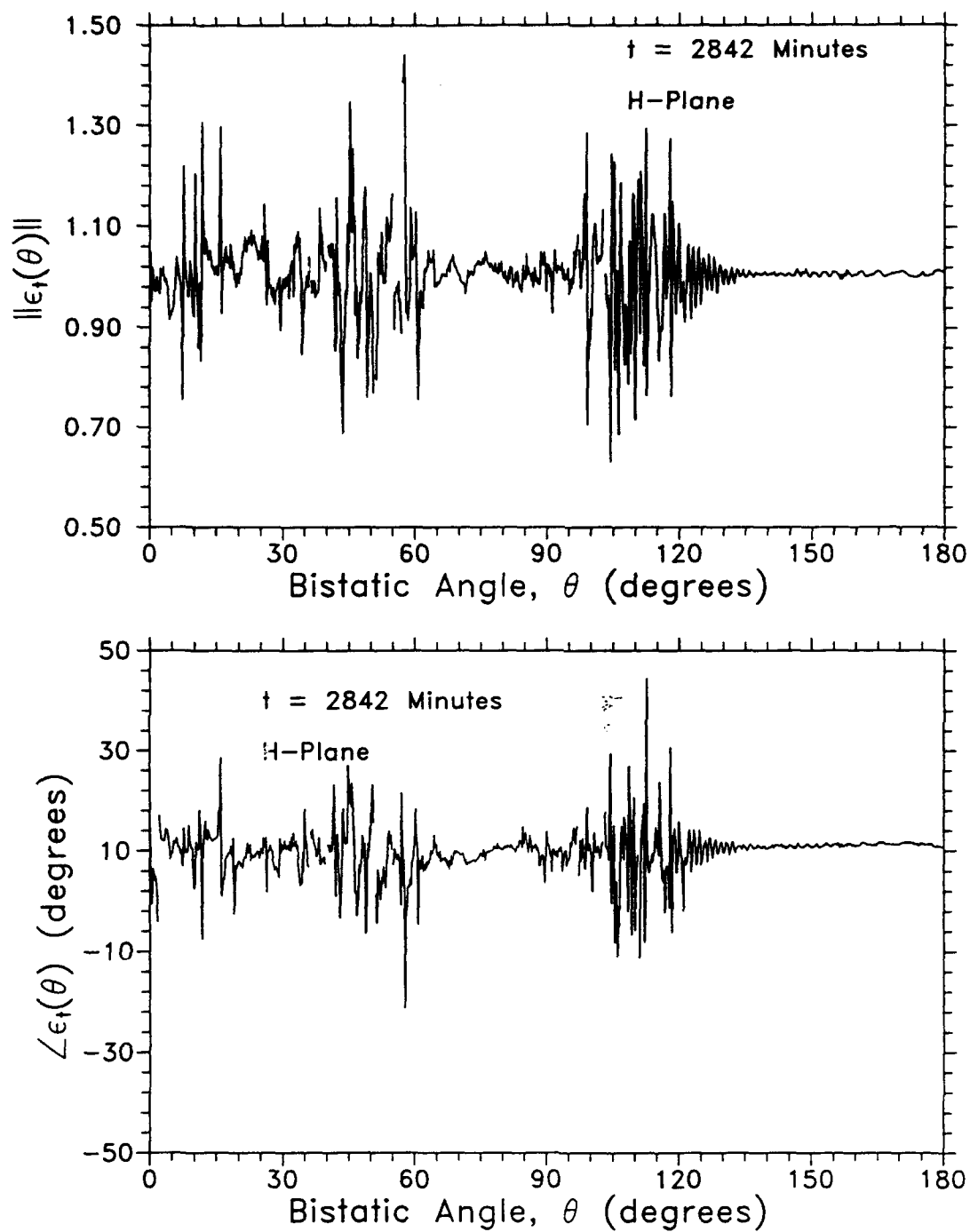


Figure C.23: Perturbation Phasor Computed from Two H-plane Background Measurements Separated in Time by About 47.4 Hours

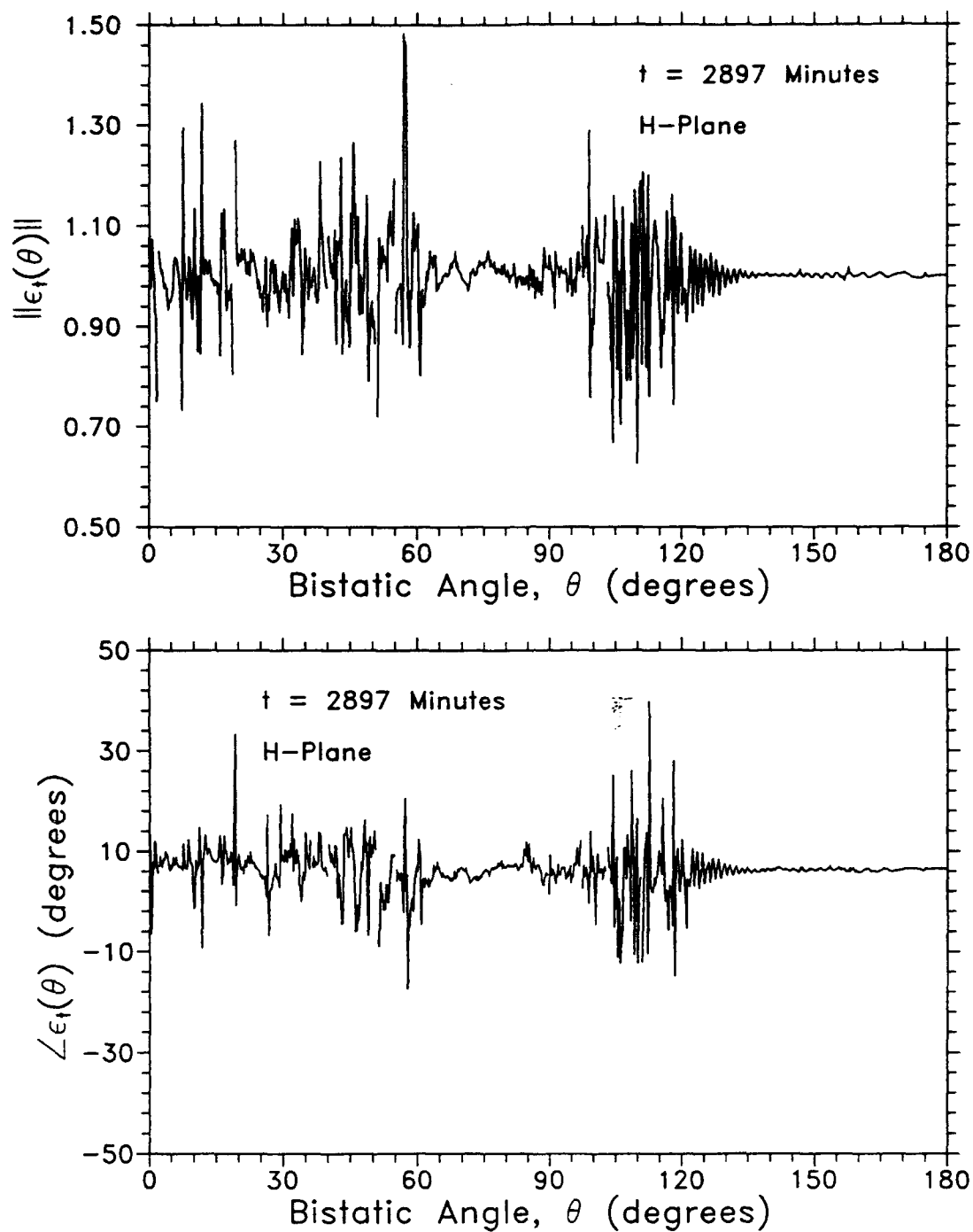


Figure C.24: Perturbation Phasor Computed from Two H-plane Background Measurements Separated in Time by About 48.3 Hours

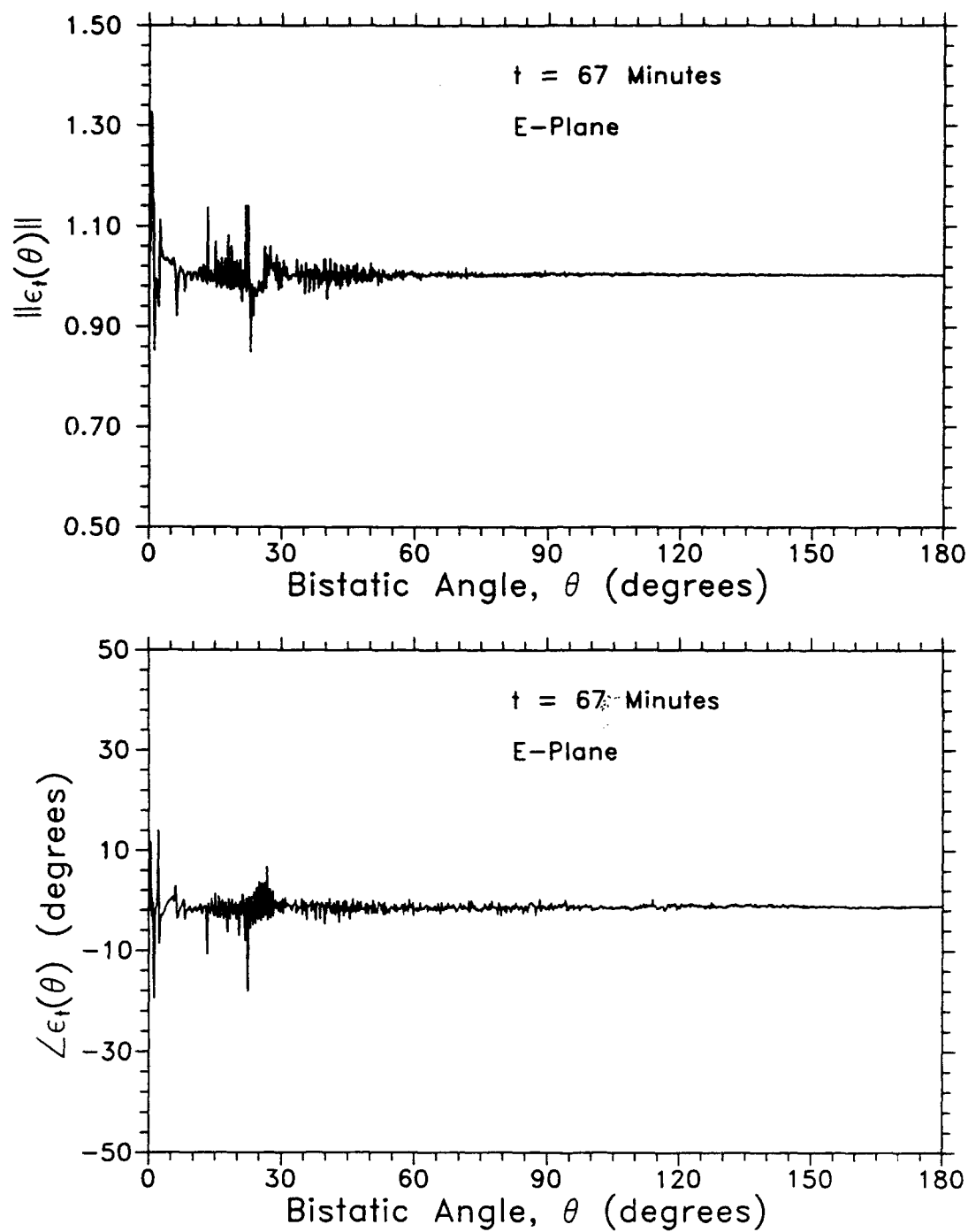


Figure C.25: Perturbation Phasor Computed from Two E-plane Background Measurements Separated in Time by Approximately 1 Hour

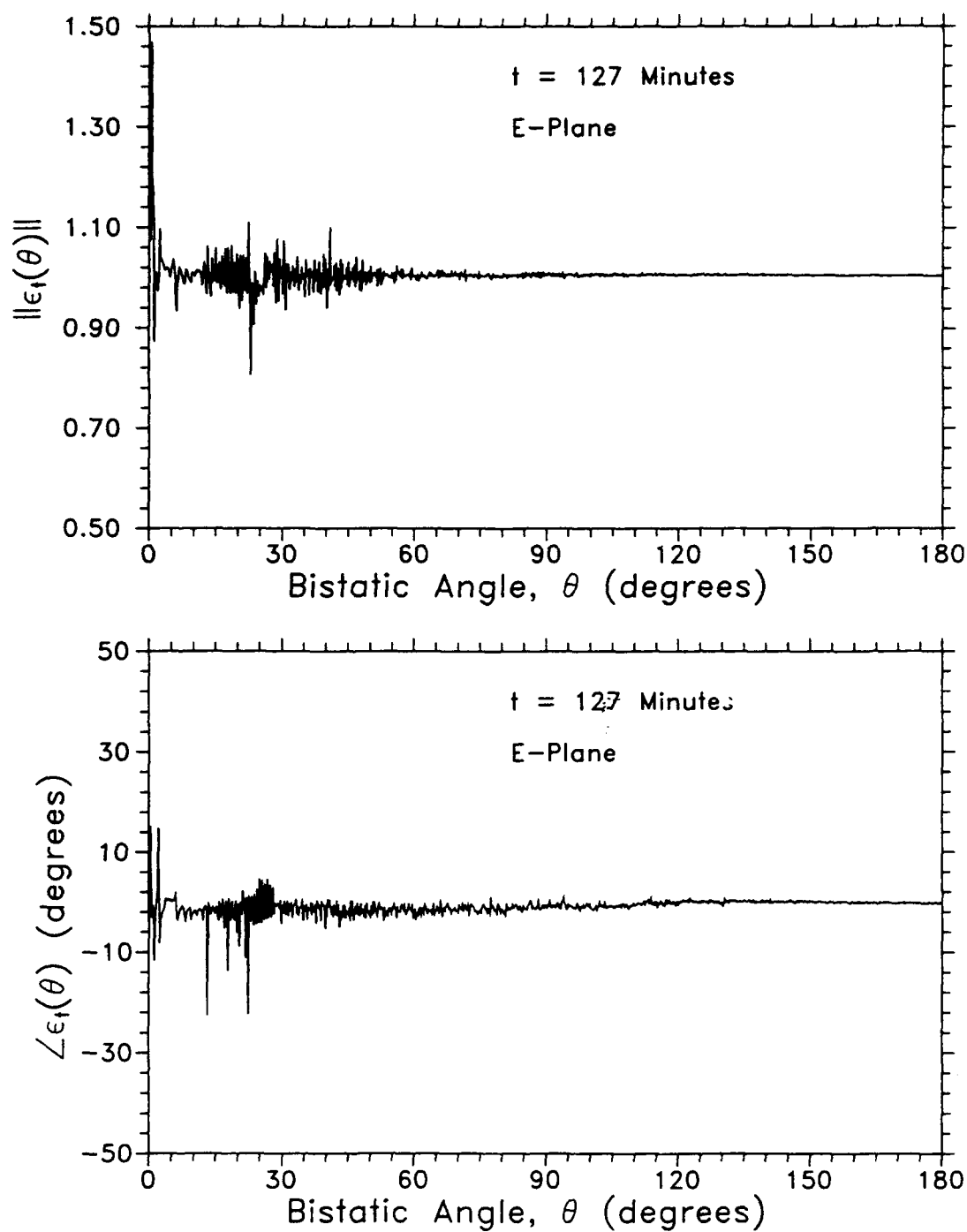


Figure C.26: Perturbation Phasor Computed from Two E-plane Background Measurements Separated in Time by About 2 Hours

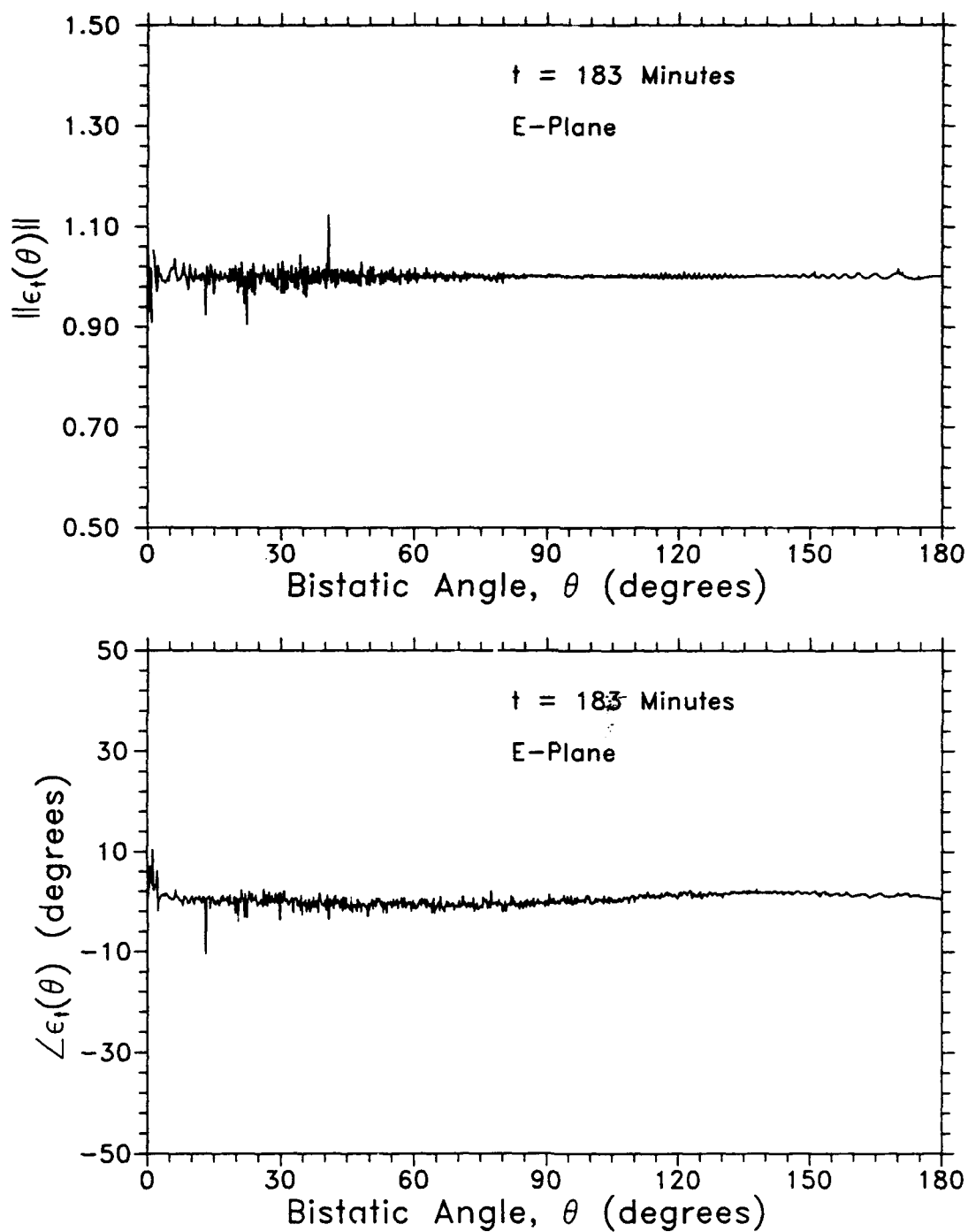


Figure C.27: Perturbation Phasor Computed from Two E-plane Background Measurements Separated in Time by About 3 Hours

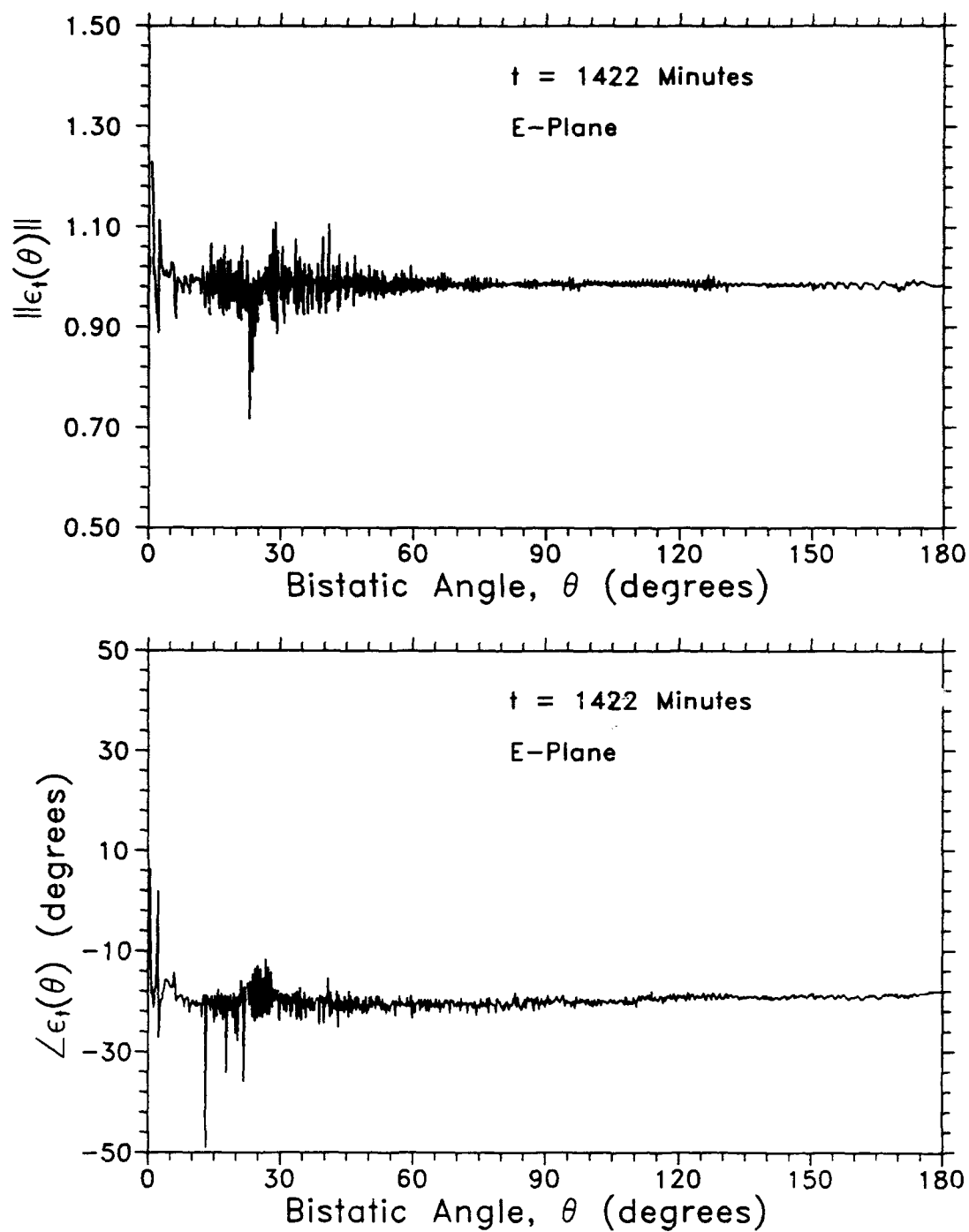


Figure C.28: Perturbation Phasor Computed from Two E-plane Background Measurements Separated in Time by About 24 Hours

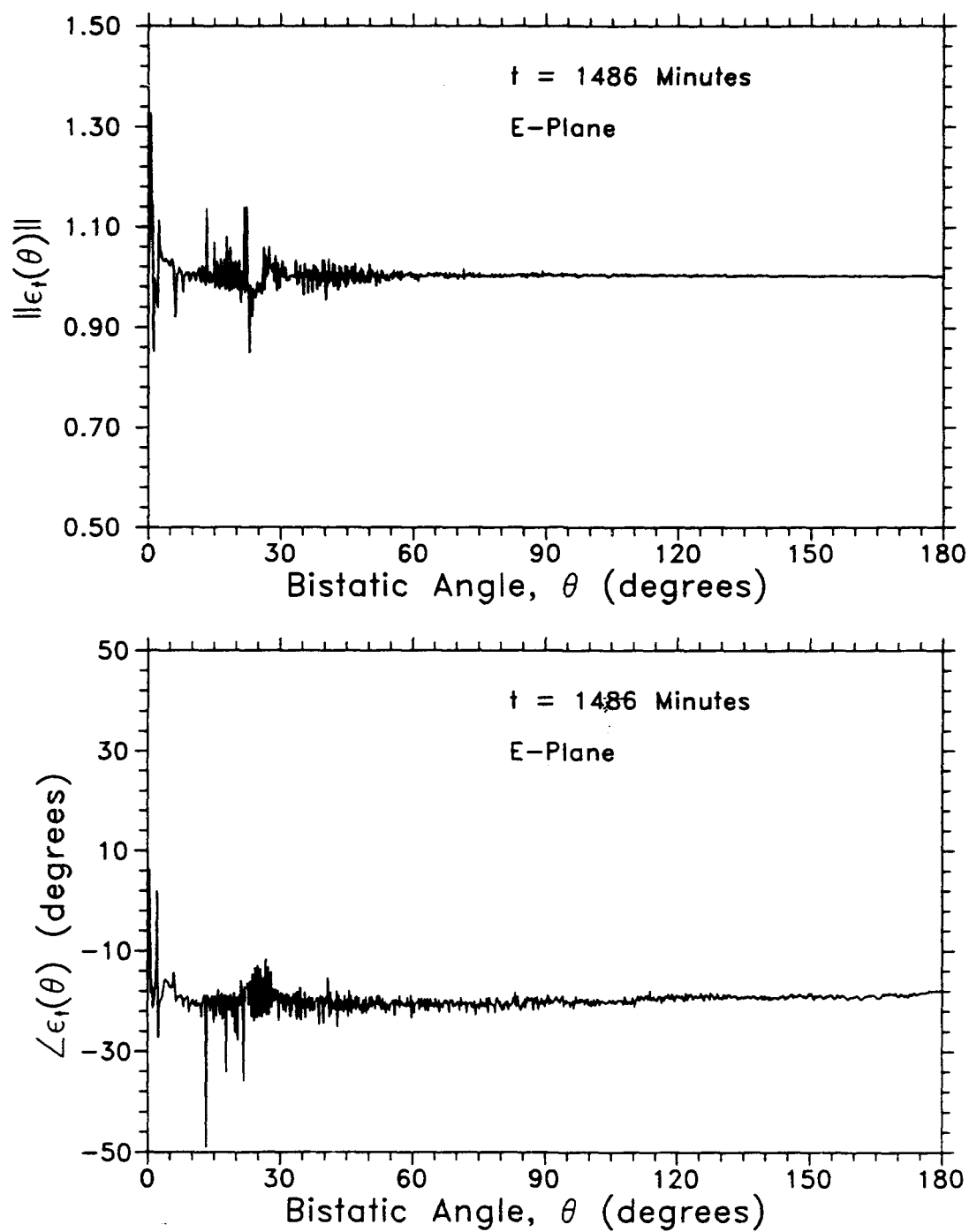


Figure C.29: Perturbation Phasor Computed from Two E-plane Background Measurements Separated in Time by About 25 Hours

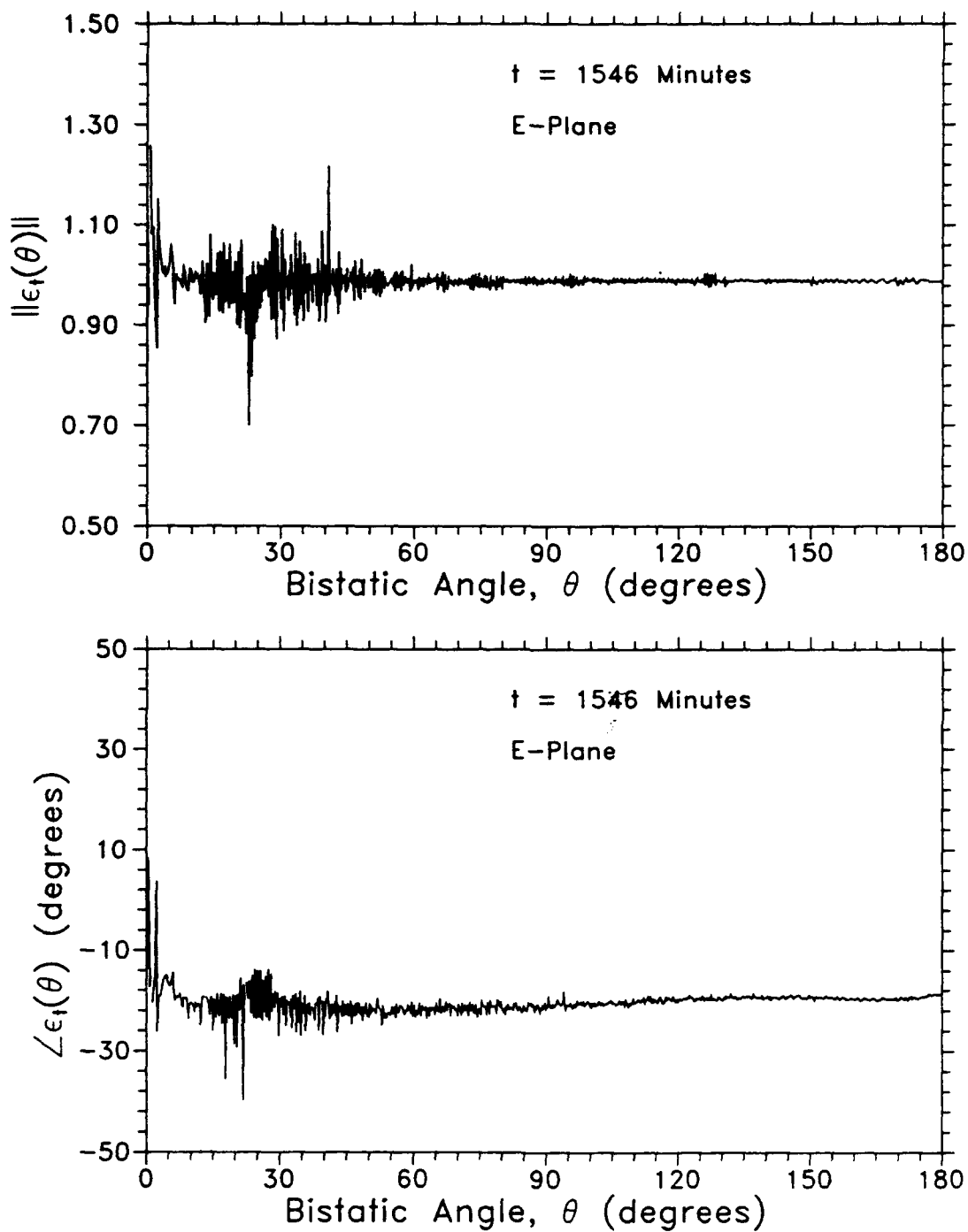


Figure C.30: Perturbation Phasor Computed from Two E-plane Background Measurements Separated in Time by About 26 Hours

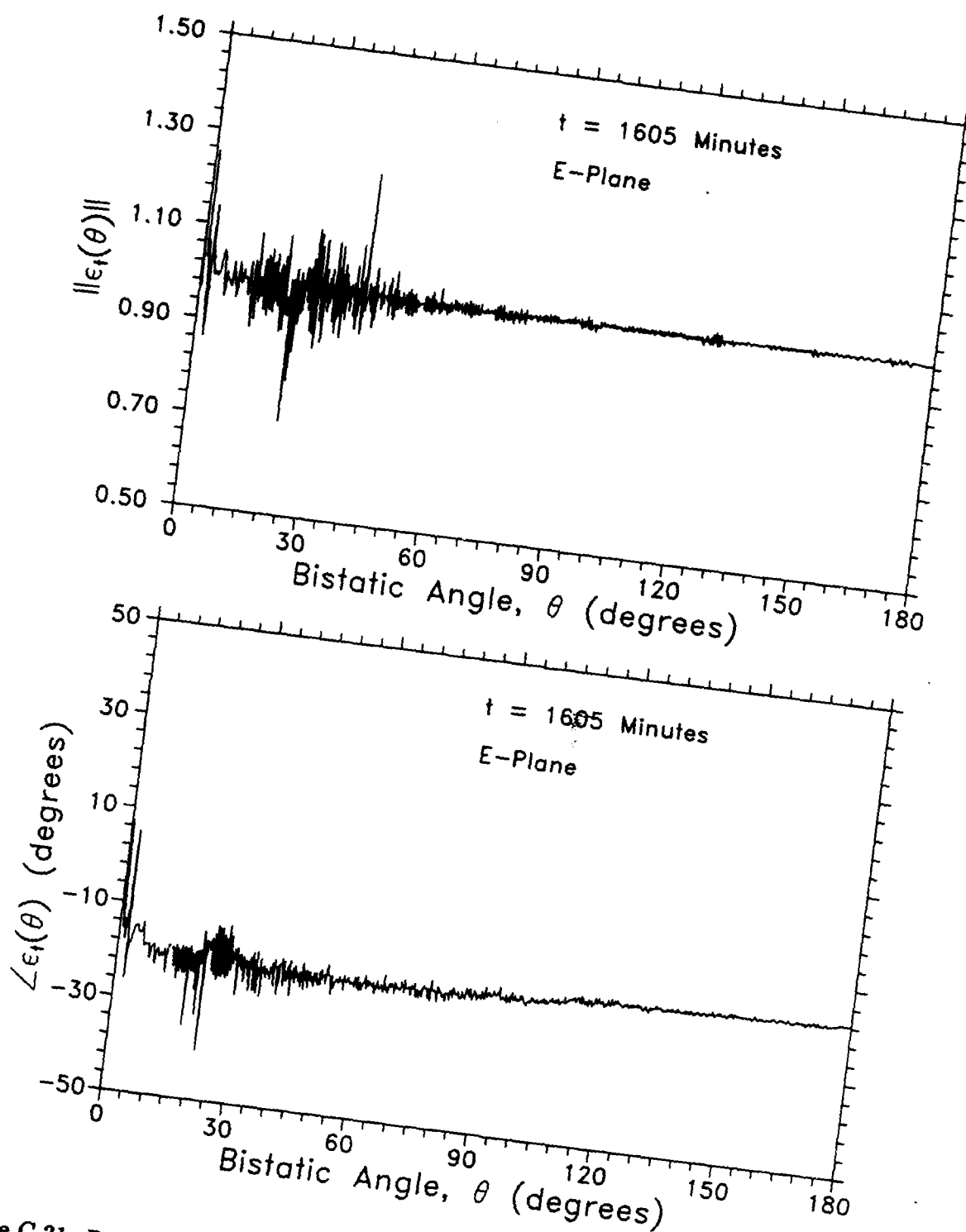


Figure C.31: Perturbation Phasor Computed from Two E-plane Background Measurements Separated in Time by About 27 Hours

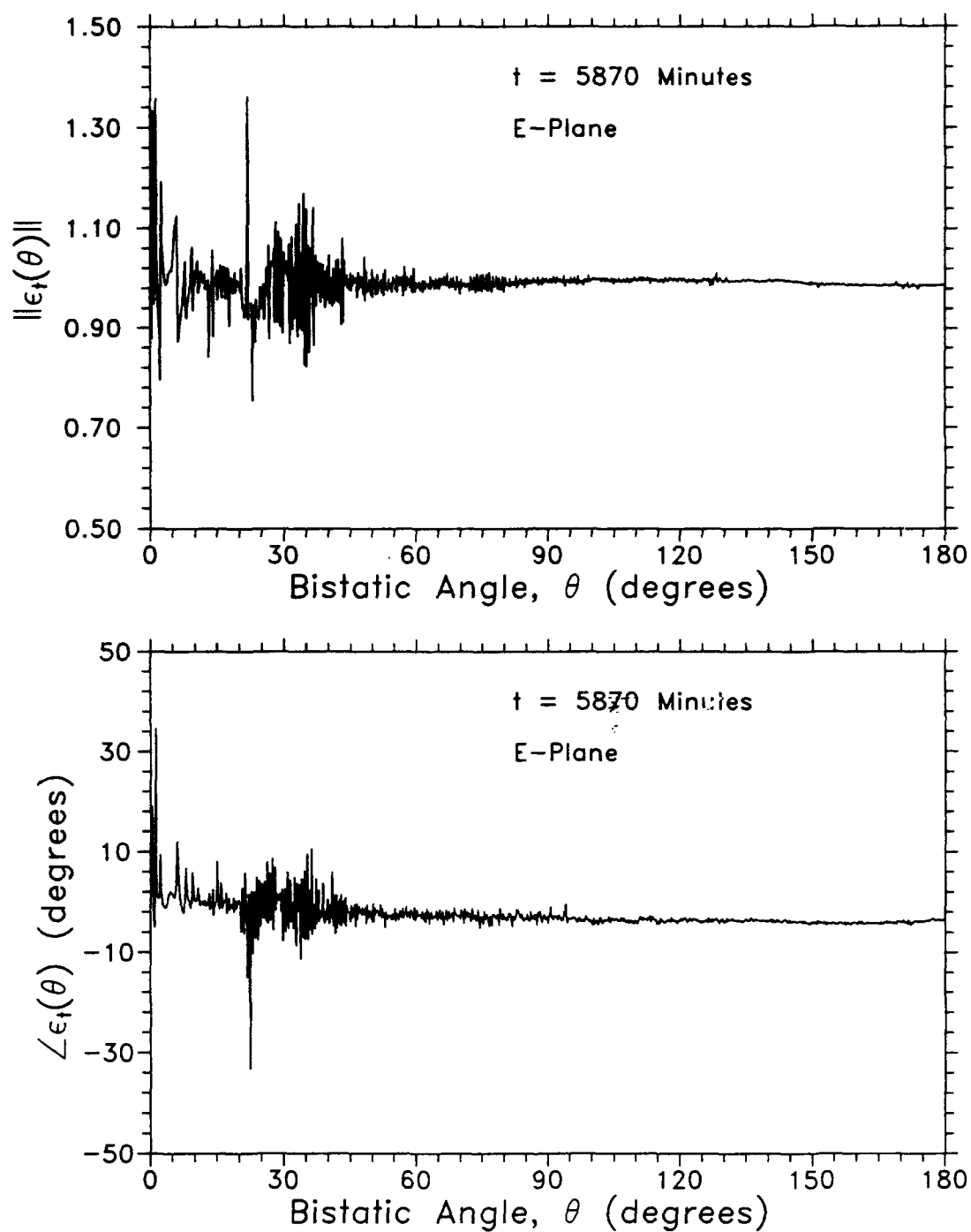


Figure C.32: Perturbation Phasor Computed from Two E-plane Background Measurements Separated in Time by About 98 Hours

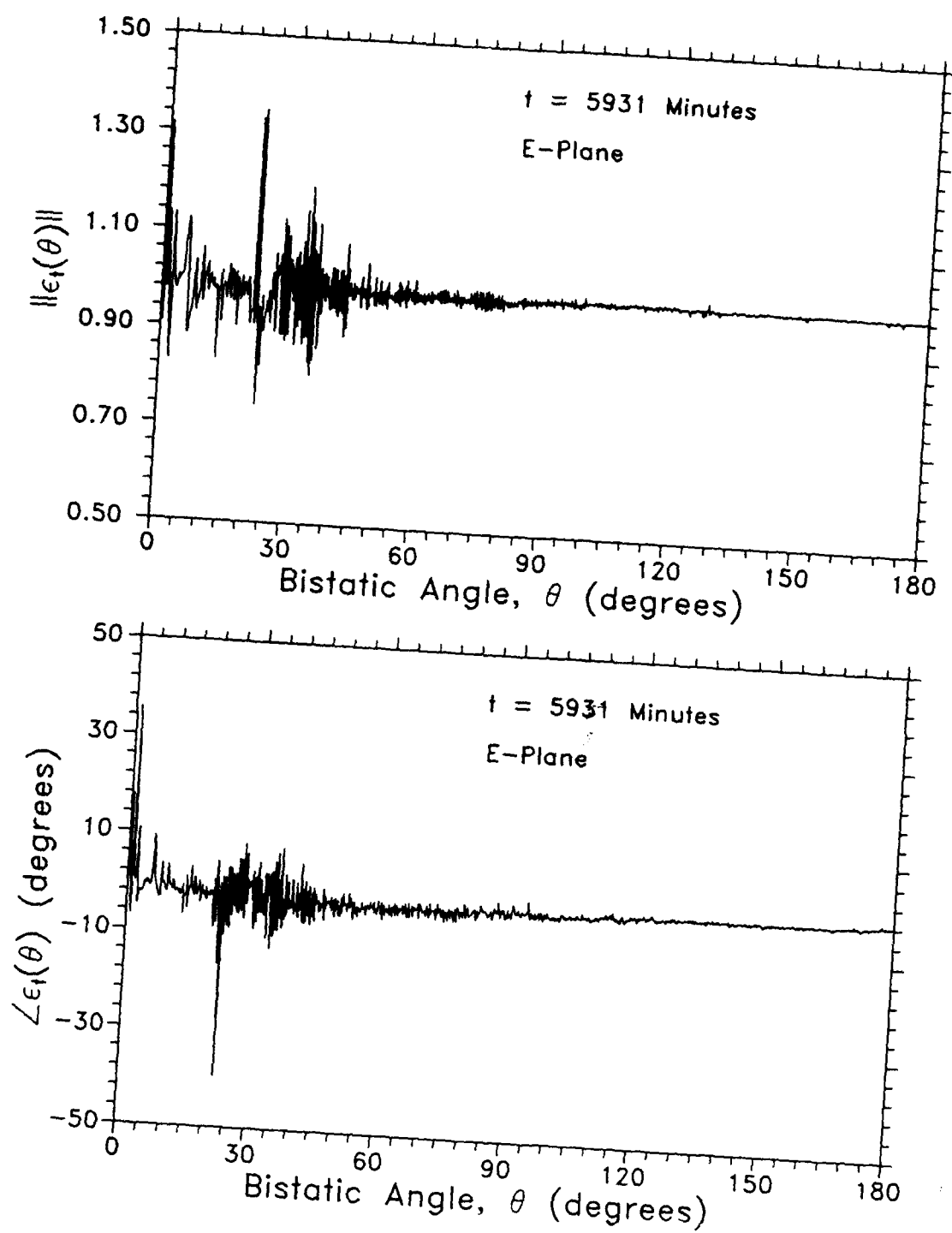


Figure C.33: Perturbation Phasor Computed from Two E-plane Background Measurements Separated in Time by About 99 Hours

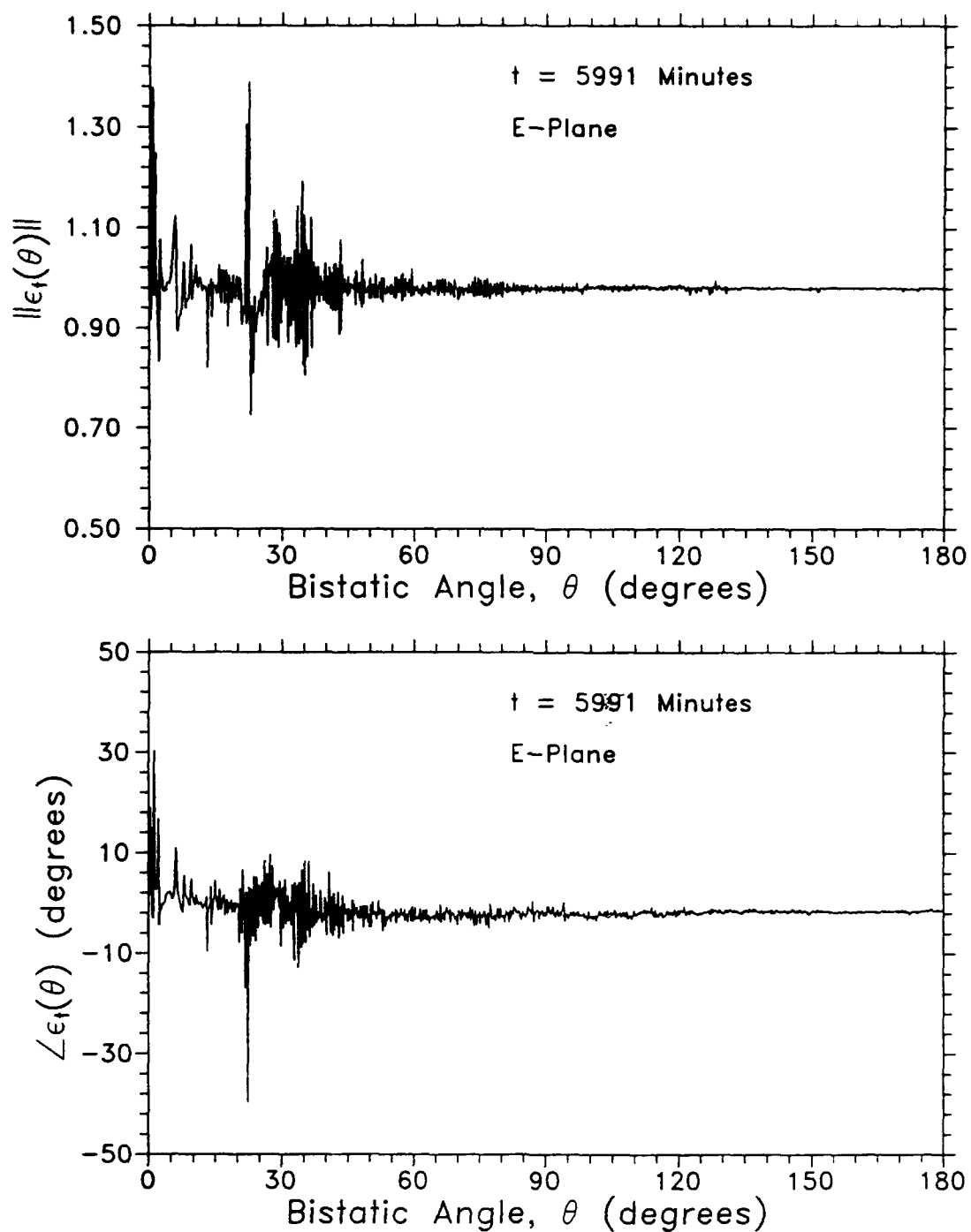


Figure C.34: Perturbation Phasor Computed from Two E-plane Background Measurements Separated in Time by About 100 Hours

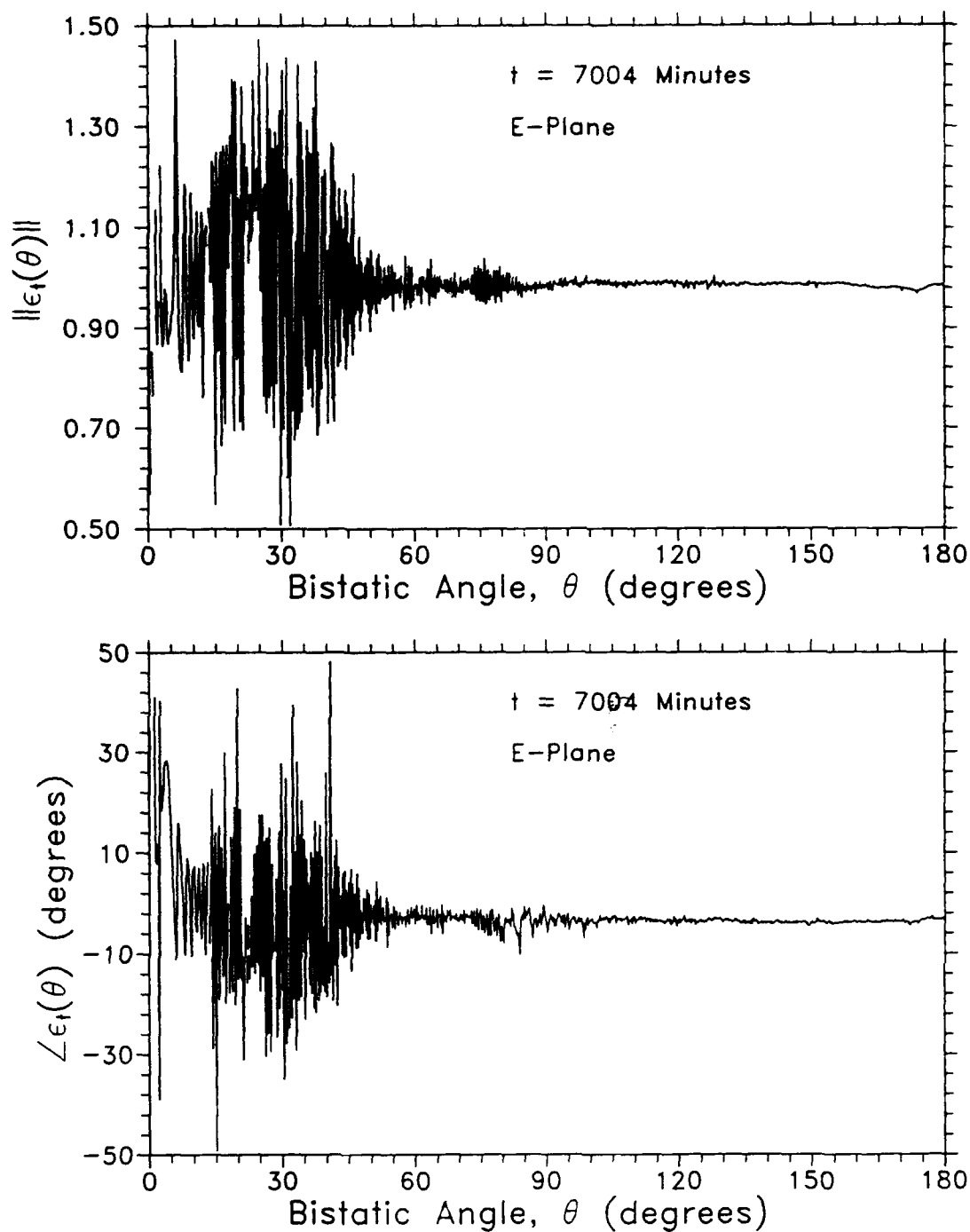


Figure C.35: Perturbation Phasor Computed from Two E-plane Background Measurements Separated in Time by About 117 Hours

Appendix D

DERIVATION OF THE MINIMUM RCS MEASURABLE

Let $A_o(\theta)$ be the power level displayed by the receiver in dB at the observation point, θ , and $\phi_o(\theta)$ be the relative phase displayed. The circle indicates the particular measurement with $o = t$ denoting the total field, and $o = b$ denoting the background field. The raw data used to compute the measured scattered field, $E_s^M(\theta)$, is then, (A_t, ϕ_t) and (A_b, ϕ_b) .

If we assume the receiver provides phase data with infinite resolution and amplitude data with a resolution of $\pm\delta$ dB, and the multipath field is negligible, we can write the raw data as field phasors using Eqs. (D.1) and (D.2),

$$E_t = 10^{\pm \frac{\delta_1}{20}} \times 10^{\frac{A_t}{20}} \exp[i\phi_t], \quad (D.1)$$

$$E_b = 10^{\pm \frac{\delta_2}{20}} \times 10^{\frac{A_b}{20}} \exp[i\phi_b]. \quad (D.2)$$

Neglecting the multipath field, from Eq. (2.3) we note that,

$$E'_t = E'_s + E'_b, \quad (D.3)$$

and from Eq. (2.5) the measured scattered field is,

$$E_s^M(\theta) = E'_s(\theta) + E'_b(\theta) - E_b(\theta). \quad (D.4)$$

Rewriting the measured scattered field in terms of the recorded data we have

$$E_s^M(\theta) = \epsilon_1 10^{\frac{A_t}{20}} \exp[i\phi_t] - \epsilon_2 10^{\frac{A_b}{20}} \exp[i\phi_b], \quad (D.5)$$

where $\epsilon_1 = 10^{\pm \frac{\delta_1}{20}}$ and $\epsilon_2 = 10^{\pm \frac{\delta_2}{20}}$. From Eqs. (D.1), (D.2), and (D.3) the measured scattered field can be written

$$E_s^M(\theta) = \epsilon_1 \left[E'_s(\theta) + E_b(\theta) \left(1.0 - \frac{\epsilon_2}{\epsilon_1} \right) \right], \quad (D.6)$$

where,

$$E'_s(\theta) + E'_b(\theta) = 10^{\frac{A_t}{20}} \exp[i\phi_t],$$

and

$$E_b(\theta) + E'_b(\theta) = 10^{\frac{A_b}{20}} \exp[i\phi_b],$$

Dividing Eq. (D.6) by $E'_s(\theta)$ gives

$$\frac{E_s^M(\theta)}{E'_s(\theta)} = \epsilon_1 \left[1.0 + \frac{E_b(\theta)}{E'_s(\theta)} \left(1.0 - \frac{\epsilon_2}{\epsilon_1} \right) \right]. \quad (D.7)$$

For the ASBSMS receiver (SA-1785) the amplitude resolution is 0.01 dB. This gives a worst case of $\delta_1 = 0$, $\delta_2 = .02$ and $\epsilon_1 = 1.0$, $\epsilon_2 = 1.0023$. From Eq. (D.7) we can write

$$E_s^M(\theta) = E'_s(\theta) \left[1.0 + \frac{E_b(\theta)}{E'_s(\theta)} (-0.0023) \right], \quad (D.8)$$

which means that the resolution error will be on the order of the true scattered field when the true scattered field power is about 53 dB below the nominal background level. As we saw earlier in Figures C.7 and C.8, the nominal background level is about -20 dBsm for the H-plane and -10 dBsm for E-plane. This places a lower limit on the RCS measurable with the ASBSMS of approximately -73 dBsm for H-plane and -63 dBsm for E-plane. For ± 1 dB accuracy this limit must be about 20 dB higher or -53 dBsm for the H-plane and -43 dBsm for E-plane.

**MISSION
OF
ROME LABORATORY**

Rome Laboratory plans and executes an interdisciplinary program in research, development, test, and technology transition in support of Air Force Command, Control, Communications and Intelligence (C³I) activities for all Air Force platforms. It also executes selected acquisition programs in several areas of expertise. Technical and engineering support within areas of competence is provided to ESD Program Offices (POs) and other ESD elements to perform effective acquisition of C³I systems. In addition, Rome Laboratory's technology supports other AFSC Product Divisions, the Air Force user community, and other DOD and non-DOD agencies. Rome Laboratory maintains technical competence and research programs in areas including, but not limited to, communications, command and control, battle management, intelligence information processing, computational sciences and software producibility, wide area surveillance/sensors, signal processing, solid state sciences, photonics, electromagnetic technology, superconductivity, and electronic reliability/maintainability and testability.